

# Interpretation of Fluid-Induced Seismicity at Geothermal and Hydrocarbon Reservoirs of Basel and Cotton Valley

Dissertation  
zur Erlangung des akademischen Grades  
Doktor der Naturwissenschaften  
am Fachbereich Geowissenschaften  
der Freien Universität Berlin

vorgelegt von  
Carsten Dinske

Dezember 2010



Ich erkläre hiermit an Eides statt, dass ich die vorliegende Dissertation selbstständig und nur unter Verwendung der angegebenen Quellen und Hilfsmittel angefertigt habe.

Berlin, 9. Dezember 2010

Referent: Prof. Serge A. Shapiro

Korreferent: Prof. Rainer Kind

Datum der Disputation: 27. April 2011



*Das Leben ist wie ein Fahrrad...  
Man muss sich vorwärts bewegen,  
um das Gleichgewicht nicht zu verlieren.*

Albert Einstein



# Abstract

The main objective of the thesis is a further development of the seismicity based reservoir characterization approach (*SBRC*). In general, the *SBRC* method is applied to microearthquakes resulting from fluid injections into the subsurface. The *SBRC* method allows firstly, to estimate the fluid-transport properties of hydraulically stimulated reservoir rock, secondly, to examine the fluid-rock interaction, and thirdly, to characterize activated fractures and faults within the reservoir. Thus, *SBRC* substantially contributes to the understanding of physical processes that are related to injection-induced seismicity. To extend the applicability of *SBRC* the thesis focus on the following topics.

The *SBRC* method so far assumes a constant source strength of a fluid injection. This condition, however, is not always given, such as by the hydraulic stimulation of a geothermal reservoir in Basel (Switzerland). In the first part of the thesis, *SBRC* is extended in order to analyze seismicity resulting from fluid injections where the source strength is linearly increasing with time. For this purpose, an analytical solution of the diffusion equation is derived taking into account this special condition. The derived analytical solution and the resulting expressions for seismicity rate and cumulative number of microearthquakes are numerically verified using finite element modeling and synthetically generated seismicity. Afterwards, *SBRC* methods are applied to the catalog of fluid-induced seismicity recorded in Basel. They provide consistent estimates of the permeability of the hydraulically stimulated reservoir. It is of the order of 150 *microDarcy* by assuming an effective-isotropic medium. The criticality which statistically describes the strength of pre-existing fractures is found to be distributed between about 5000 *Pa* and approximately 1 *MPa*.

In the second part of the thesis, a model is introduced in order to interpret fracturing-induced seismicity related to single-planar hydraulic fractures. The model considers the growth of fracture and seismicity as a combined geometry- and diffusion-controlled process. It is confirmed by observations from fracturing-induced seismicity in the Cotton Valley gas reservoir (USA). The space-time diagrams ( $r - t$  diagrams) of induced microearthquakes show signatures of fracture

volume growth, loss of treatment fluid, and diffusion of injection-induced pore pressure perturbations within the fracture as well as from the fracture into the surrounding formation. Evaluation of envelopes of the spatio-temporal distribution of fracturing-induced seismicity allows to determine geometrical parameters and hydraulic properties of the created fracture. Considering a volume balance principle of the injected treatment fluid permits to quantify the fluid loss from the fracture into the virgin reservoir and to estimate the reservoir permeability. The proposed interpretational approach is applied to microearthquakes induced during three stages of hydraulic fracturing in Cotton Valley. Although the three stages differ with respect to the treatment design parameters, it is found that the individual stages resulted in similar fracture geometries. Ratios of new fracture volume and total injected volume are nearly identical in all treatments. It means that the fracture growth process is likely decoupled from the type of treatment design. Estimates of fluid loss and reservoir permeability are consistent for the three investigated fracturing stages. The results obtained from the interpretational model are confirmed by modeling the fracture propagation using the maximum likelihood method.

Fluid injections into the subsurface can sometimes induce earthquakes characterized by a significant magnitude. In particular, seismic events with larger magnitudes are reported from geothermal reservoirs. Understanding of the scaling relations of magnitudes of fluid-induced seismicity is crucial for assessing the seismic risk by injection operations. In the last part of the thesis, a statistical model is introduced which describes the magnitude distribution of microearthquakes induced during injections. It combines a Gutenberg-Richter statistics of magnitude probability with the cumulative number of induced microearthquakes. Earthquake magnitudes resulting from hydraulic stimulation in Basel and from hydraulic fracturing in Cotton Valley are in agreement with this model. Furthermore, the model allows to identify controlling parameters of the size and distribution of magnitudes. These include design parameters of a fluid injection, such as fluid volume, or fluid flow rates and injection duration, and seismotectonic quantities like Gutenberg-Richter  $a$ - and  $b$ -value and the tectonic potential which is defined by statistical properties of pre-existing fractures.

# Zusammenfassung

Die wesentliche Zielsetzung der vorliegenden Dissertation ist eine Weiterentwicklung des Ansatzes der Seismizitätsbasierten Reservoircharakterisierung (*SBRC*). Die *SBRC* Methode wird im Allgemeinen auf Mikroerdbeben, die durch die Injektion von Fluiden in den Untergrund ausgelöst werden, angewendet. Dieses ermöglicht einerseits die Fluidtransporteigenschaften des hydraulisch stimulierten Reservoirgesteins abzuschätzen, zweitens, die Fluid-Gesteins-Wechselwirkungen zu untersuchen, und drittens, die aktivierten Bruch- und Störungssysteme innerhalb des Reservoirs zu charakterisieren. *SBRC* trägt somit wesentlich zum Verständnis der physikalischen Prozesse, die in Verbindung zu induzierter Seismizität stehen, bei. Zur Erweiterung der Anwendbarkeit der *SBRC* Methode konzentriert sich die Dissertation auf die folgenden Themen.

Die *SBRC* Methode basiert bisher auf der Annahme, dass die Quellstärke während einer Fluidinjektion konstant ist. Diese Bedingung ist jedoch nicht immer gegeben, wie beispielsweise bei der hydraulischen Stimulation des geothermischen Reservoirs in Basel (Schweiz). Im ersten Teil der Dissertation wird die *SBRC* Methode erweitert, um Seismizität resultierend aus Fluidinjektionen in denen die Quellstärke linear mit der Zeit ansteigt, zu analysieren. Zu diesem Zweck wird eine analytische Lösung der Diffusionsgleichung hergeleitet, welche diese spezielle Randbedingung berücksichtigt. Diese Lösung und die daraus ermittelten mathematischen Formulierungen für Seismizitätsrate und Anzahl der Mikroerdbeben werden numerisch verifiziert mit Hilfe von Finite-Elementen-Modellierung und synthetisch erzeugter Seismizität. Anschließend wird die *SBRC* Methode auf den Katalog fluid-induzierter Seismizität in Basel angewendet. Sie ergibt eine konsistente Abschätzung der Permeabilität des hydraulisch stimulierten Reservoirs von  $150 \text{ microDarcy}$ . Die Kritikalität, welche statistisch die Festigkeit von prä-existierenden Bruchsystemen beschreibt, ist verteilt zwischen etwa  $5000 \text{ Pa}$  und ca.  $1 \text{ MPa}$ .

Im zweiten Teil der Dissertation wird ein Modell vorgestellt, das die Interpretation von induzierter Seismizität im Zusammenhang mit einfach-planaren hydraulischen Brüchen ermöglicht. Das Modell betrachtet das Wachstum eines solchen

hydraulisch-generierten Bruches und der assoziierten Seismizität als einen kombinierten Geometrie- und Diffusions-kontrollierten Prozess. Dieses wird durch Beobachtungen von induzierter Seismizität aus dem Cotton Valley Gasreservoir (USA) bestätigt. Die Raum-Zeit-Diagramme ( $r - t$  Diagramme) der induzierten Mikroerdbeben zeigen Signaturen von Bruchausbreitung, des Verlustes von Fluid vom Bruch in das umgebende Reservoirgestein und die Ausbreitung von injektions-induzierten Perturbationen des Porenfluiddrucks innerhalb des Bruches. Die Auswertung der Einhüllenden der räumlich-zeitlichen Verteilung der induzierten Seismizität erlaubt die Bestimmung von geometrischen Parametern und von hydraulischen Eigenschaften des erzeugten Bruches. Ausgehend von dem Prinzip einer Volumenbalance des injizierten Fluides können der Fluidverlust aus dem Bruch in die umgebende Formation und die Permeabilität des Reservoirs quantifiziert werden. Der vorgestellte Interpretationsansatz wird auf Mikroerdbeben, die während dreier Phasen hydraulischer Bruchbildung in Cotton Valley ausgelöst worden sind, angewendet. Obwohl die drei Phasen sich hinsichtlich der Konzeption der Injektion unterscheiden, ergaben die einzelnen Phasen sehr ähnliche Bruchgeometrien. Das Verhältnis aus neu geschaffenem Bruchvolumen und dem injiziertem Gesamtvolumen ist nahezu identisch in allen Phasen. Die Abschätzungen von Fluidverlust und Reservoirpermeabilität sind konsistent für die drei untersuchten Phasen. Die aus dem vorgestellten Interpretationsmodell abgeleiteten Kenngrößen sind anhand einer Modellierung der Bruchausbreitung mit der Maximum-Likelihood-Methode bestätigt worden.

Fluidinjektionen in den Untergrund können zum Teil Erdbeben, die durch eine signifikante Magnitude charakterisiert sind, zur Folge haben. Insbesondere in geothermischen Reservoiren sind seismische Ereignisse mit größerer Magnitude beobachtet worden. Das Verständnis von Skalierungsverhältnissen der Magnituden von fluid-induzierter Seismizität ist entscheidend für die Beurteilung des seismischen Risikos durch Fluidinjektionen. Im letzten Teil der Dissertation wird ein statistisches Modell vorgestellt, welches die Magnitudenverteilung von Mikroerdbeben, die während der Injektion auftreten, beschreibt. Das Modell kombiniert die Gutenberg-Richter Statistik der Magnitudenwahrscheinlichkeit mit der kumulativen Anzahl der induzierten Mikroerdbeben. Beobachtungen von Erdbebenmagnituden bei der hydraulischen Stimulation in Basel und bei der hydraulischen Bruchbildung in Cotton Valley sind in Übereinstimmung mit diesem Modell. Darüber hinaus ermöglicht das Modell, die kontrollierenden Parameter der Größe und der Verteilung der Erdbebenmagnituden zu identifizieren. Dazu zählen einerseits Konzeptionsparameter einer Fluidinjektion, wie zum Beispiel das Fluidvolumen oder die Fließrate und die Dauer der Injektion, als auch seismotektonische Kenngrößen, wie Gutenberg-Richter  $a$ - und  $b$ -Wert und das tektonische Potential, welches von den statistischen Eigenschaften prä-existierender Bruchsysteme definiert wird.

# Contents

<b>1</b>	<b>Introduction</b>	<b>13</b>
<b>2</b>	<b>Triggering Concept of Fluid-Induced Seismicity</b>	<b>17</b>
2.1	Introduction . . . . .	17
2.2	Triggering Controlled by Linear Pore Pressure Diffusion . . . . .	18
2.3	Triggering Controlled by Non-Linear Pore Pressure Diffusion . . . . .	24
2.4	Seismicity Back Front . . . . .	31
<b>3</b>	<b>Seismicity Induced by Fluid Injections with Time-Dependent Source Strength</b>	<b>35</b>
3.1	Introduction . . . . .	35
3.2	Analytical Formulations . . . . .	37
3.2.1	Pore Pressure Perturbation Resulting From Constant Injection Source Strength . . . . .	37
3.2.2	Pore Pressure Perturbation Resulting From Non-Constant Injection Source Strength . . . . .	38
3.2.3	Pore Pressure Related Signatures of Fluid-Induced Seismicity . . . . .	42
3.3	Numerical Verification . . . . .	49
3.3.1	Modeling Approach . . . . .	49
3.3.2	Comparison of Modeling Results with the Analytical Solution . . . . .	52
3.4	Application to Basel Data . . . . .	53
3.4.1	Heuristic Analysis . . . . .	58
3.4.2	Deterministic Analysis . . . . .	62
3.4.3	Numerical Verification of Results . . . . .	70
3.5	Summary and Conclusions . . . . .	78
<b>4</b>	<b>Interpretational Model for Single-Planar Hydraulic Fractures</b>	<b>83</b>
4.1	Introduction . . . . .	83
4.2	Hydraulic Fracture Growth and Induced Seismicity . . . . .	85

4.3	Interpretation Flow Chart . . . . .	89
4.4	Application to Cotton Valley Data . . . . .	91
4.4.1	A Gel Treatment . . . . .	93
4.4.2	A Water Treatment . . . . .	97
4.4.3	Summary of Results . . . . .	101
4.5	Modeling of Fracture Propagation . . . . .	101
4.6	Fracturing Related Phenomena . . . . .	107
4.6.1	Flow Pattern Heterogeneities . . . . .	107
4.6.2	Kaiser Effect Breakdown . . . . .	109
4.7	Summary and Conclusions . . . . .	115
<b>5</b>	<b>Magnitudes of Fluid-Induced Seismicity</b>	<b>117</b>
5.1	Theoretical Model of Magnitude Distribution of Fluid-Induced Seismicity . . . . .	118
5.2	Magnitude Distributions of Basel and Cotton Valley Data Catalogs	123
5.3	Summary and Conclusions . . . . .	128
<b>6</b>	<b>Summary and Perspectives</b>	<b>131</b>
	<b>References</b>	<b>134</b>
<b>A</b>	<b>Supplement to Chapter 4</b>	<b>143</b>

# Chapter 1

## Introduction

Injections of fluids into the deeper subsurface are by now a routine and cover a wide field of applications. Amongst them are, for instance, operations that lead to a permeability enhancement required for development and exploitation of geothermal and hydrocarbon reservoirs (Fehler et al., 1987; Block et al., 1994). In many cases, injection operations are accompanied by numerous earthquakes which are predominantly of low, non-noticeable magnitude [ $-3 < M < 2$ ]. If a fluid injection is seismically monitored by an adequately sensitive network of geophones/seismometers, then the registered seismic activity can provide useful information about the fluid-rock interaction. One important aspect of such monitoring is the high-resolution spatial mapping of induced seismicity. It allows to draw inferences about the hydraulically stimulated rock volume, activated pre-existing fractures, and orientations of fault zones.

The seismicity based reservoir characterization approach (*SBRC*) (Shapiro et al., 1997, 1999) goes one step further in the analysis and interpretation. It correlates the spatio-temporal evolution of fluid-induced microearthquakes with the relaxation of pore pressure perturbations caused by the injection. In this way, the *SBRC* permits the following. On the one hand, it well describes observed features of fluid-induced seismicity such as triggering fronts and seismicity rates, and therefore contributes to a better understanding of physical processes (Shapiro et al., 2003; Parotidis et al., 2004; Parotidis and Shapiro, 2004). On the other hand, the *SBRC* can be used to estimate the permeability tensor in reservoir-scale (Shapiro et al., 2002) as well as to characterize pre-existing fracture systems by determining the distribution of critical pressures (Rothert and Shapiro, 2007).

## Objectives

The main objective of the current thesis is a further development of the *SBRC* approach. It became evident that assumptions, such as the linearity of processes and the stationarity of injection sources, are sometimes insufficient to describe fluid injections and to explain observations made from catalogs of fluid-induced earthquakes. Therefore two points are of central interest in this thesis. The first one covers the non-stationarity of injection sources which is often the case for hydraulic stimulation operations in geothermal reservoirs. The second key point addresses the consequences of a non-linear interaction between injected fluid and reservoir rock. These non-linear interactions are manifested in a pressure-dependent permeability which is a common observation from hydraulic fracturing operations in hydrocarbon reservoirs. In addition, the relations of statistical distribution of fluid-induced earthquake magnitudes are written down in this thesis covering a third key topic. The magnitude examinations rely on the awareness that also fluid injections can sometimes produce seismic risk. An in-depth knowledge in order to mitigate such a risk is lacking up to now. Altogether this thesis contributes to a better understanding of the processes leading to the triggering of seismicity by injection operations. It provides instructions for an analysis, evaluation, and interpretation of fluid-induced earthquakes in terms of *SBRC*.

## Outline

This thesis is structured in respect to the mentioned three key points. At first, however, I will introduce the status-quo of the understanding of triggering mechanisms of fluid-induced seismicity. It includes a description of the concept of seismicity triggering fronts. It is derived for the condition of both a linear as well as a non-linear diffusion of pore pressure perturbations resulting from fluid injections. The non-linear equations provide a more general formalism which comprehends a diffusion of linear type as an asymptotic situation. Microseismic activity occurring after the stop of fluid injection can be explained by the concept of seismicity back front. Like the concept of triggering fronts, it also assumes a diffusion-like process of relaxation of induced pressure perturbations.

Chapter 3 focuses on further developing *SBRC* methods in such a way that a time-dependent injection source strength is taken into account. It is required in order to accurately apply *SBRC* to microearthquakes which are induced by injection pressures increasing with ongoing injection time. The first step is to derive an analytical solution of the diffusion equation for this special problem. Subsequent to the numerical verification of the derived analytical solution, *SBRC* is applied to the catalog of microearthquakes induced by the hydraulic stimulation of a geothermal reservoir in December 2006 in Basel (Switzerland).

Of special interest by hydraulic fracturing operations in the hydrocarbon industry is a reliable estimation of hydraulic properties of fluid-driven fractures and virgin reservoir. In Chapter 4, an interpretational model is proposed for single-planar (classical 1D) hydraulic fractures. It uses spatio-temporal signatures of the associated fracturing-induced seismicity to derive geometry parameters of a created fracture. By applying a volume balance principle of the injected treatment fluid the transport properties can finally be obtained from the interpretational model. The approach is tested on microearthquake catalogs recorded during hydraulic fracturing in a tight-gas sandstone reservoir in Carthage Cotton Valley (USA). Scaling relations of the size and frequency of earthquakes resulting from fluid injection operations are presented in Chapter 5. A theoretical model is introduced which describes the statistical distribution of fluid-induced earthquake magnitudes. Observations of the magnitude distributions of microearthquakes induced in Basel and in Carthage Cotton Valley are in accordance with the model. Furthermore, the presented model allows to identify the controlling parameters of magnitude distributions and to specify the seismotectonic state of an injection location.



## Chapter 2

# Triggering Concept of Fluid-Induced Seismicity

### 2.1 Introduction

Borehole fluid injections into surrounding rocks are used for development of hydrocarbon and geothermal reservoirs, disposal of waste and for geological sequestration of carbon dioxide (Fehler et al., 1987; Block et al., 1994; Keck and Withers, 1994). Such injections are often accompanied by microseismic activity. Although the nature of fluid induced seismicity is still topic of ongoing research, one hypothesis explaining this phenomenon argues that the triggering of this type of seismicity is controlled by the relaxation of pore pressure perturbations (Pearson, 1981; Shapiro et al., 1997). Assuming that in some locations of the upper Earth crust the tectonical stresses are in near-critical condition, then minor changes of the in-situ stress state cause microseismicity. Due to the injection of a fluid volume into a reservoir rock the pore-fluid pressure  $p$  in the connected pore-space increases which consequently decreases the effective normal stress  $\sigma_{eff} = \sigma - p$ , where  $\sigma$  is total stress (Terzaghi, 1923). In accordance with the Coulomb failure criterion (Scholz, 2002), this modification of the stress state can lead to reactivation of pre-existing faults and fractures by triggering slip events and thereby releasing previously accumulated shear stress in the stimulated rock volume (Rutledge and Phillips, 2003). In this chapter, I will briefly introduce the status quo of the understanding of triggering processes of fluid-induced microseismicity.

## 2.2 Triggering Controlled by Linear Pore Pressure Diffusion

First attempts to physically describe the nature of fluid-induced seismicity and its triggering process in more detail were carried out by Shapiro et al. (1997). The spatio-temporal evolution of such a seismicity is governed by a diffusional process of relaxation of pore pressure perturbation. In an infinite heterogeneous anisotropic poroelastic medium, the differential equation of diffusion in the Biot low-frequency limit is given by (Biot, 1962):

$$\frac{\partial p}{\partial t} = \frac{\partial}{\partial x_i} \left[ D_{ij} \frac{\partial}{\partial x_j} p \right] \quad i, j = 1, 2, 3 . \quad (2.1)$$

Here  $p$  is the pore pressure perturbation,  $x_{i,j}$  are components of the radius vector from the injection source point and  $t$  is the time.  $D_{ij}$  are components of the hydraulic diffusivity tensor which is directly proportional to the Darcy permeability  $K_{ij}$  (Shapiro et al., 2003):

$$K_{ij} = \frac{\eta}{N} D_{ij} . \quad (2.2)$$

In this formulation, the physical quantities in front of the diffusivity tensor are dynamic viscosity of the pore fluid,  $\eta$ , and the poroelastic modulus  $N$  (see Shapiro et al., 2003). In the most simple case, that is a homogenous, isotropic, poroelastic medium, the diffusion equation reduces to:

$$\frac{\partial p}{\partial t} = D \nabla^2 p, \quad (2.3)$$

with a scalar hydraulic diffusivity  $D$ . In such a situation, the migration of pore pressure perturbations initiated at the injection source point can be described by a propagating front (Shapiro et al., 1997, 2002) according to:

$$r_t(t) = \sqrt{4\pi Dt} . \quad (2.4)$$

This relation was introduced as the triggering front equation of fluid-induced microseismicity. The distance  $r_t(t)$  defines the upperbound of the spatial domain where the occurrence of microearthquakes is characterized by a high probability. Hence Equation (2.4) corresponds to the upper envelope of a microseismicity cloud in a plot of its spatio-temporal distribution (the so-called  $r - t$  diagram). This envelope of parabolic type allows to heuristically estimate the hydraulic diffusivity of the seismically active rock volume.

In the following, two examples of fluid-induced seismicity are presented to demonstrate the validity of the triggering front concept. The first one considers

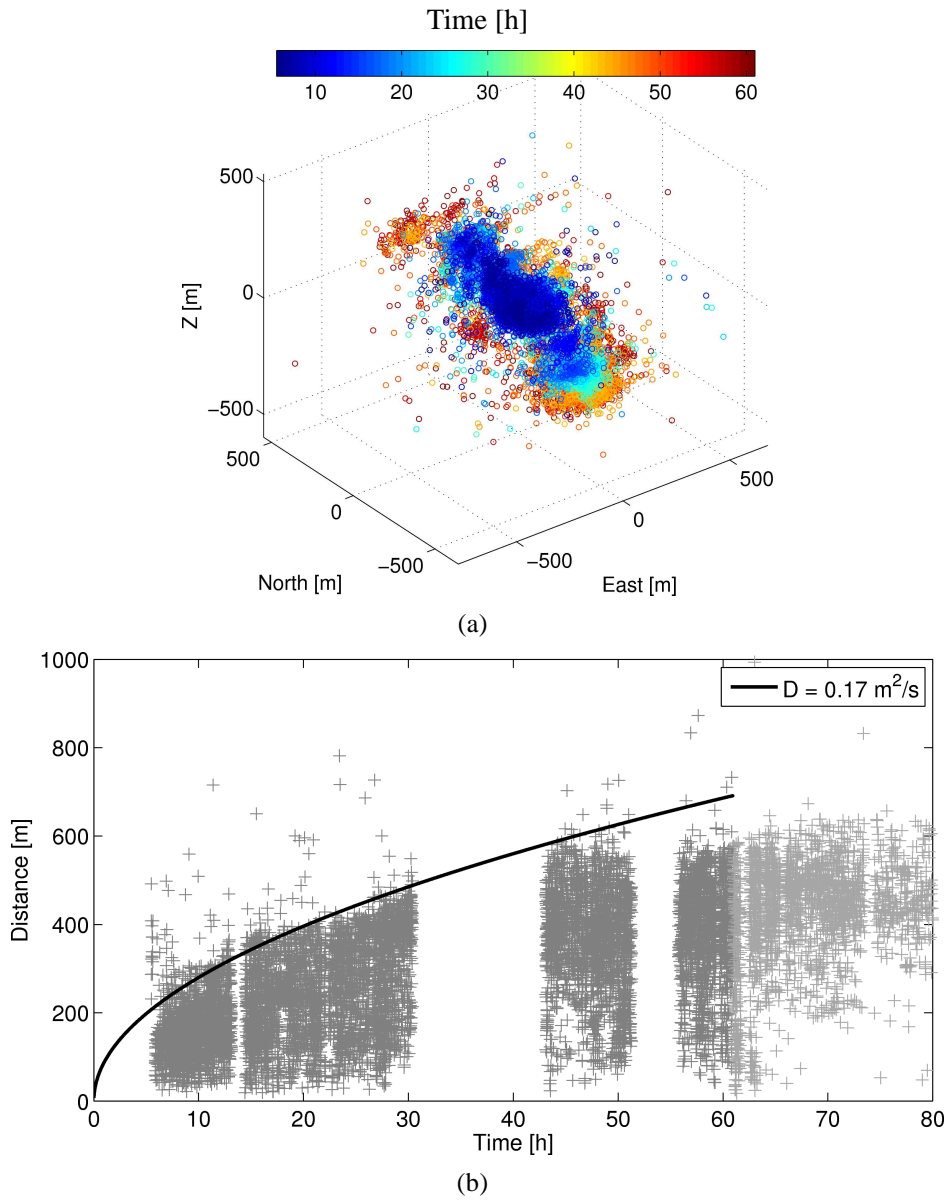


Figure 2.1: Microearthquakes induced during a hydraulic stimulation of a geothermal reservoir in Fenton Hill, USA. In December 1983, about  $21,000 \text{ m}^3$  water were injected at wellhead pressures close to  $50 \text{ MPa}$ . During the  $61 \text{ h}$  injection period, about 9000 locatable microearthquakes were detected. (a) Distribution of source locations (color corresponds to event occurrence time after the begin of injection) and (b) corresponding  $r - t$  diagram. Co-injection seismicity is shown in dark grey color, post-injection seismicity in light grey color. Solid black line denotes triggering front curve according to Equation (2.4). The estimated hydraulic diffusivity is  $D = 0.17 \text{ m}^2/\text{s}$ .

microseismic data from hydraulic stimulation of a geothermal reservoir in Fenton Hill, New Mexico (USA), in December 1983. The aim of the massive, high-pressure fluid injection was to create fluid pathways and hence to enhance the rock permeability. For this purpose, over  $21,000 \text{ m}^3$  water were pumped during about  $60 \text{ h}$  at wellhead injection pressures of  $48 \text{ MPa}$  into granitic rock (Phillips et al., 1997). More than 11,000 locatable microearthquakes were detected by the installed downhole station network, from which about 9000 occurred during the period of injection (Phillips et al., 1997). The distribution of hypocenters is shown in Figure 2.1(a). The area of microseismic activity forms an elongated zone, striking  $N355^\circ$  and dipping  $E70^\circ$ . Figure 2.1(b) shows the  $r - t$  diagram of induced microearthquakes (distance to injection point versus occurrence time). The spatio-temporal evolution clearly obeys a diffusional behavior. The corresponding signature, the parabolic triggering front curve  $r_t(t)$ , well limits the cloud of induced microearthquakes. It can be used to determine the hydraulic diffusivity  $D$  of the hydraulically stimulated reservoir. Rearranging of Equation (2.4) provides  $D = 0.17 \text{ m}^2/\text{s}$  as the most representative estimation.

In a second example, microseismic data were collected at the European Hot-Dry-Rock geothermal reservoir test site in Soultz-sous-Forêts (France). A series of hydraulic stimulations using several boreholes have been performed between 1989 and 2004. Figure 2.2(a) shows source locations of about 12,000 microearthquakes which were induced during the fluid injection experiment in June/July 2000. In this experiment, more than  $22,000 \text{ m}^3$  fluid (brine and water) were injected within six days using stepwise increasing flow rates which caused a slight build-up of wellhead injection pressures from  $11 \text{ MPa}$  to  $14 \text{ MPa}$  (Dyer, 2001). At the time of injection stop, the microseismicity cloud covers a rock volume of approximately  $500 \times 1600 \times 1200 \text{ m}^3$ , its principal direction strikes  $N156^\circ$  and it dips  $W72^\circ$ . The corresponding  $r - t$  diagram of the induced microearthquakes is shown in Figure 2.2(b). The triggering front curve provides an estimate for hydraulic diffusivity of  $D = 0.15 \text{ m}^2/\text{s}$ .

Occasionally, the assumption of isotropic conditions in respect to fluid transport properties is not fulfilled in real situations. One can recognize from both presented examples that the distribution of microearthquakes hypocenters is to some extent aligned to pre-existing structures, such as fractures, joints and faults. This clearly demonstrates a preferred direction of fluid migration primarily parallel to the direction of maximal horizontal stress. It can be inferred from this observation that the reservoir rock is anisotropic in respect to its fluid transport properties. In a homogeneous but anisotropic medium, the diffusion equation can be written in a more general form:

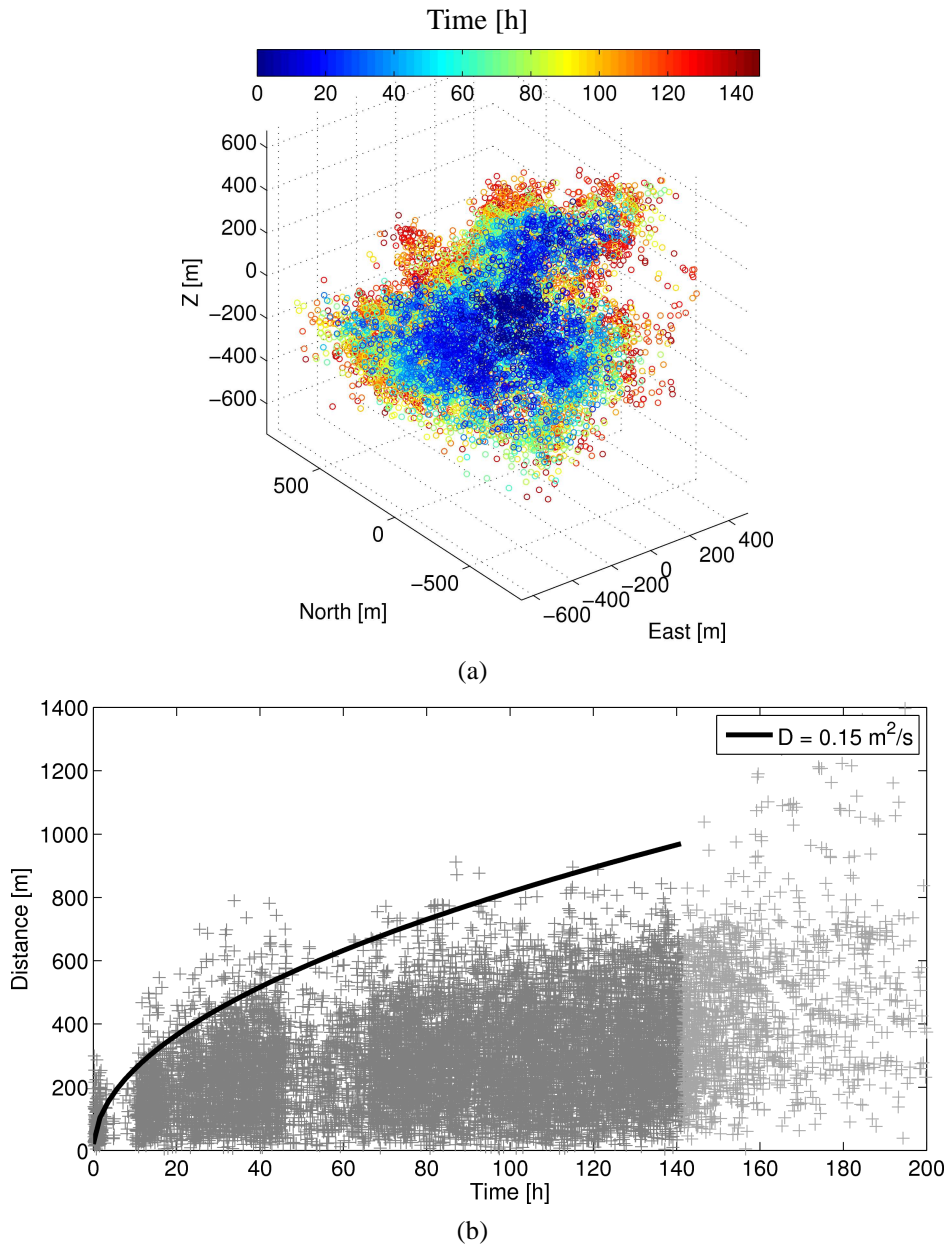


Figure 2.2: Microearthquakes induced during a hydraulic stimulation of a geothermal reservoir in Soultz-sous-Forêts, France. In June/July 2000, about  $22,000 \text{ m}^3$  water were injected at wellhead pressures between 11 and 14 MPa. During the 141 h injection period, about 12,000 locatable microearthquakes were detected. (a) Distribution of source locations (color corresponds to event occurrence time after the begin of injection) and (b) corresponding  $r - t$  diagram. Co-injection seismicity is shown in dark grey color, post-injection seismicity in light grey color. Solid black line denotes triggering front curve according to Equation (2.4). The estimated hydraulic diffusivity is  $D = 0.15 \text{ m}^2/\text{s}$ .

$$\frac{\partial p}{\partial t} = D_{ij} \frac{\partial}{\partial x_i} \frac{\partial}{\partial x_j} p \quad i, j = 1, 2, 3, \quad (2.5)$$

which takes into account the directional dependence of hydraulic diffusivity. Then, in anisotropic media the triggering front equation takes the following form (Shapiro et al., 1999) :

$$r = \sqrt{\frac{4\pi t}{\vec{n}^T D_{ij}^{-1} \vec{n}}}. \quad (2.6)$$

Here  $D_{ij}^{-1}$  is the inverse of the diffusivity tensor and  $\vec{n}^T$  is the transposed of  $\vec{n} = \vec{r}/|\vec{r}|$ . Equation (2.6) can be rewritten in the principal coordinate system of the diffusivity tensor (i.e.  $D_{ij}$  becomes diagonal):

$$\frac{x_1^2}{D_{11}} + \frac{x_2^2}{D_{22}} + \frac{x_3^2}{D_{33}} = 4\pi t. \quad (2.7)$$

Scaling the  $x_i$  coordinates by  $\sqrt{4\pi t}$  one obtains an ellipsoidal equation for the triggering front:

$$x_{si} = \frac{x_i}{\sqrt{4\pi t}} \quad \implies \quad \frac{x_{s1}^2}{D_{11}} + \frac{x_{s2}^2}{D_{22}} + \frac{x_{s3}^2}{D_{33}} = 1, \quad (2.8)$$

with its half-axes equal to the square roots of the principal values of diffusivity  $D_{ii}$ .

Let us again have a look at the two examples of fluid-induced microseismicity. The following results are obtained if the real reservoir conditions are approximated by an anisotropic medium. For both injection sites, Fenton Hill as well as Soultz-sous-Forêts, an ellipsoid which encloses the majority of microearthquakes is defined using the algorithm proposed by Rindschwentner (2001). According to Equation (2.8), the principal components of the tensor of hydraulic diffusivity can be derived from such an ellipsoidal envelope. The ellipsoid presented in Figure 2.3(a) is obtained as best-fit solution for the scaled seismicity cloud induced during the reservoir stimulation in Fenton Hill. In source location coordinate system it is defined by a strike direction of  $N340^\circ$  and a dip of  $E63^\circ$ . The ellipsoid is represented by the tensor of hydraulic diffusivity  $\mathbf{D} = \text{diag}(0.7, 2.0, 0.9) \cdot 10^{-1} m^2/s$ . Figure 2.3(b) shows the ellipsoid for the cloud of microearthquakes induced during the hydraulic stimulation in Soultz-sous-Forêts. In this case, it is oriented  $N156^\circ$  but its longest half-axis is in near vertical plane. In fact, the dip angle of the ellipsoid is  $W80^\circ$ . The tensor of diffusivity is found to be  $\mathbf{D} = \text{diag}(0.4, 1.6, 3.2) \cdot 10^{-1} m^2/s$ .

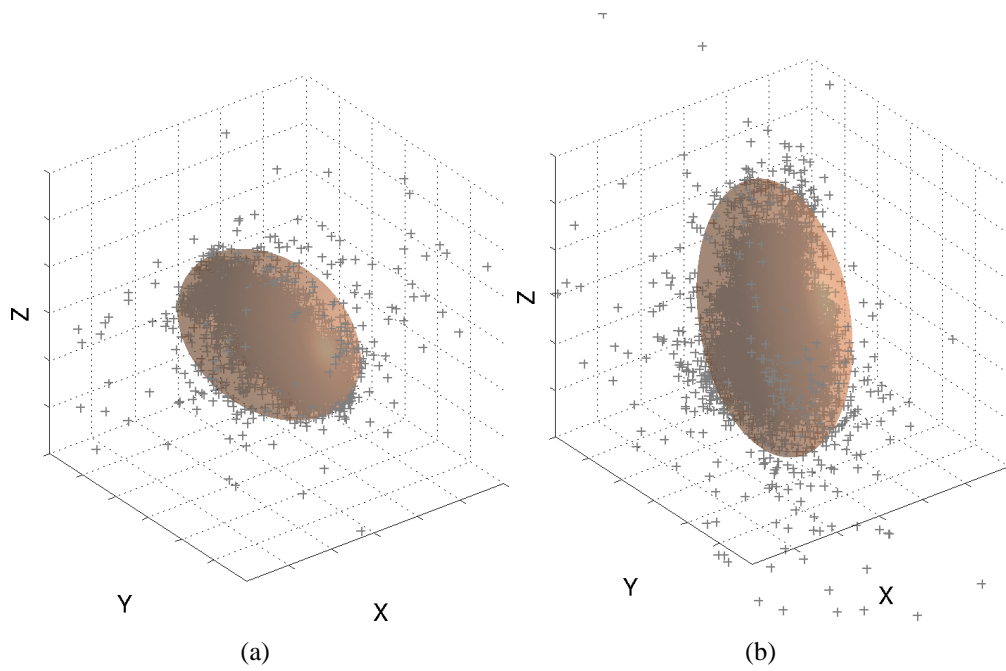


Figure 2.3: Cloud of microearthquakes together with fitting ellipsoid with its half-axes representing the tensor of hydraulic diffusivity. Source coordinates are scaled by  $\sqrt{4\pi t}$  and rotated to principal coordinate system  $(X, Y, Z)$  of the diffusivity tensor. The center of ellipsoid is the injection source point. (a) Fenton Hill and (b) Soultz-sous-Forêts.

### 2.3 Triggering Controlled by Non-Linear Pore Pressure Diffusion

Recently published works by Shapiro and Dinske (2009a) and Shapiro and Dinske (2009b) have shown that the triggering of seismicity described in the previous section can be seen as an asymptotic situation of a rather general non-linear diffusion problem. The relaxation of a pore pressure perturbation due to fluid injections can be explained using the two following fundamental equations. One of those expresses the conservation of mass, that is the continuity equation:

$$\frac{\partial \phi \rho}{\partial t} = -\nabla \vec{U} \rho, \quad (2.9)$$

with  $\phi$  being the porosity of the rock,  $\rho$  being the density and  $\vec{U}$  the filtration velocity of a pore fluid. The second one is Darcy's law:

$$\vec{U} = -\frac{K}{\eta} \nabla p. \quad (2.10)$$

In this equation, the filtration velocity is related to a pore pressure perturbation which is factorized by the tensor of rock permeability,  $K$ , and the dynamic viscosity of the pore fluid,  $\eta$ . In Equation (2.9), the time dependency of  $\phi \rho$  should be proportional to the perturbation of pore pressure  $p$  and it can be replaced by  $\phi \rho = \rho_0 p S$ , where  $\rho_0$  is a reference fluid density and  $S$  is a poroelastic compliance (Shapiro and Dinske, 2009b). Both Equation (2.9) and Equation (2.10) can be combined to derive a general diffusion equation:

$$\frac{\partial p}{\partial t} = \frac{\rho}{\rho_0 S} \nabla \left( \frac{K}{\eta} \nabla p \right). \quad (2.11)$$

Introducing hydraulic diffusivity  $D = \frac{\rho K}{\rho_0 \eta S}$  and considering a  $d$ - dimensional spherically coordinate system with the center at the injection point, then the following equation is obtained:

$$\frac{\partial p}{\partial t} r^{d-1} = \frac{\partial}{\partial r} D r^{d-1} \frac{\partial}{\partial r} p. \quad (2.12)$$

Due to non-linearities of fluid-rock interaction permeability and hence hydraulic diffusivity become pressure dependent. This pressure dependency is assumed to be of a power-law type, that is  $D = D(p) = (n + 1) D_0 p^n$ , where  $n$  is an index of the grade of non-linearity (Shapiro and Dinske, 2009b):  $n = 0$  corresponds to the problem of linear diffusion whereas a large  $n$  describes the problem of strongly pressure dependent diffusion.

If a non-linear diffusion process is described by Equation (2.12), then a general form of the triggering front can be derived using Barenblatt dimensional analysis (Barenblatt, 1996; Shapiro and Dinske, 2009b):

$$r_t \propto D_0 Q_0^n t^{n(i+1)+1}. \quad (2.13)$$

Here the quantity  $Q_0$  is defining the strength of the injection source, that is  $Q_0 = Q_i(t)/((i+1)SA_d t^i)$  under the assumption of a power-law type flow rate  $Q_i(t)$ . The factor  $A_d$  is a geometrical constant with values corresponding to the dimension of the problem under consideration, which means, if  $d = 1, 2$ , or  $3$  then  $A_d = 2A_r, 2\pi h$ , or  $4\pi$  ( $A_r$  is the cross section of an infinite straight rod,  $h$  is height of a homogeneous plain layer). If, for example, the flow rate of an injection is constant and a diffusional process takes place in a  $3D$  space, then the source strength is  $Q_0 = Q_i/4\pi S$  and it has dimension of  $[Pa \cdot m^3 s^{-1}]$ .

The generality of relation (2.13) is shown in the following considerations. If the hydraulic diffusivity is independent on pressure, then the non-linearity index  $n$  equals zero. In such condition, relation (2.13) simplifies to  $r_t \propto \sqrt{Dt}$ . This corresponds to the 'classical' triggering front equation (see Equation (2.4)) in the case of microearthquake triggering by linear pore pressure diffusion. For strongly non-linearities of the diffusion process the general triggering front takes the form  $r_t \propto (Q_0 t^{(i+1)})^{1/d}$ . This proportionality represents the seismicity triggering front which is valid for both 'classical' one-dimensional hydraulic fracturing as well as volumetric three-dimensional hydraulic fracturing.

### **Fluid-Rock Interaction and its Effect on Hydraulic Fracturing**

A single-planar hydraulic fracture is the most simple type of fluid-forced fracturing of reservoir rock. The created hydraulic fracture, however, can become more complex depending on characteristics of the pre-existing natural fracture system. If, for example, multiple diverse-oriented natural fracture networks exist in the reservoir, then the fluid migrates in those different fracture networks and accordingly opens new fracture volume (see Figure 2.4). In such a situation, primary branches (in direction of maximum horizontal stress) and secondary fairways develop (Fisher et al., 2005) and consequently form a 3D hydraulic fracture body.

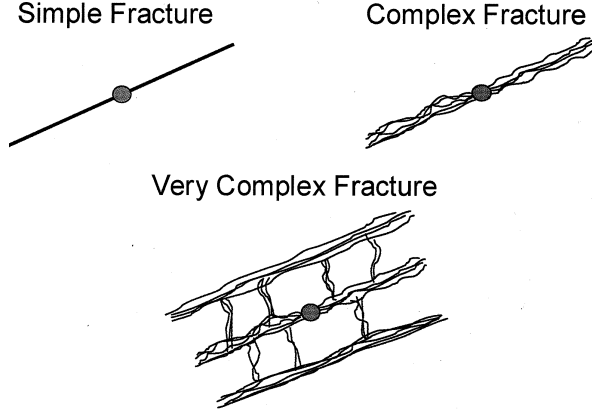


Figure 2.4: Illustration of hydraulic fracture complexity (after Fisher et al., 2005). Fractures can be categorized as simple (classical description), complex, or very complex. The classical description is a single-planar bi-wing crack with the wellbore at the center of the two wings whereas very complex fractures result from interaction of the injected fluid with multiple oriented pre-existing fracture systems.

Let me resume the general relation of the triggering front which is found for the condition of non-linear pressure diffusion:

$$r_t \propto \sqrt[1/(dn+2)]{D_0 Q_0^n t^{n(i+1)+1}}. \quad (2.14)$$

I have mentioned that the index  $n$  describes the grade of non-linearity of a diffusion process. It is intuitively to recognize that by hydraulic fracturing fluid transport properties of the reservoir rock become strongly non-linear which results in the asymptotic situation of  $n \rightarrow \infty$ : The opening of a fracture causes a sudden increase of about several orders of magnitude in permeability. Hence the injected treatment fluid can be transported faster to the fracture tip. This special characteristic implies that the diffusion constant of the diffusion equation becomes pressure dependent as indicated by Equation (2.12). The induced seismicity, as a response to the forced fluid-rock interaction, shows then a typical behavior in its spatio-temporal evolution. If the case of a simple, single-planar hydraulic fracture is considered, then the dimensionality index  $d$  equals 1 and relation (2.14) simplifies to:

$$r_t \propto Q_0 t^{i+1} = \frac{Q_I t^{i+1}}{A_r (i+1) S t^i}, \quad (2.15)$$

and for constant injection flow rate ( $i = 0$ ), it further reduces to:

$$r_t \propto Q_0 t = \frac{Q_I t}{A_r S}, \quad (2.16)$$

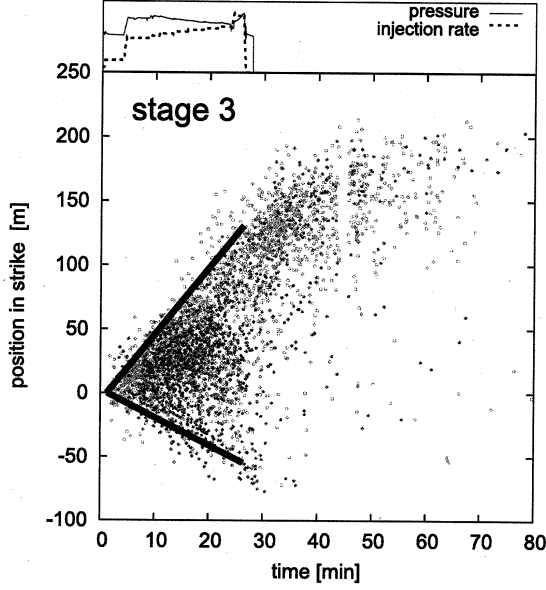


Figure 2.5:  $r-t$  diagram of microearthquakes induced during hydraulic fracturing of tight gas sandstone formation. The linear with time growth of the microseismicity cloud indicates that the created fracture body can well be described as a single-planar (simple) fracture. Figure is taken from Fischer et al. (2008).

The two expressions show that the position of the triggering front  $r_t$  is controlled by the injected fluid volume  $V_I = Q_I t$ . This is in agreement with the interpretational model that I will introduce in Chapter 4. Additionally, they suggest a linear proportionality between growth of a microseismicity cloud and injection time. This characteristic feature is indeed observed. Figure 2.5 exemplifies a  $r-t$  diagram of microearthquakes resulting from hydraulic fracturing in tight-gas sandstone reservoir. Evidently, the fracturing-induced microseismicity is linearly correlated in its spatio-temporal evolution during injection.

Let us now consider the case of volumetric hydraulic fracturing resulting in the very complex fracture type as illustrated in Figure 2.4. In such a situation, the dimensionality is  $d = 3$  and relation (2.14) then takes the form:

$$r_t \propto \sqrt[3]{Q_0 t^{i+1}} = \sqrt[3]{\frac{Q_I t^{i+1}}{4\pi(i+1)S t^i}}, \quad (2.17)$$

respectively:

$$r_t \propto \sqrt[3]{Q_0 t} = \sqrt[3]{\frac{Q_I t}{4\pi S}}, \quad (2.18)$$

if the flow rate is kept constant during injection. Again, the two relations demonstrate a link between seismicity triggering front, or in other words, the outer limit of the seismically active region, and injected fluid volume. In contrast to single-planar fractures, the position of the triggering front here depends on the

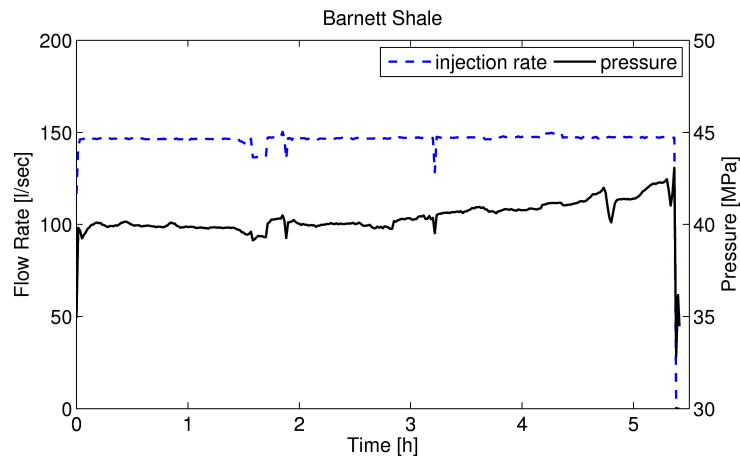


Figure 2.6: Hydraulic treatment data of a fracturing stage in Barnett Shale formation in Fort Worth Basin, Texas.

cubic root of injection time respectively on the cubic root of injected fluid volume.

To emphasize the relations found for seismicity triggering fronts by volumetric hydraulic fracturing one more case study of induced microseismicity is considered. Here I present part of data that were collected during a large fracture diagnostic project undertaken in Summer 2001 in Fort Worth Basin, Texas (USA) (Maxwell et al., 2009). The project was aimed to provide a clearer understanding of the highly complex fracture behavior in the Barnett Shale formation (Fisher et al., 2005). The gas-bearing shale rock is characterized by a porosity of three to five percent and an extremely low permeability of the order of  $10^{-21} - 10^{-19} \text{ m}^2$  (1 – 100 *nanoDarcy*) (S. Maxwell, *personal comm.*). Hydraulic fracturing is therefore extensively used to produce gas from the practically impermeable Barnett Shale formation.

In the following, one particular fracture treatment is considered in more detail. During approximately 5.5 h of injection, 2840  $\text{m}^3$  of water were pumped at high flow rates of about 150  $\text{l/s}$  (Figure 2.6). The measured injection wellhead pressure slightly increased from 40  $\text{MPa}$  to 42  $\text{MPa}$  during the treatment. About 900 locatable microearthquakes, from which 844 occurred during injection, were recorded by the installed seismic monitoring system. The temporal evolution of induced microearthquakes is illustrated in Figure 2.7 and Figure in 2.8. The evolution clearly demonstrates that the injected fluid opens a complex fracture network in the shale formation which is indicated by the non-planar growth of the microseismicity cloud in all three dimensions.

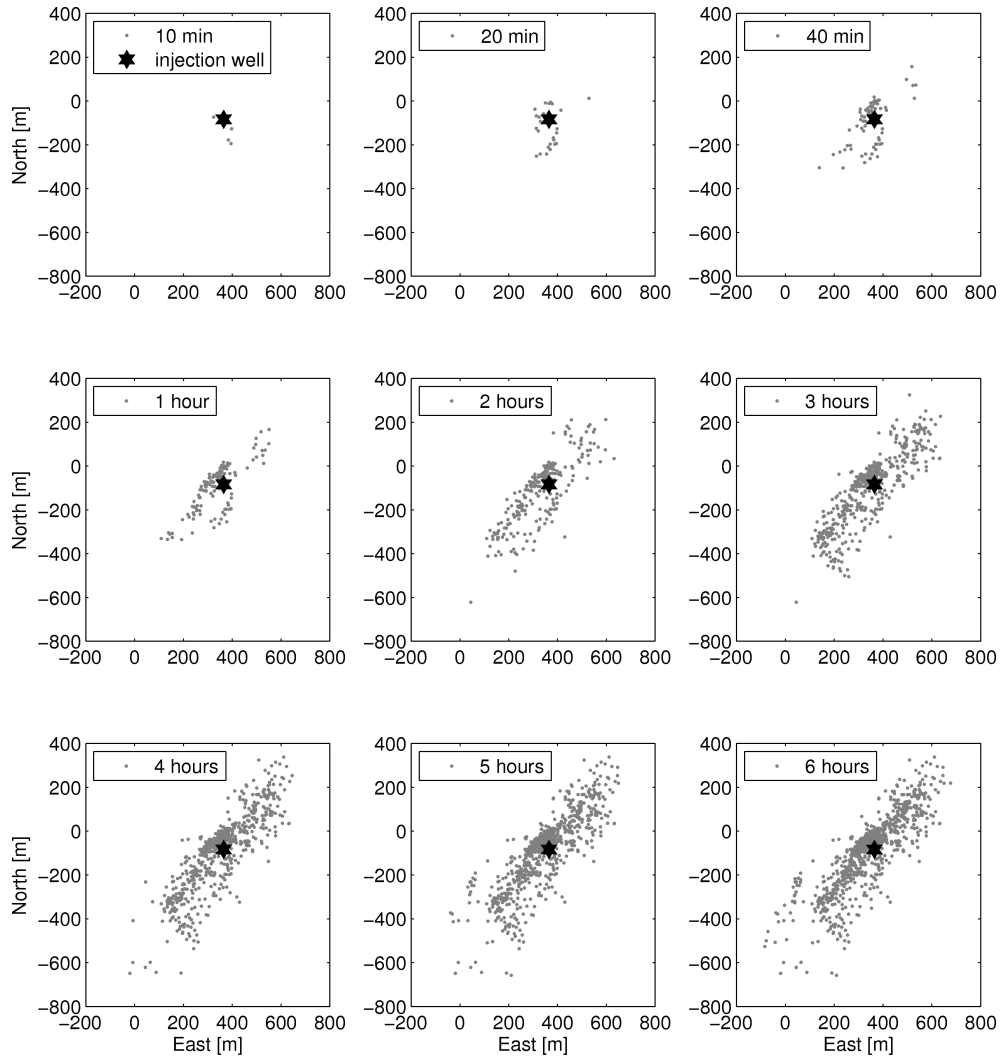


Figure 2.7: Map view of microseismicity resulting from hydraulic fracturing in Barnett Shale. Time slices showing the temporal evolution of the cloud. They indicate that the pressurized fluid opens a very complex pre-existing fracture network within the reservoir formation.

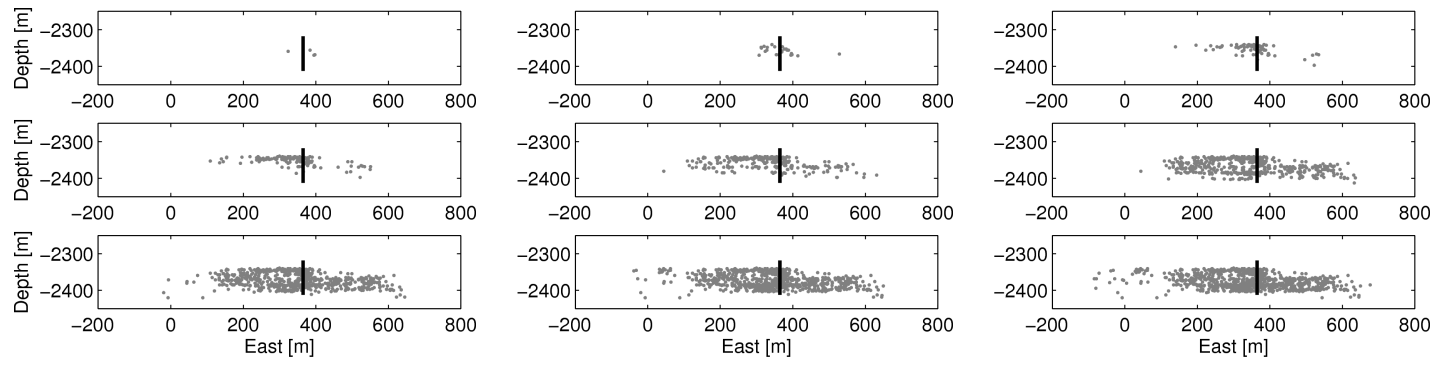


Figure 2.8: Depth view of microseismicity resulting from hydraulic fracturing in Barnett Shale. Again, time slices are shown as in Figure 2.7.

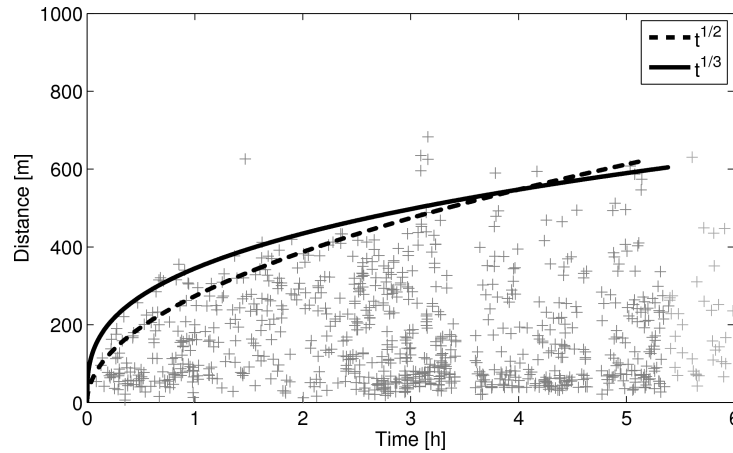


Figure 2.9:  $r - t$  diagram of microearthquakes induced during hydraulic fracturing in Barnett Shale. Co-injection seismicity is shown in dark grey color, post-injection seismicity in light grey color. Dashed black line denotes triggering front curve according to Equation (2.4), whereas solid black line denotes position of the triggering front according to relation (2.18). The latter provides a better fit to the data confirming the cubic root dependency on time in case of volumetric hydraulic fracturing.

This volumetric growth of fracture and related microseismicity therefore implies that the position of the triggering front should obey the cubic root dependency in a  $r - t$  diagram. Figure 2.9 shows the microearthquakes in space-time domain. One can clearly observe that the upper envelope of the microseismicity cloud does not follow a square root of time dependence but rather the expected cubic root dependency.

## 2.4 Seismicity Back Front

So far I have discussed the occurrence of microearthquakes associated with an active fluid injection. However, one could have noticed from the presented case studies that fluid-induced microseismicity continues after the stop of injection. This observation can be explained with the concept of the back front of microseismicity. It was introduced by Parotidis et al. (2004) based on the idea of pore pressure diffusion.

It is assumed that post-injection microseismic events are also triggered by a

diffusional process of relaxation of pore pressure perturbations. Intuitively, decreasing pore pressures lead to rock strengthening and therefore only positive changes of pore pressure perturbations are able to induce microseismicity. It means that no further microearthquakes can occur in a point  $r = \sqrt{x^2 + y^2 + z^2}$  of the medium after the pore pressure perturbation  $p(r, t)$  has reached its maximal value. In other words, the spatio-temporal position of the pore pressure maximum after injection stop defines the minimal distance of a microearthquake to occur. This distance defines the back front of fluid-induced seismicity  $r_{bf}(t)$ . In a space-time diagram of the induced microearthquakes it corresponds to the lower envelope of post-injection seismicity.

To find a mathematical formulation for the back front of induced seismicity, one has to consider the analytical solution of the diffusion equation of pore pressure perturbation. Let us assume, for example, that the pore pressure is perturbed only in one dimension,  $r = x$ . If a isotropic, homogeneous, porous medium is considered, then the solution of the diffusion equation for times smaller than the shut-in time ( $t \leq t_0$ ) is given by Carslaw and Jaeger (1973):

$$p(x, t) = q_0 \sqrt{\frac{t}{\pi D}} \cdot \exp\left(\frac{-x^2}{4Dt}\right) - q_0 \frac{x}{2D} \cdot \operatorname{erfc}\left(\frac{x}{\sqrt{4Dt}}\right), \quad (2.19)$$

whereas for times larger than the shut-in time ( $t > t_0$ ) the following solution can be derived:

$$\begin{aligned} p(x, t > t_0) &= U - V && \text{with :} && (2.20) \\ U &= q_0 \left( \sqrt{\frac{t}{\pi D}} \cdot \exp\left(\frac{-x^2}{4Dt}\right) - \sqrt{\frac{t-t_0}{\pi D}} \cdot \exp\left(\frac{-x^2}{4D(t-t_0)}\right) \right) \\ V &= q_0 \frac{x}{2D} \cdot \left( \operatorname{erfc}\left(\frac{x}{\sqrt{4Dt}}\right) - \operatorname{erfc}\left(\frac{x}{\sqrt{4D(t-t_0)}}\right) \right). \end{aligned}$$

In the two equations,  $\operatorname{erfc} = 1 - \operatorname{erf}$  is the complementary Gaussian error function and  $q_0$  is the strength of an injection point source. The pore pressure maximum, which separates regions of positive and negative pore pressure changes, corresponds to the mathematical condition that the time derivative of Equation (2.20) equals zero:

$$\frac{\partial p(x, t > t_0)}{\partial t} = \frac{q_0}{\sqrt{4\pi Dt}} \cdot \exp\left(\frac{-x^2}{4Dt}\right) - \frac{q_0}{\sqrt{4\pi D(t-t_0)}} \cdot \exp\left(\frac{-x^2}{4D(t-t_0)}\right) = 0. \quad (2.21)$$

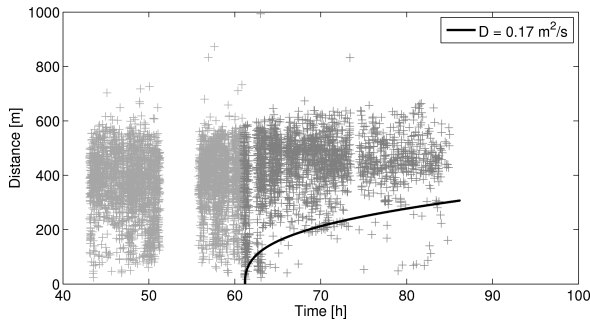
Solving this condition for distances  $x$  provides the equation for the back front of fluid-induced seismicity:

$$x_{bf}(t) = \sqrt{2D t \left(\frac{t}{t_0} - 1\right) \ln\left(\frac{t}{t - t_0}\right)}. \quad (2.22)$$

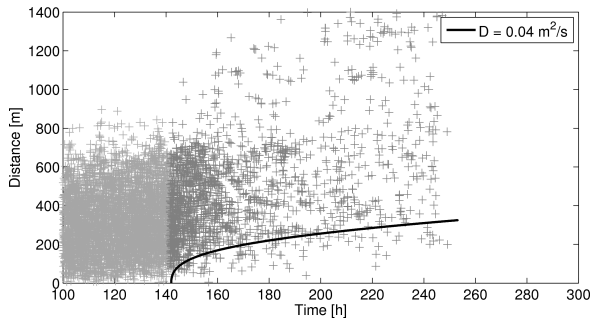
The diffusion constant  $D$  represents the diffusivity  $D_f$  of hydraulically stimulated systems. The back front of seismicity can therefore be evaluated for characterizing fluid transport properties of a reservoir. Equation (2.22) is similar to those equations which have been derived by Parotidis et al. (2004) under consideration of a diffusion problem in two-dimensional and in three-dimensional space, respectively:

$$\begin{aligned} 2D : \quad r_{bf}(t) &= \sqrt{4D t \left(\frac{t}{t_0} - 1\right) \ln\left(\frac{t}{t - t_0}\right)}, \\ 3D : \quad r_{bf}(t) &= \sqrt{6D t \left(\frac{t}{t_0} - 1\right) \ln\left(\frac{t}{t - t_0}\right)}. \end{aligned} \quad (2.23)$$

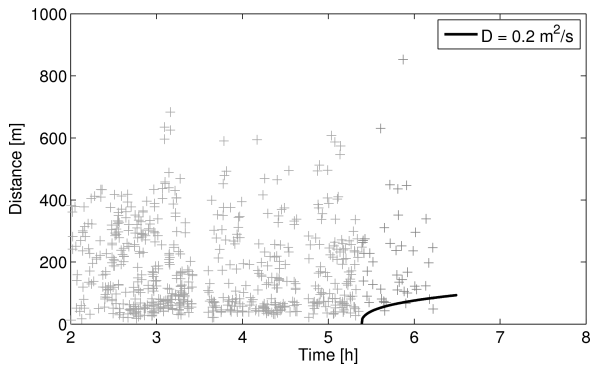
Let me go back to the examples of fluid-induced microseismicity from Fenton Hill, Soultz-sous-Forêts, and Barnett Shale. The  $r - t$  diagrams presented in Figure 2.10 show a part of clouds of induced microearthquakes of the three data sets. Following the injection stop, a region of seismic inactivity evolves at the borehole and then enlarges with ongoing time. According to the concept of seismicity back front, this region is the area where pore pressure is decreasing and triggering of microearthquakes becomes improbable. In the presented case studies, the back front signature is clearly developed in the presented examples. It can further be used to determine the hydraulic diffusivity as it is indicated by Equation (2.22)/(2.23) which should be of the same order of magnitude as the diffusivity estimate obtained from the seismicity triggering front signature.



(a)



(b)



(c)

Figure 2.10:  $r - t$  diagrams of induced microearthquakes resulting from hydraulic stimulation respectively fracturing of a reservoir. To emphasize the back front signature only a part of the induced microseismicity cloud is presented. Co-injection seismicity is shown in light grey color, post-injection seismicity in dark grey color. Solid black lines denote back front curve according to Equation (2.22)/(2.23). (a) Fenton Hill: seismicity back front provides hydraulic diffusivity  $D = 0.17 \text{ m}^2/\text{s}$  which is equal to the estimate from triggering front in isotropic approximation. (b) Sultz-sous-Forêts: hydraulic diffusivity  $D = 0.04 \text{ m}^2/\text{s}$  is equal to least principal component of diffusivity tensor obtained from triggering front in anisotropic approximation. (c) Barnett Shale: seismicity back front provides hydraulic diffusivity  $D = 0.2 \text{ m}^2/\text{s}$  characterizing the permeability of the created fracture.

# Chapter 3

## Seismicity Induced by Fluid Injections with Time-Dependent Source Strength

### 3.1 Introduction

In the previous chapter, it was shown that triggering mechanisms of fluid-induced seismicity can well be approximated with a diffusional process of relaxation of pore pressure perturbations which are caused by the injected fluid. An analysis of spatial and temporal dynamics of the induced seismicity supports this conclusion and contributes to the understanding of underlying physical processes. Typical signatures that confirm the diffusive nature are, for example, the parabola-like triggering front and back front of seismicity. Further evidences are related to the seismicity rate, to the spatial event density distribution, and to the characteristics of magnitudes of microseismic events. Based on the concept of pressure diffusion, the so-called *SBRC* approach (Seismicity Based Reservoir Characterization) was introduced (e.g. Shapiro et al., 1997, 2002, 2003, 2005). It combines heuristic as well as deterministic methods for analyzing microseismic data which can generally be used to estimate the fluid transport properties of a hydraulically stimulated reservoir.

In the deterministic analysis, the main hypothesis of the *SBRC* approach, that is pore pressure diffusion as the controlling process for seismicity triggering, is described by a statistical model (Parotidis and Shapiro, 2004; Shapiro et al., 2005). The probability  $P(Ev, \vec{r}, t)$  of a microearthquake to occur until a given time  $t$  and location  $\vec{r} = (x, y, z)$  is equal to  $P(C(\vec{r}) \leq p(r, t))$ . It means that this occurrence probability is equal to the probability of the critical pore pressure  $C(\vec{r})$  necessary for triggering a microearthquake to be smaller than or equal to the pore pressure

perturbation  $p(r, t)$ . Under the condition that the injection-induced pore pressure perturbation is a non-decreasing function this probability becomes:

$$P(Ev, r, t) = \int_0^{p(r,t)} f(C) dC. \quad (3.1)$$

In this equation,  $f(C)$  is the probability density function (*PDF*) of critical pore pressure. It is given as  $f(C) = 1/(C_{max} - C_{min}) = 1/dC$ , if a uniform distribution of criticality  $C(\vec{r})$  is assumed. The criticality field characterizes the strength of pre-existing fractures at which shear events can occur. It is bounded by  $C_{max}$ , specifying most stable, and  $C_{min}$ , specifying most unstable fractures, respectively. In this case, Equation (3.1) results in:

$$P(Ev, r, t) = p(r, t)/dC. \quad (3.2)$$

This equation shows that the probability of triggering a microearthquake is directly proportional to the pore pressure perturbation. The pore pressure perturbation  $p(r, t)$  can be obtained by solving the partial differential equation of diffusion. Analytical solutions of the diffusion equation are known for the condition of constant strength of a fluid injection source (Carslaw and Jaeger, 1973). This special condition is approximately fulfilled by several hydraulic reservoir stimulations (for instance, in Fenton Hill (House, 1987), in Ogachi (Hori et al., 1999) and at the KTB site (Shapiro et al., 2006b)). However, in cases where the constant source condition does not meet the design parameters of an injection experiment the application of *SBRC* methods under the assumption of constant source strength would give inaccurate results. Such a situation applies to, for example, the reservoir stimulation performed in Basel in December 2006, where flow rates have been increased in several steps which caused an injection pressure build-up from 10 *MPa* to 30 *MPa* (Häring et al., 2008).

In this chapter, an analytical solution of the diffusion equation is presented which considers the special problem of a linearly increasing injection source strength. The obtained solution is then used to find mathematical expressions for the seismicity rate and for the cumulative number of induced microearthquakes. Next, the derived equations are verified by numerically solving the diffusion equation and then generating synthetical microseismicity. In the third part of this chapter, heuristic as well as the modified deterministic *SBRC* methods will be applied to the microseismic data collected during the hydraulic stimulation of the Basel geothermal reservoir. The different methods allow for independently estimating the hydraulic diffusivity respectively permeability on a field-scale. In addition, the *SBRC* methods enable an evaluation of the stability of pre-existing fracture systems of the stimulated reservoir by reconstructing the critical pressures of induced microearthquakes.

## 3.2 Analytical Formulations

Before the case of a time-dependent source strength of fluid injections is considered, I will begin this section with a brief review of the fundamental equations which are valid for the condition of constant source strength.

### 3.2.1 Pore Pressure Perturbation Resulting From Constant Injection Source Strength

In Chapter 2.2, it was already shown that in homogeneous, isotropic, fluid-saturated, porous media the partial differential equation of linear pressure diffusion is given as:

$$\frac{\partial p(r, t)}{\partial t} = D \nabla^2 p(r, t), \quad (3.3)$$

with pore pressure perturbation  $p(r, t)$ , scalar hydraulic diffusivity  $D$  and distance to the source point  $r = \sqrt{x^2 + y^2 + z^2}$ . If an injection point source with constant strength  $q$  switched on at time  $t = 0$  is considered, then the solution of the diffusion equation in 3D space becomes (Carslaw and Jaeger, 1973):

$$p(r, t) = \frac{q}{4\pi D r} \cdot \operatorname{erfc} \left( \frac{r}{\sqrt{4Dt}} \right), \quad (3.4)$$

where  $\operatorname{erfc}(z) = 1 - \operatorname{erf}(z) = 2/\sqrt{\pi} \int_z^\infty e^{-t^2} dt$  is the complementary Gaussian error function. Rothert and Shapiro (2007) have shown that in real situations the point source condition can be approximated by an equivalent source strength  $q = q_0 = 4\pi D a_0 p_0$ , where  $a_0$  is the radius of a spherical surface on which a constant injection pressure  $p_0$  is applied. In the case of a finite injection source switched off at time  $t = t_0$  the 3D solution of the diffusion equation for times  $t > t_0$  becomes (Parotidis et al., 2004) (see also Figure 3.1):

$$p(r, t > t_0) = \frac{q}{4\pi D r} \cdot \left[ \operatorname{erfc} \left( \frac{r}{\sqrt{4Dt}} \right) - \operatorname{erfc} \left( \frac{r}{\sqrt{4D(t-t_0)}} \right) \right]. \quad (3.5)$$

Both Equation (3.4) and Equation (3.5) allow to analytically calculate the pore pressure perturbation which is caused by a fluid injection with a constant injection pressure. In the next section, it will be shown how these equations change if the applied injection pressure becomes time-dependent.

### 3.2.2 Pore Pressure Perturbation Resulting From Non-Constant Injection Source Strength

Now, a solution of the diffusion equation will be derived where a non-constant injection source strength is taken into account. In particular, the special problem of linearly increasing injection pressures during the hydraulic treatment will be considered. Generally, a solution of Equation (3.3) for point sources has the form (Carslaw and Jaeger, 1973):

$$p(r, t) = \frac{1}{8(\pi D)^{3/2}} \int_0^t \psi(\tilde{t}) e^{\frac{-r^2}{4D(t-\tilde{t})}} \frac{1}{(t-\tilde{t})^{3/2}} d\tilde{t}. \quad (3.6)$$

The source variable can be written as  $\psi(t) = q_0 + q_t t$  with  $q_0$  being a time-independent constant source strength, which can also be zero, and  $q_t$  being the rate of source strength increase, which is assumed to be a constant gradient. The source strength  $\psi(t)$  is hence a linear with time increasing function. The solution for the constant term  $q_0$  is known (see Chapter 3.2.1), it is therefore sufficient to consider the time-dependent term only:

$$p(r, t) |_{nonconst} = \frac{q_t}{8(\pi D)^{3/2}} \int_0^t \tilde{t} e^{\frac{-r^2}{4D(t-\tilde{t})}} \frac{1}{(t-\tilde{t})^{3/2}} d\tilde{t}. \quad (3.7)$$

Simplifying the integral by replacing integration variable,  $\tau = (t - \tilde{t})^{-1/2}$ , and solving the integral one obtains:

$$p(r, t) |_{nonconst} = \frac{q_t}{8\pi D^2 r} (r^2 + 2Dt) \cdot \operatorname{erfc}\left(\frac{r}{\sqrt{4Dt}}\right) - \frac{q_t \sqrt{t}}{4(\pi D)^{3/2}} \cdot e^{\frac{-r^2}{4Dt}}. \quad (3.8)$$

Finally, summation of Equation (3.4) and Equation (3.8) gives the analytical solution of the diffusion equation for a time-dependent source function representing a linearly increasing injection pressure:

$$p(r, t) = \left( \frac{q_0 + q_t t}{4\pi D r} + \frac{q_t r}{8\pi D^2} \right) \cdot \operatorname{erfc}\left(\frac{r}{\sqrt{4Dt}}\right) - \frac{q_t \sqrt{t}}{4(\pi D)^{3/2}} \cdot e^{\frac{-r^2}{4Dt}} \quad (3.9)$$

Let us now consider the migration of pore pressure perturbations after switching off the injection source, that is  $p(r, t)$  for times  $t$  larger the injection stop time  $t_0$ . The solution given in Equation (3.9) is valid for continuous sources only. An expression for  $p(r, t > t_0)$  can be found with the following idea which is illustrated in Figure 3.1. The switch-off of the injection source is simulated by a summation of two source functions:

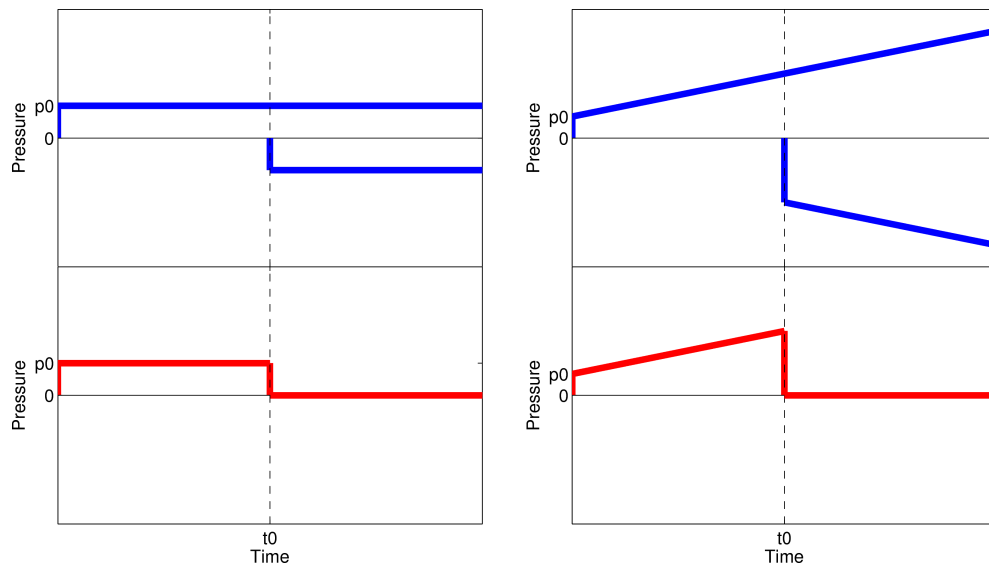


Figure 3.1: Left: Blue lines are continuous pressure functions illustrating the input functions for deriving solutions of the diffusion equation valid for constant sources. For times  $t$  larger than injection stop time  $t_0$  a negative pressure function has to be applied in order to simulate the switch-off of the source. The red line shows the sum of the two input function that gives a source strength of finite time. Right: Equivalent sketch for a linearly increasing source strength.

1.  $q_0 + q_t t$  for all  $t$ , and
2.  $-(q_0 + q_t(t - t_0) + q_t t_0)$  for  $t > t_0$  and zero for  $t \leq t_0$

In such a way, the resulting injection source becomes limited to finite times  $t \leq t_0$  and then the following solution to the problem of non-constant strength is found:

$$p(r, t > t_0) = \left( \frac{q_0 + q_t t}{4\pi D r} + \frac{q_t r}{8\pi D^2} \right) \cdot \operatorname{erfc} \left( \frac{r}{\sqrt{4Dt}} \right) - \frac{q_t \sqrt{t}}{4(\pi D)^{3/2}} \cdot e^{-\frac{r^2}{4Dt}}$$

$$- \left[ \left( \frac{q_0 + q_t(t - t_0) + q_t t_0}{4\pi D r} + \frac{q_t r}{8\pi D^2} \right) \cdot \operatorname{erfc} \left( \frac{r}{\sqrt{4D(t - t_0)}} \right) - \frac{q_t \sqrt{t - t_0}}{4(\pi D)^{3/2}} \cdot e^{-\frac{r^2}{4D(t - t_0)}} \right] \quad (3.10)$$

Both Equation (3.9) and Equation (3.10) completely describe the propagation of a pore pressure perturbation in a 3D volume caused by an injection source of linearly increasing strength and finite time.

To illustrate the differences of the two solutions for constant source and non-constant source, respectively, the pore pressure perturbation  $p(r, t)$  is calculated using the following parameters:

- source terms  $q_0 = 4\pi D a_0 p_0$  and  $q_t = 4\pi D a_0 p_t$  with
  - constant injection pressure  $p_0 = 10 \text{ MPa}$
  - pressure gradient  $p_t = 50 \text{ Pa/s}$
- effective source radius  $a_0 = 1 \text{ m}$
- injection duration  $t_I \leq t_0 = 4 \cdot 10^5 \text{ s}$
- hydraulic diffusivity  $D = 0.05 \text{ m}^2/\text{s}$

Figure 3.2 shows pore pressure profiles as functions of time and distance, respectively. The profile lines for both constant and non-constant source run nearly identical for small times, and they split as expected with ongoing injection duration where the effect of the pressure gradient  $q_t$  becomes increasingly significant. It is evident from the figure that, if non-linear interactions are excluded, the penetration depth of pore pressure perturbations is only controlled by hydraulic diffusivity and injection duration but the magnitude of the perturbation is strongly influenced by the applied injection pressure, in particular in distances close to the source point. This is confirmed by comparing contour maps of pore pressure perturbations which are presented in Figure 3.3.

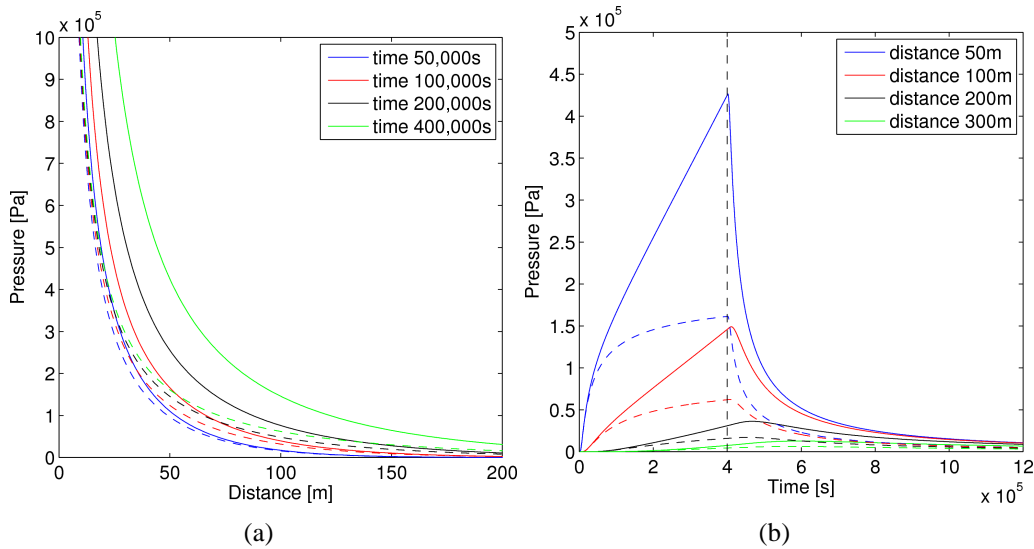


Figure 3.2: (a) Pore pressure profiles for constant injection source pressure (dashed lines) and for linearly increasing injection source pressure (solid lines) as function of distance to source point. (b) Pore pressure profiles as function of time. Vertical dashed line marks time of injection stop.

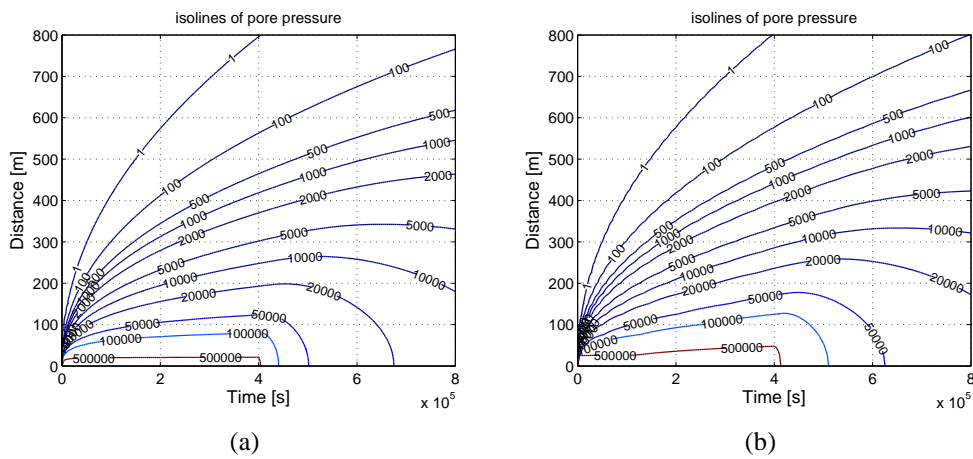


Figure 3.3: (a) Isolines of perturbation of the pore pressure field caused by a constant injection source strength and (b) by linearly increasing injection source strength.

### 3.2.3 Pore Pressure Related Signatures of Fluid-Induced Seismicity

#### Back front of seismicity

In Chapter 2.4, I have already mentioned that occurrence of microseismicity even after stop of an injection is a well known phenomenon. It was observed in many locations of fluid injection, such as in Fenton Hill (Parotidis et al., 2004) and in Soultz-sous-Forêts (Delepine et al., 2004). At first, I briefly recall the concept of the back front of fluid-induced seismicity introduced by Parotidis et al. (2004). Intuitively, microseismic events are only probable if pore pressure increases because a decreasing pore pressure leads to rock strengthening. From Figure 3.3 one can notice that at the time of switching off the source, neither the pore pressure is immediately relaxed nor it is decreasing everywhere in the medium. Therefore microearthquakes can still continue to occur after injection stop but their locations are restricted to the region of positive pore pressure changes. This means that the back front is defined by the isosurface of zero pore pressure changes which separates the domains of positive and negative pressure changes. For a constant source strength, it was shown that the back front of seismicity in a 3D volume is given as:

$$r_{bf} = \sqrt{6Dt\left(\frac{t}{t_0} - 1\right)\ln\left(\frac{t}{t-t_0}\right)}. \quad (3.11)$$

A simple formulation for the back front  $r_{bf}$  where a linearly increasing source strength is considered can not be derived. However, the plot of isolines of changes of pore pressure perturbations  $dp/dt$ , which is presented in Figure 3.4, shows only minor deviation of the isoline of zero change,  $dp/dt = 0$ , from the back front parabola which is calculated according to Equation (3.11). Thus, it is reasonable to conclude that usage of Equation (3.11) results in a negligible inaccuracy. In the following considerations of seismicity rate and cumulative event number, however, I will refer the term back front  $r_{bf}$  to the radius of the isoline / isosurface of zero pore pressure change,  $dp/dt = 0$ .

#### Seismicity rate and cumulative event number

Using the probability based approach (Parotidis and Shapiro (2004)), the solutions of the diffusion equation given in Equation (3.9) and Equation (3.10) allow to calculate the seismicity rate during injection,  $R(t \leq t_0)$ , and after switching off the injection source,  $R(t > t_0)$ , respectively. The seismicity rate is defined as the number of induced events per unit time. The following integral has to be applied to find the expressions for both rates  $R(t \leq t_0)$  and  $R(t > t_0)$ :

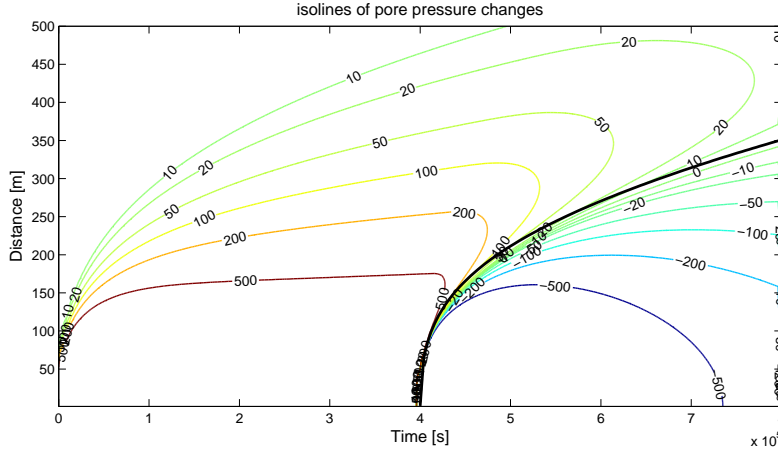


Figure 3.4: Isolines of changes of pore pressure perturbations  $dp/dt$  (colored lines) and back front  $r_{bf}$  according to Equation (3.11) (thick black line). Although this equation is valid for the condition of constant injection source strength one notice only minor differences between the isoline  $dp/dt = 0$  and  $r_{bf}$ .

$$R(t) = \frac{\zeta}{dC} \int_V \frac{\partial p(r, t)}{\partial t} d^3r = \frac{4\pi\zeta}{dC} \int_a^b r^2 \cdot \frac{\partial p(r, t)}{\partial t} dr, \quad (3.12)$$

where  $1/dC = 1/(C_{max} - C_{min})$  is the probability density function of critical pressures  $C(\vec{r})$ . In the statistical model of the triggering of fluid-induced microearthquakes, the criticality specifies the fracture stability which is uniformly distributed between a maximum criticality  $C_{max}$  (most stable fractures) and a minimum criticality  $C_{min}$  (most unstable fractures). The quantity  $\zeta$  is the volume concentration of pre-existing fractures. The integration limits are defined by the seismically active rock volume:  $a$  and  $b$  are the time-dependent radii of isosurfaces of pore pressure perturbation corresponding to the values of maximum and minimum criticality, respectively. For  $t > t_0$ , the radius of the back front replaces the radius of pore pressure iso-surface of the value of  $C_{max}$  in the lower integration limit (Langenbruch and Shapiro, 2009). In Figure 3.5 the time-dependent radii of the seismically active volume are illustrated in a  $r - t$  diagram of fluid-induced microearthquakes.

First, the equation for the seismicity rate before the injection source is switched off is derived. The time derivative of Equation (3.9)

$$\frac{\partial p(r, t)}{\partial t} \Big|_{t \leq t_0} = \frac{q_0}{8(\pi Dt)^{3/2}} \cdot e^{-\frac{r^2}{4Dt}} + \frac{q_t}{4\pi Dr} \cdot \operatorname{erfc}\left(\frac{r}{\sqrt{4Dt}}\right) \quad (3.13)$$

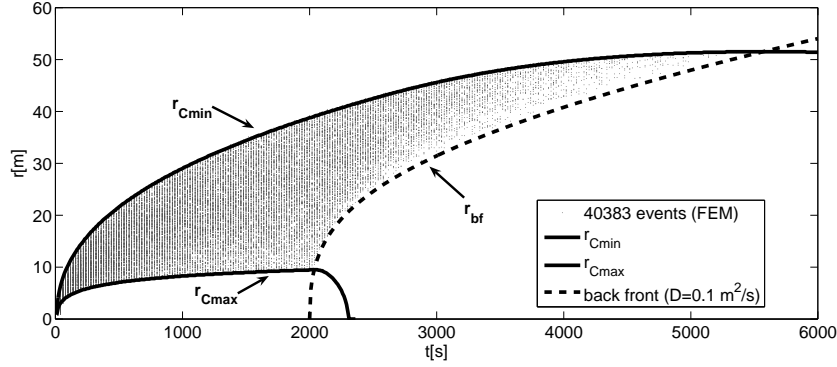


Figure 3.5:  $r - t$  diagram of microearthquakes along with bounds of the seismically active volume: radius of the isosurface of pore pressure perturbation with the value minimum criticality,  $r_{C_{min}}(t)$ , radius of the isosurface of pore pressure perturbation with the value of maximum criticality,  $r_{C_{max}}(t)$ , and radius of back front,  $r_{bf}$  (after Langenbruch and Shapiro, 2009).

is introduced into Equation (3.12) and solving the integral gives the seismicity rate during injection:

$$R(t \leq t_0) = \frac{\zeta}{dC} (R_1 + R_2) \quad \text{with :} \quad (3.14)$$

$$R_1 = -\frac{b(q_0 + q_t t)}{\sqrt{\pi D t}} \cdot e^{-\frac{b^2}{4Dt}} + (q_0 + q_t t - \frac{b^2 q_t}{2D}) \cdot \text{erf}\left(\frac{b}{\sqrt{4Dt}}\right) + \frac{b^2 q_t}{2D}$$

$$R_2 = \frac{a(q_0 + q_t t)}{\sqrt{\pi D t}} \cdot e^{-\frac{a^2}{4Dt}} - (q_0 + q_t t - \frac{a^2 q_t}{2D}) \cdot \text{erf}\left(\frac{a}{\sqrt{4Dt}}\right) - \frac{a^2 q_t}{2D}$$

where  $a$  has to be substituted by  $r_{C_{max}}(t)$  and  $b$  by  $r_{C_{min}}(t)$ . Next, the post-injection period is considered, that is times  $t$  larger than the stop time  $t_0$ . The time derivative of Equation (3.10)

$$\frac{\partial p(r, t)}{\partial t} \Big|_{t > t_0} = \frac{q_0}{8(\pi D t)^{3/2}} \cdot e^{-\frac{r^2}{4Dt}} - \frac{q_0 + q_t t_0}{8(\pi D (t - t_0))^{3/2}} \cdot e^{-\frac{r^2}{4D(t-t_0)}} + \frac{q_t}{4\pi D r} \left[ \text{erfc}\left(\frac{r}{\sqrt{4Dt}}\right) - \text{erfc}\left(\frac{r}{\sqrt{4D(t-t_0)}}\right) \right] \quad (3.15)$$

is introduced into Equation (3.12) and the following expression is obtained for the seismicity rate after switching off the injection source:

$$R(t > t_0) = \frac{\zeta}{dC} \sum_{i=1}^4 U_i - V_i \quad (3.16)$$

$$\begin{aligned} \text{with} \quad U_1 &= \frac{-(b(q_0 + q_t t))}{\sqrt{\pi D} \sqrt{t}} \cdot e^{\frac{-b^2}{4Dt}} \\ U_2 &= (q_0 + q_t t - \frac{b^2 q_t}{2D}) \cdot \text{erf}(\frac{b}{\sqrt{4Dt}}) \\ U_3 &= \frac{a(q_0 + q_t t)}{\sqrt{\pi D} \sqrt{t}} \cdot e^{\frac{-a^2}{4Dt}} \\ U_4 &= -(q_0 + q_t t - \frac{a^2 q_t}{2D}) \cdot \text{erf}(\frac{a}{\sqrt{4Dt}}) \end{aligned}$$

$$\begin{aligned} \text{and} \quad V_1 &= \frac{-(b(q_0 + q_t t))}{\sqrt{\pi D} \sqrt{t - t_0}} \cdot e^{\frac{-b^2}{4D(t-t_0)}} \\ V_2 &= (q_0 + q_t t - \frac{b^2 q_t}{2D}) \cdot \text{erf}(\frac{b}{\sqrt{4D(t-t_0)}}) \\ V_3 &= \frac{a(q_0 + q_t t)}{\sqrt{\pi D} \sqrt{t - t_0}} \cdot e^{\frac{-a^2}{4D(t-t_0)}} \\ V_4 &= -(q_0 + q_t t - \frac{a^2 q_t}{2D}) \cdot \text{erf}(\frac{a}{\sqrt{4D(t-t_0)}}) \end{aligned}$$

where  $a$  has to be substituted by  $\max\{r_{C_{max}}(t), r_{bf}(t)\}$  and  $b$  by  $r_{C_{min}}(t)$ .

Equation (3.14) and Equation (3.16) are full solutions of the integral for the computation of the seismicity rate. Occasionally, it can be useful for the calculation of seismicity rates to consider the whole volume where pore pressure changes occur. It means that the seismically active region is not bounded by values of maximum and minimum criticality:  $C_{max}$  is larger than the maximum injection pressure and  $C_{min}$  equals zero. Such a situation was introduced as a reference case by Langenbruch and Shapiro (2009). The integration limits  $a$  and  $b$  in Equation (3.12) then become 0 and  $\infty$  for times  $t \leq t_0$  respectively  $r_{bf}$  and  $\infty$  for  $t > t_0$ . The solutions of the integral hence simplify to:

$$R(t \leq t_0) = \frac{\zeta}{C_{max}}(q_0 + q_t t) \quad (3.17)$$

and

$$R(t > t_0) = \frac{\zeta}{C_{max}}(U - V) \quad \text{with :} \quad (3.18)$$

$$U = (q_0 + q_t t) \cdot \sqrt{\frac{6}{\pi} \left(\frac{t}{t_0} - 1\right) \ln\left(\frac{t}{t-t_0}\right) \left(\frac{t}{t-t_0}\right)^{-\frac{3}{2} \frac{t}{t_0}} \cdot \left( \left(\frac{t}{t-t_0}\right)^{\frac{3}{2}} - \left(\frac{t}{t-t_0}\right)^{\frac{1}{2}} \right)}$$

$$V = \left( q_0 + q_t t - 3q_t t \left(\frac{t}{t_0} - 1\right) \ln\left(\frac{t}{t-t_0}\right) \right) \cdot \left[ \operatorname{erf} \left( \sqrt{\frac{3}{2} \left(\frac{t}{t_0} - 1\right) \ln\left(\frac{t}{t-t_0}\right)} \right) - \operatorname{erf} \left( \sqrt{\frac{3}{2} \left(\frac{t}{t_0}\right) \left(\frac{t}{t_0} - 1\right) \ln\left(\frac{t}{t-t_0}\right)} \right) \right]$$

The effect of different set-ups of criticality on the seismicity rate is now investigated. This allows to deduce how the rate of seismicity evolves in dependence on the stability of fractures. For this purpose, a reference rate is calculated according to Equation (3.17) and Equation (3.18) and then compared to rates which are calculated according to Equation (3.14) and Equation (3.16) using varying values of minimum and maximum criticality. Figure 3.6 illustrates the result. On the one hand, one can notice that an increased value of minimum criticality leads to fewer events per time-step in relation to the reference rate. The seismicity rate is more gently rising during injection whereas it decays faster in the post-injection period. Therefore a higher minimum criticality addresses as expected a more stable fracture system. On the other hand, values of maximum criticality below the maximum of pore pressure perturbation,  $C_{max} < p(r, t)$ , result in the interesting observation that the rate is still rising even though the injection has already been stopped. Such situations represent rather unstable fracture systems.

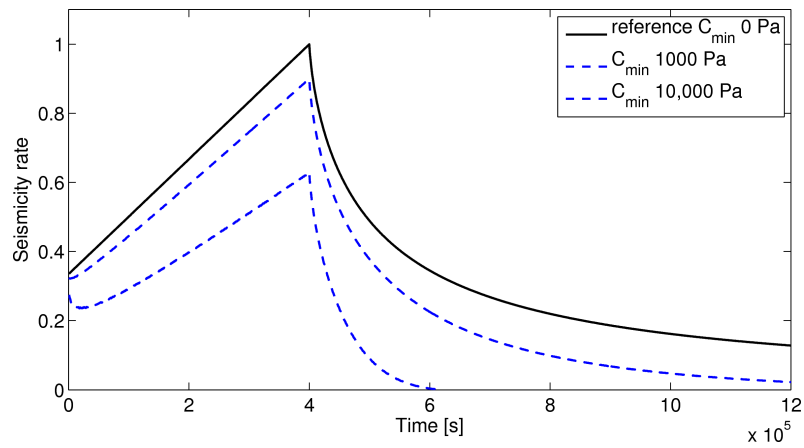
The cumulative number of induced microearthquakes  $N_{ev}$  at a time  $t$  can be obtained by summation of the seismicity rate until time  $t$ . The summation reads in integral form:

$$N_{ev}(t) = \int R(t) dt. \quad (3.19)$$

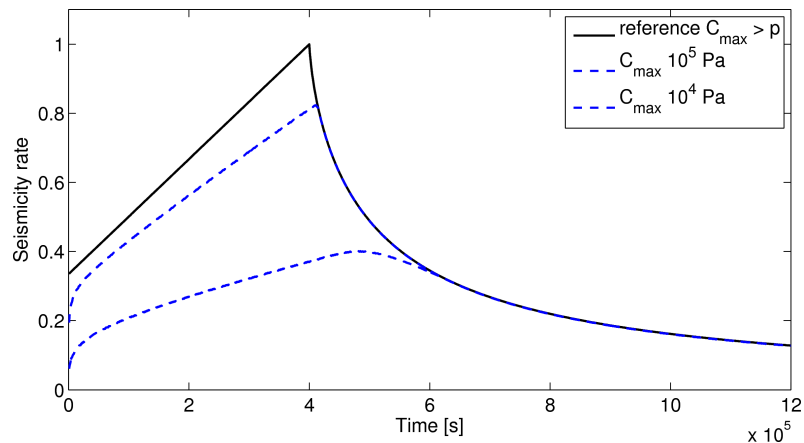
Introducing the definition of seismicity rate, Equation (3.12), yields for the cumulative event number:

$$N_{ev}(t) = \frac{\zeta}{dC} \int_V p(r, t) d^3r = \frac{4\pi\zeta}{dC} \int_a^b r^2 p(r, t) dr \quad (3.20)$$

First, solving the integral for times  $t \leq t_0$  the cumulative number is then given as:



(a)



(b)

Figure 3.6: Comparison of seismicity rates which are calculated for different scenarios of fracture stability. (a) Effect of increasing minimum criticality (more stable fracture system), and (b) effect of decreasing maximum criticality (more unstable fracture system).

$$N_{ev}(t) = \frac{\zeta}{dC} [N_1 + N_2]_{r=a}^{r=b} \quad \text{with :} \quad (3.21)$$

$$N_1 = \frac{q_0}{D} \left( \frac{r^2}{2} - \frac{Dtre^{-\frac{r^2}{4Dt}}}{\sqrt{\pi Dt}} + (Dt - \frac{r^2}{2}) \cdot erf \left( \frac{r}{\sqrt{4Dt}} \right) \right)$$

$$N_2 = \frac{q_t t}{D} \left( \frac{r^2}{2} + \frac{r^4}{16Dt} - \frac{Dtre^{-\frac{r^2}{4Dt}}}{\sqrt{\pi Dt}} \left( \frac{r^2}{4Dt} + \frac{1}{2} \right) + \left( \frac{Dt}{2} - \frac{r^4}{16Dt} - \frac{r^2}{2} \right) \cdot erf \left( \frac{r}{\sqrt{4Dt}} \right) \right)$$

where  $a$  has to be substituted by  $r_{C_{max}}(t)$  and  $b$  by  $r_{C_{min}}(t)$ . For times  $t$  larger than the injection stop time  $t_0$  the cumulative number of microearthquakes can be obtained by the following equation:

$$N_{ev}(t > t_0) = N_{ev}(t) - \frac{\zeta}{dC} [N_1 + N_2 + N_3]_{r=a}^{r=b} \quad \text{with :} \quad (3.22)$$

$$N_1 = \frac{q_0}{D} \left( \frac{r^2}{2} - \frac{D(t-t_0)re^{-\frac{r^2}{4D(t-t_0)}}}{\sqrt{\pi D(t-t_0)}} + (D(t-t_0) - \frac{r^2}{2}) \cdot erf \left( \frac{r}{\sqrt{4D(t-t_0)}} \right) \right)$$

$$N_2 = \frac{q_t t}{D} \left( \frac{r^2}{2} + \frac{r^4}{16D(t-t_0)} - \frac{D(t-t_0)re^{-\frac{r^2}{4D(t-t_0)}}}{\sqrt{\pi D(t-t_0)}} \left( \frac{r^2}{4D(t-t_0)} + \frac{1}{2} \right) \right)$$

$$N_3 = \frac{q_t t}{D} \left( \left( \frac{D(t-t_0)}{2} - \frac{r^4}{16D(t-t_0)} - \frac{r^2}{2} \right) \cdot erf \left( \frac{r}{\sqrt{4D(t-t_0)}} \right) \right)$$

where  $a$  has to be substituted by  $\max\{r_{C_{max}}(t), r_{bf}(t)\}$  and  $b$  by  $r_{C_{min}}(t)$ .

### 3.3 Numerical Verification

Numerical modeling is applied in order to verify the derived analytical solution for pressure diffusion in the case of linearly increasing source strength. For this purpose, the commercial software package COMSOL<sup>®</sup>™ is used to numerically solve the diffusion equation. The outcome of the modeling, that is the spatio-temporal distribution of the pore pressure perturbations, forms the base for the simulation of fluid-induced microearthquakes.

#### 3.3.1 Modeling Approach

A comprehensive description of the modeling approach of fluid-induced seismicity which is used here is given in Rothert (2004). In the following, the procedure of numerical modeling and generation of synthetical microearthquakes is briefly outlined (see also Figure 3.7):

- **Step 1: model creation**

Prior to numerically evaluate injection induced pore pressure perturbations a model set-up has to be defined. For this purpose, I consider a 3D model space with physical dimensions of 3000 *m* in each direction. The hydraulic diffusivity *D* is homogeneously distributed over the whole model space and a value of 0.05 *m*<sup>2</sup>/*s* is assigned to it. In the center of the cube the source is placed which is an injection pressure cavity with a radius *a*<sub>0</sub> of 3 *m*. From the source, fluid injection pressure *p*<sub>I</sub> is liberated satisfying the following initial and boundary conditions:

$$p_I(a_0, t = 0) = 0 \qquad p_I(a_0, t) = p_t t \quad \text{for } t \leq t_0,$$

with pressure gradient  $p_t = 50 \text{ Pa/s}$  and injection stop time  $t_0 = 4 \cdot 10^5 \text{ s}$ . *r* is the radial distance to the source defined as the vector norm  $|\vec{r}| = \sqrt{x^2 + y^2 + z^2}$ . The initial condition for the pore pressure  $p(r, t)$  in the whole model domain is set to:

$$p(r \geq a_0, t = 0) = 0,$$

whereas along the surface of the model space,  $\partial\Omega$ , a Dirichlet boundary condition is defined in such a way that there is fixed zero pore pressure:

$$p(\forall r \in \partial\Omega, t) = 0.$$

- **Step 2: equation solving**

The partial differential equation of time-dependent linear pressure diffusion

is solved using the FE (finite element) method (Gallagher, 1975) which is implemented in COMSOL<sup>®</sup>™. The finite element modeling is done for a total time  $t = 360 h = 1.296 \cdot 10^6 s$ , with a sample interval  $\Delta t = 3600 s$ . As a result, it provides the spatio-temporal evolution and distribution of pore pressure perturbations  $p(x, y, z, t)$  on the nodes of the irregularly spaced element grid. Afterwards, the obtained numerical solution is interpolated to regularly spaced cells which is required for further processing. The 3D model with a length of  $x = y = z = 800 m$  is subdivided into 64 evenly sized cubes where each cube consists of  $50 \times 50 \times 50$  cells. Hence, the total number of cells in the whole model is 8 million.

- **Step 3: criticality field**

Once the perturbed pore pressure field caused by an injection has been obtained synthetical microseismicity can be generated. For this purpose, a failure, respectively microearthquake triggering criterion, has firstly to be introduced. In accordance with the concept of *SBRC*, which argues that the *in-situ* stress state of rocks in the upper Earth crust is close to a critical state of failure equilibrium, a criticality field  $C(\vec{r})$  is defined. In the model, the state of stability of pre-existing defects (such as faults, fractures, fissures) is characterized by assigning a critical value of pore pressure  $C$  to each cell. These critical pressures are statistically homogeneous and randomly distributed on the complete ensemble of cells.

- **Step 4: seismicity triggering**

The triggering of seismicity is now realized by comparing the pore pressure perturbation  $p(r, t)$  and the critical pressure  $C(\vec{r})$  for each cell and for each time step. If at a time  $t = t_e$  the increasing pore pressure exceeds the local criticality value in a point  $\vec{r}_e$  then this point becomes the hypocenter of a microearthquake with source time  $t_e$ :

$$p(\vec{r}_e, t_e) \geq C(\vec{r}_e) \quad \implies \quad event(x_e, y_e, z_e, t_e)$$

Once an event occurred in a certain point no additional microearthquakes are triggered at this position. It concludes from the assumption that recharging of critically stressed defects due to processes such as stress corrosion, tectonical loading and deformation is much slower than the process of pore pressure diffusion (Shapiro et al., 2007). Finally, the obtained synthetical cloud of microearthquakes can further be analyzed, for instance, its spatio-temporal characteristics and the rate of seismicity.

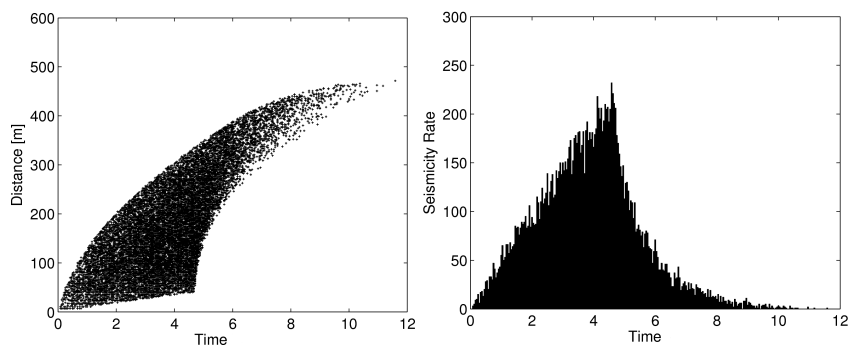
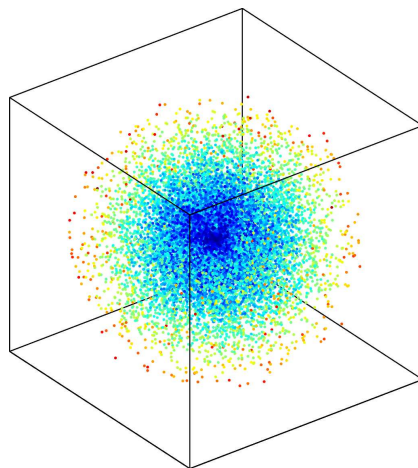
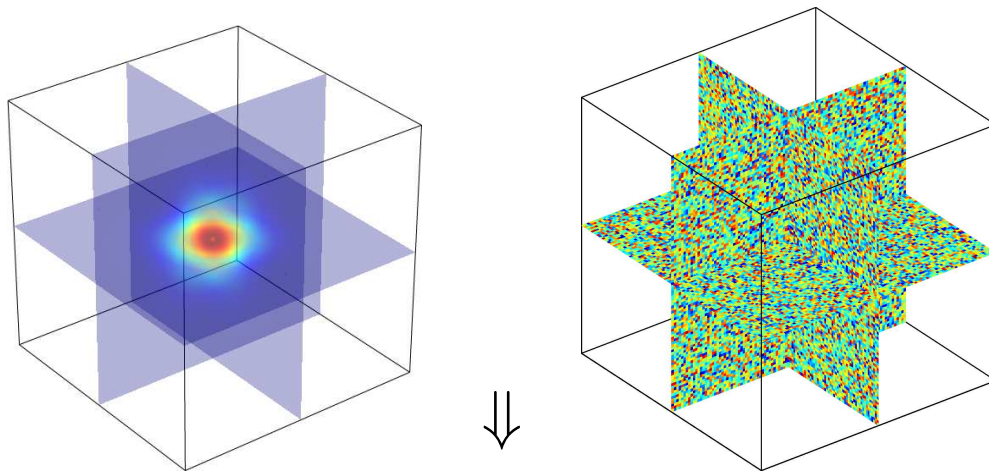


Figure 3.7: (Page 51) Work flow of generating synthetical fluid-induced microearthquakes using numerical modeling. After a model set-up has been defined, the differential equation of linear pressure diffusion is numerically solved with the FE method to obtain the pore pressure perturbation (top left). A criticality field is then defined which statistically characterizes the strength of pre-existing fractures (top right). A comparison of pore pressure perturbation and criticality provides a cloud of microearthquakes (middle) which can be analyzed using a  $r - t$  diagram (bottom left) or its seismicity rate (bottom right)

---

### 3.3.2 Comparison of Modeling Results with the Analytical Solution

In a first step, pore pressure perturbations  $p(r, t)$  that have been obtained from the analytical as well as the numerical solution of the diffusion equation are compared with each other. The parameters for the calculation are the same as used in the FE modeling:

- source terms  $q_0 = 4\pi D a_0 p_0$ ,  $q_t = 4\pi D a_0 p_t$ 
  - constant injection pressure  $p_0 = 0 \text{ Pa}$
  - pressure gradient  $p_t = 50 \text{ Pa/s}$
- effective source radius  $a_0 = 3 \text{ m}$
- injection duration  $t_I \leq t_0 = 4 \cdot 10^5 \text{ s}$
- hydraulic diffusivity  $D = 0.05 \text{ m}^2/\text{s}$

Figure 3.8(a) shows pore pressure profiles as function of distance to the source point for different times. In such a presentation, one can examine the temporal evolution of the spatial distribution of pore pressure perturbations. It is clearly identifiable from the figure that the profile lines well coincide for both solutions. In Figure 3.8(b) the pore pressure perturbation is plotted as function of time for different distances to injection source. Again, one can see a good agreement between analytical and numerical solution although minor deviations are recognizable, in particular for the  $50 \text{ m}$  profile line during the post-injection phase (times  $t > t_0$ ). But, the overall deviations are in the order of the grade of accuracy of the numerical modeling.

In a next step, the modeled pore pressure perturbation is used to generate microearthquakes as explained before. The synthetical microseismicity allows for

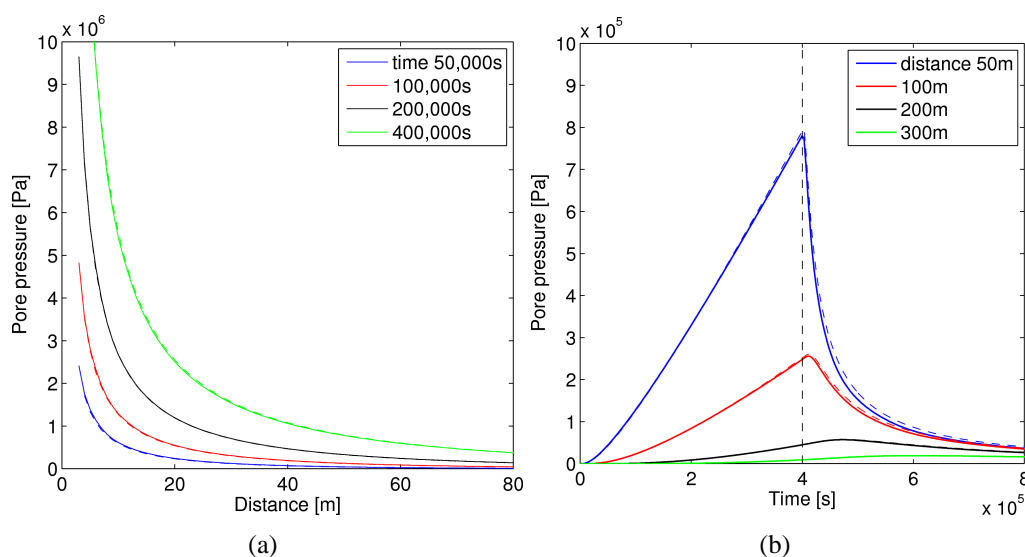
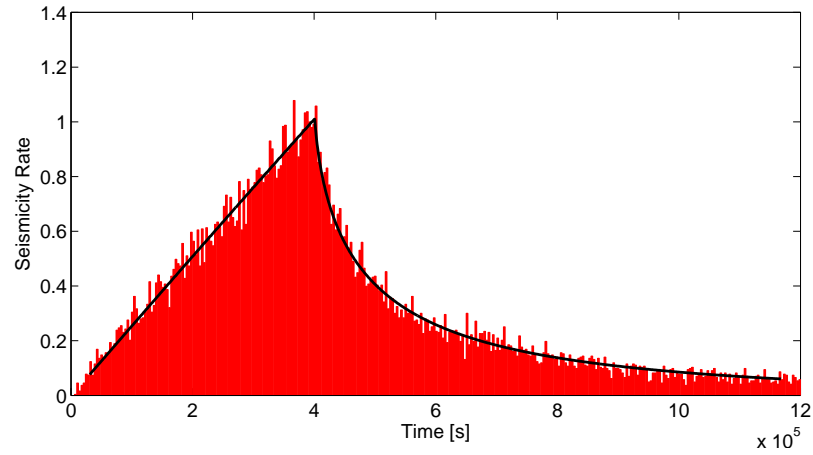


Figure 3.8: (a) Pore pressure profiles from numerically solving the diffusion equation (dashed lines) and from the analytical solution (solid lines) as function of distance to source point. (b) Pore pressure profiles as function of time. Vertical dashed line marks time of injection stop.

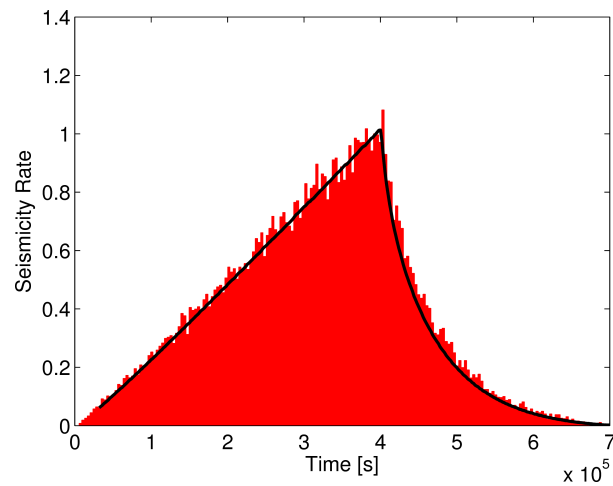
further testing the derived analytical equations. Here the rate of seismicity is considered in more detail. Using Equation (3.14) and Equation (3.16) the seismicity rate is calculated for different scenarios of fracture stability and then compared to an equivalent modeled seismicity rate. The result is presented in Figure 3.9. One can notice from the figure that both analytically and numerically determined seismicity rates well correlate for the shown setups of criticality limits.

### 3.4 Application to Basel Data

In 1996, Geopower Basel AG and its contractor Geothermal Explorers Ltd. started to establish a new geothermal site in Basel, Switzerland, to produce heat and electric energy (Häring et al., 2008). The city of Basel is located at the southern end of the Upper Rhine Graben system where it intersects the fold and thrust belt of the Jura Mountains. The area represents a positive geothermal anomaly in Central Europe with an estimated reservoir temperature of about  $190^\circ\text{C}$  in  $5\text{ km}$  depth (Häring et al., 2008). The geological and tectonical setup of the region is illustrated in Figure 3.10. The Rhine Graben is part of the Cenozoic European Rift system, a failed extensional rift structure extending



(a)



(b)

Figure 3.9: Comparison of seismicity rates for two different set-ups of fracture stability: (a)  $C_{min} = 500 \text{ Pa}$  and  $C_{max} = 1 \text{ MPa}$ , (b)  $C_{min} = 10,000 \text{ Pa}$  and  $C_{max} = 1 \text{ MPa}$ . Red bars represent the seismicity rates obtained by numerical modeling and black lines represent analytically calculated seismicity rates according to Equation (3.14) and Equation (3.16).

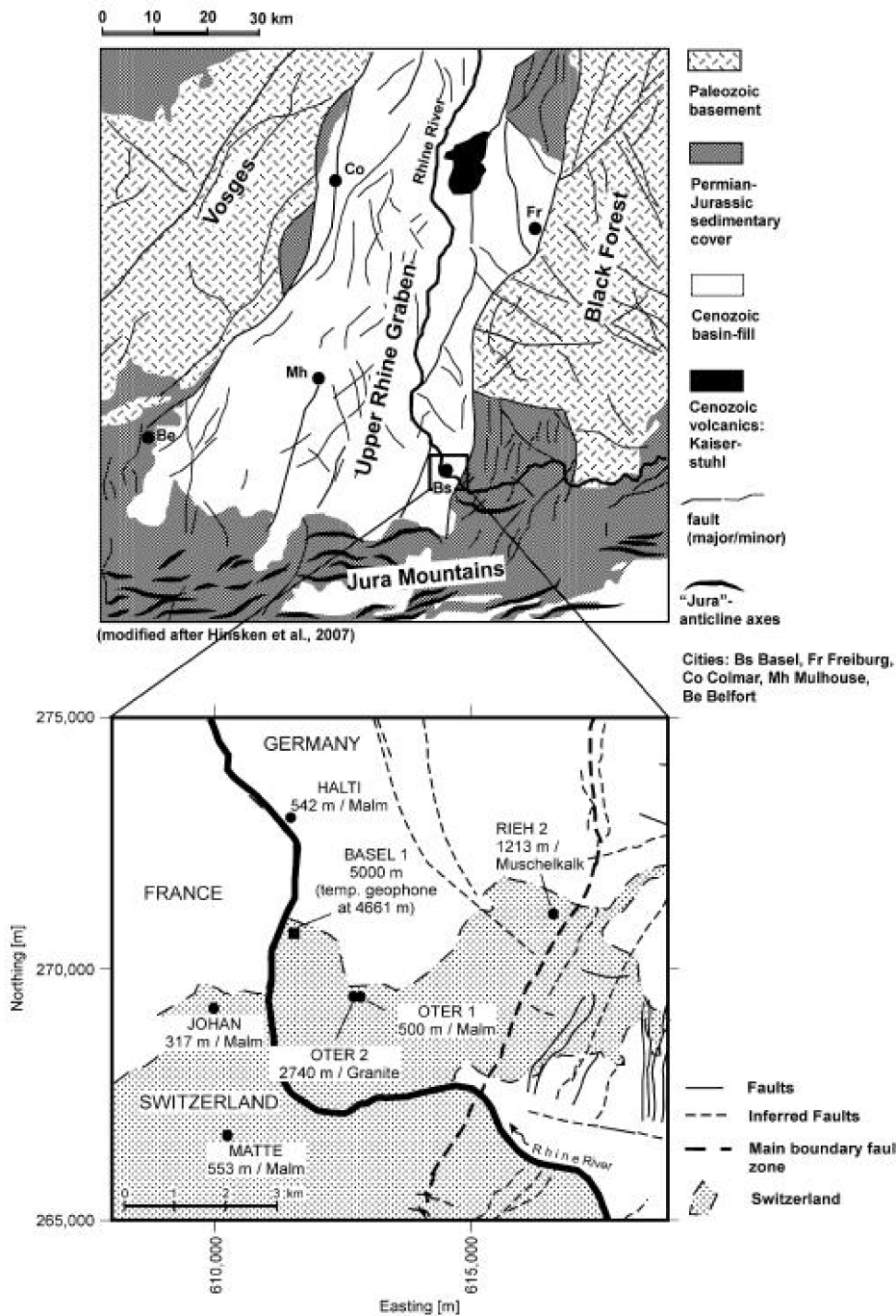


Figure 3.10: Schematic geological and tectonical map of the southern Upper Rhine Graben. Lower part shows the seismic monitoring network: black circles mark the positions of seismic stations. In addition, information on installation depth and geological formation are given for each station (after Häring et al., 2008).

from Norway (Oslo Graben) to the Mediterranean Sea in south of France (Rhône Graben) (Eisbacher, 1996). As a consequence of its tectonic evolution, the Upper Rhine Graben forms a weakness zone which is documented by significant natural seismic activity (Deichmann and Giardini, 2009). It is noteworthy in this context that the strongest historically known earthquake in Europe north of the Alps occurred in Basel in 1356. The dominant mechanism of recent natural seismicity in the area is controlled by the Alpine compression (Dyer et al., 2008) resulting from large-scale collision between the African and the European continental plates.

After completion of drilling borehole Basel-1 into the granitic basement, a hydraulic stimulation to enhance the permeability of the reservoir was performed in December 2006. Within six days of fluid injection, about  $11,500 \text{ m}^3$  water were pumped at stepwise increased flow rates up to  $60 \text{ l/s}$  and maximum wellhead pressures of  $\sim 30 \text{ MPa}$  (Figure 3.11). The installed seismic monitoring system consists of six permanent and one temporary 3-component downhole geophones (Figure 3.10). After its automatic detection the hypocenter location of a microearthquake was determined by a grid-search algorithm using P and S wave traveltimes and a 1D velocity model. A detailed description of data acquisition, processing and event localization is given in Dyer et al. (2008).

During the period of injection, approximately 14,000 microearthquakes were detected by the monitoring system from which about 2300 have been located in near real-time. The hypocenter distribution of the microearthquakes is shown in Figure 3.12. The event cloud forms an elongated zone of seismic activity striking  $N160^\circ E$ . This dominant orientation is sub-parallel to the direction of maximal horizontal stress  $S_{Hmax}$  which was estimated from borehole breakouts and from drilling induced tensile fractures (Dyer et al., 2008). It clearly demonstrates a preferred direction of fluid migration in the direction of maximum horizontal stress. It means that fluid transport properties are expected to be anisotropically distributed in the reservoir. The dimension of the microseismic cloud is approximately  $850 \text{ m}$  in strike direction,  $250 \text{ m}$  perpendicular to the direction of strike, and  $1000 \text{ m}$  in vertical direction. An interesting feature of the induced seismicity can be identified from the depth distribution of hypocenters. Considering the temporal evolution of the event cloud one can see that although it was intended to pressurize the complete open hole section (OHS,  $4378 \text{ m} - 4749 \text{ m}$ ) the injected fluid entered the reservoir rock only in the upper part of the OHS (Figure 3.12). Dyer et al. (2008) reported that the temporally installed geophone got stuck in  $4422 \text{ m}$  depth prior to the stimulation. However, well logging during water injection revealed that the open hole section was not hydraulically locked. Therefore a zone of higher permeability at this depth range can be concluded. It is confirmed

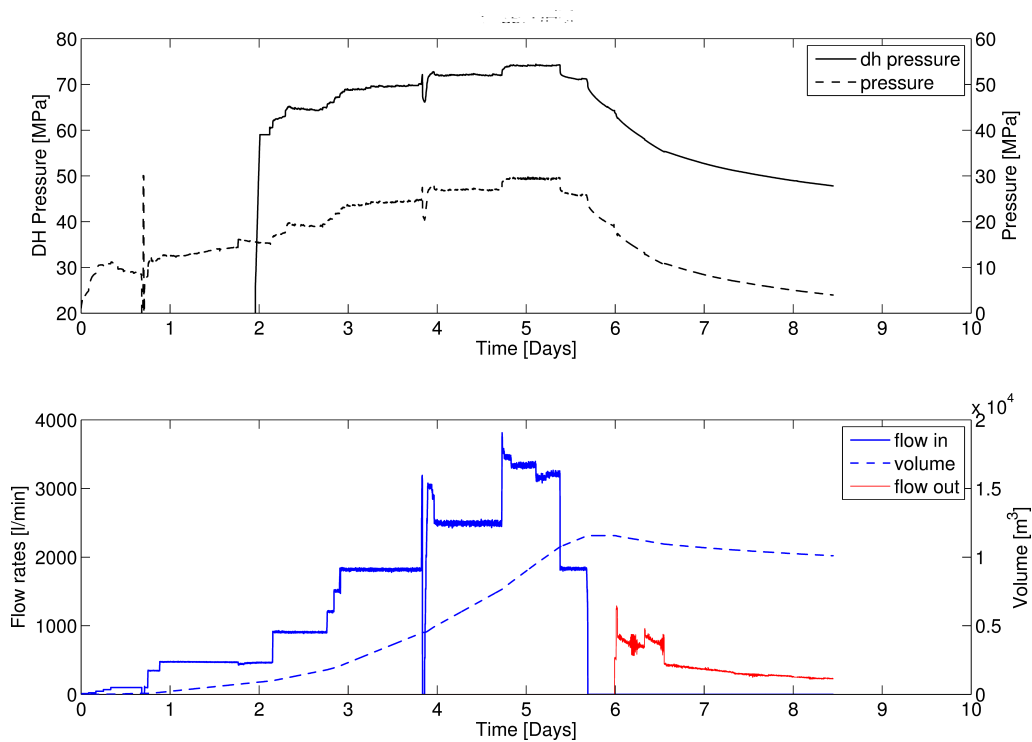


Figure 3.11: Hydraulic treatment data of the Basel geothermal reservoir stimulation in 12/2006. The upper part of the figure shows injection pressure (dashed line) and downhole pressure (solid line). The lower part shows flow rate (solid blue line) and cumulative injected volume (dashed blue line). Red line represents fluid out-flow of the borehole Basel-1 which was opened after an event with local magnitude  $M_L = 3.4$  occurred. The reason for opening the borehole was to avoid further microearthquakes with a significant magnitude by decreasing the overpressure in the reservoir.

by acoustic borehole imaging which has shown that the fracture density decreases with depth, from 0.3 to 0.2 per meter, as well as the presence of a major cataclastic zone at 4450 m (Häring et al., 2008).

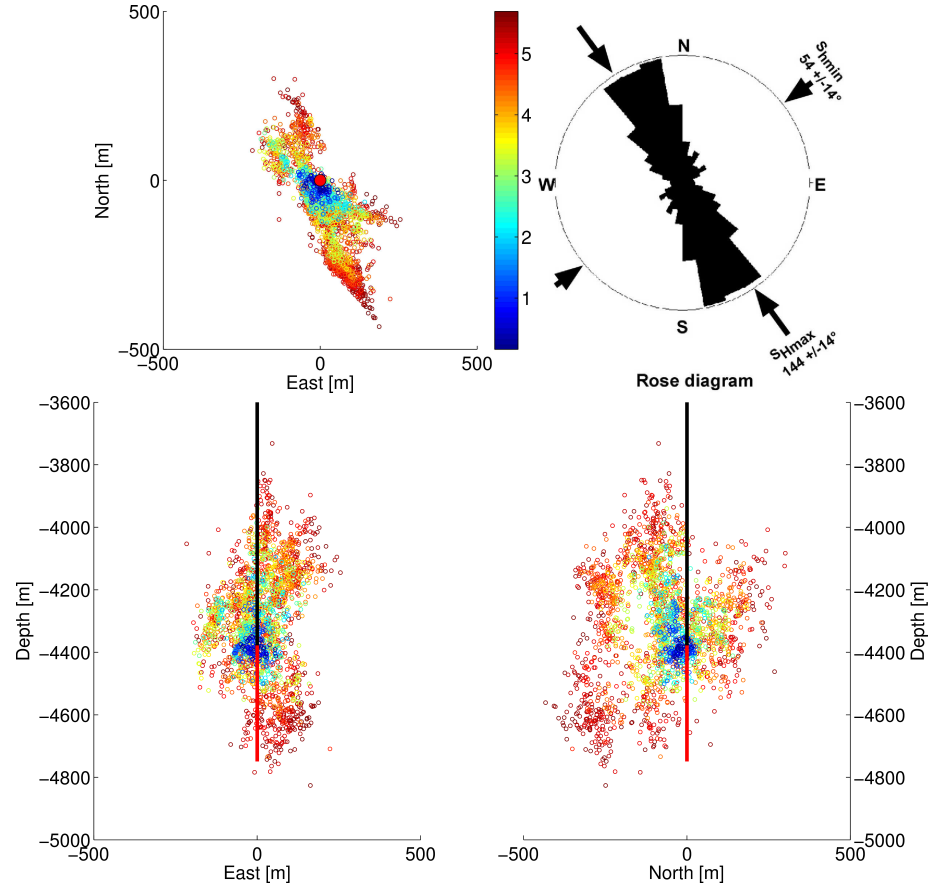


Figure 3.12: Source locations of microearthquakes induced during the injection period (02.12.-08.12.2006). Color corresponds to event occurrence time (in days), the red point in map view marks well location, black and red line in depth views mark trajectory of injection well and open hole section, respectively. Upper right plot shows the rose diagram of fracture orientation which indicates the direction of maximum horizontal stress  $S_{Hmax}$  (after Häring et al., 2008).

### 3.4.1 Heuristic Analysis

At first, it is intended to apply the concept of triggering fronts as described in Chapter 2.2 to the Basel microseismic data. In such a way, one gets an idea

about the magnitude of hydraulic properties of the reservoir. Moreover, the estimate of the tensor of hydraulic diffusivity is later needed for transferring the microearthquakes from an anisotropic medium to an effectively isotropic medium. This transfer is necessary since an isotropic distribution of hydraulic diffusivity is assumed in the derived equations for a deterministic analysis.

### **Diffusivity estimate from isotropic approximation**

Although one notices from the alignment of induced microearthquakes that hydraulic properties of the reservoir are anisotropic, a scalar diffusivity is firstly derived using the spatio-temporal evolution of microseismicity. For this purpose, the induced microearthquakes are presented in a  $r - t$  diagram, that is a plot of minimum distance between injection source and hypocenter location of each microearthquake as function of its occurrence time (Figure 3.13(a)). Also shown in Figure 3.13(a) are the triggering front curve and the back front curve which have been fitted to the data points according to Equation (2.4) and Equation (2.23), respectively. Both envelopes of the seismic cloud yield a hydraulic diffusivity  $D = 0.06 \text{ m}^2/\text{s}$  as the most representative estimation.

Another possibility to estimate the hydraulic diffusivity provides an analysis of event density in a  $r - t$  grid (Figure 3.13(b)). The number of microearthquakes is counted in each grid cell whose dimensions are  $1.3h \times 13m$ . Triggering front and back front curves are then fitted in such a way that they limit the region with high event density. This procedure yields the following result. As in the case of a regular  $r - t$  diagram, one value for the hydraulic diffusivity can be derived from both enveloping curves. A hydraulic diffusivity of the order of  $0.05 \text{ m}^2/\text{s}$  is obtained by investigating the event density in a  $r - t$  grid.

### **Diffusivity estimate from anisotropic approximation**

In the next step, the real situation of heterogeneously distributed diffusivity is approximated by an anisotropic but homogeneous medium. For such a situation, the triggering front of seismicity is given by Equation (2.6). Diagonalization of the diffusivity tensor in this equation results in an ellipsoidal equation in which the source coordinates of microearthquakes are scaled by the square root of their occurrence times (see Equation 2.8). The half-axes of the ellipsoid are equal to the square roots of components of the diffusivity tensor in principle coordinate system,  $D_{11}$ ,  $D_{22}$  and  $D_{33}$ .

An ellipsoidal envelope to the scaled microseismic cloud is now determined by applying the algorithm which has been proposed by Rindschwentner (2001). Microearthquakes which occurred in the period of strongly reduced flow rates prior

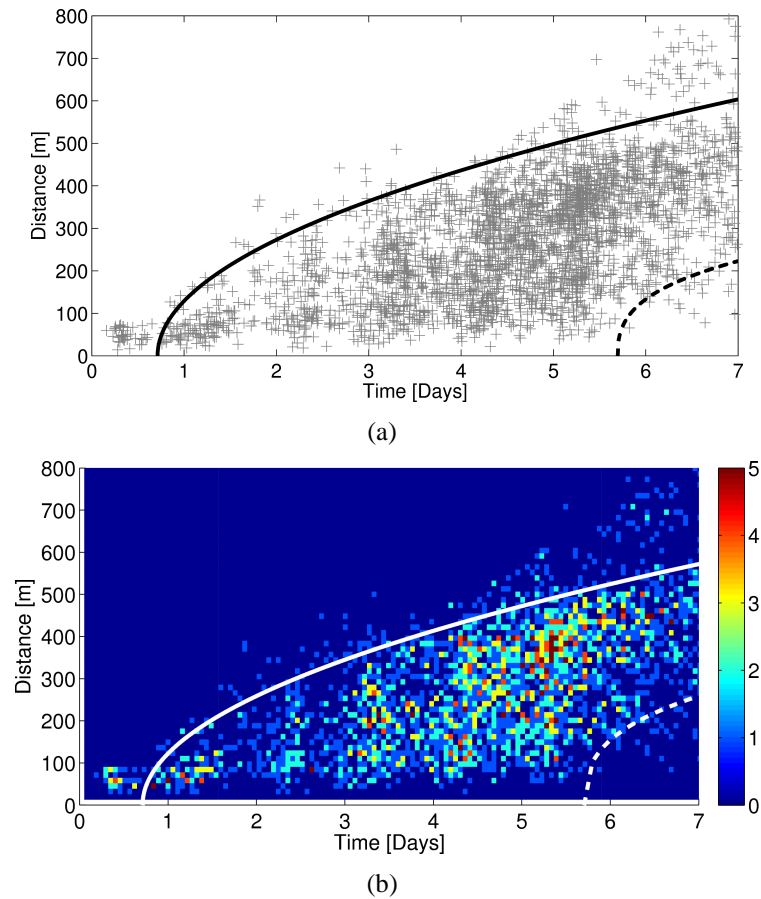


Figure 3.13: (a)  $r-t$  diagram of induced microearthquakes and (b) event density in a  $r-t$  grid. In (a) and (b) triggering and back front curves are plotted. The onset of triggering front curve is shifted to account for the low flow rate in the beginning of injection (compare with Figure 3.11).

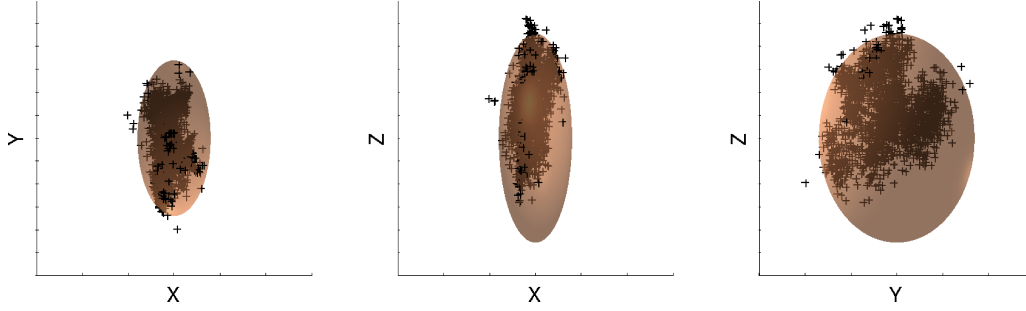


Figure 3.14: Cloud of induced microearthquakes in principal coordinate system ( $X, Y, Z$ ) together with fitting ellipsoid with its half-axes representing the tensor of hydraulic diffusivity.  $X, Y$ , and  $Z$  axis are equally scaled. Center of ellipsoid is distinct fluid entry point at  $4422\text{ m}$  depth.

to the injection stop (see Figures 3.11) are treated as post-injection events and are therefore not processed. The ellipsoid shown in Figure 3.14 is obtained as best fit to the data. In source location coordinate system, the ellipsoid is defined by a strike direction of  $150^\circ$  and a dip angle of  $89^\circ$ . The strike angle is close to the direction of  $S_{Hmax}$ , but the longest half-axis of the ellipsoid is in the vertical plane. It is coherent since the magnitude of vertical stress  $S_V$  is lower than the magnitude of maximum horizontal stress  $S_{Hmax}$  (see Häring et al., 2008). It can be concluded that pre-existing fractures are likely vertically oriented and aligned with the direction of  $S_{Hmax}$ . The half-axes of the ellipsoid yield the hydraulic diffusivity tensor:

$$\mathbf{D} = \begin{pmatrix} 0.6 & 0 & 0 \\ 0 & 2.9 & 0 \\ 0 & 0 & 5.2 \end{pmatrix} \cdot 10^{-2} \frac{m^2}{s}$$

One can also notice from Figure 3.14 an asymmetry of the microseismic cloud in the vertical plane with respect to the injection point. It means that the center of the cloud is shifted upwards and therefore being above the fluid entry zone. The lower number of microearthquakes with increasing depth (compared to the opposite direction) is caused by higher vertical stresses  $S_V$  which acts against the pore pressure perturbation. Despite this observation, I conclude that the estimated diffusivity tensor is reasonable and it is in accordance with the estimate from the isotropic approximation.

### 3.4.2 Deterministic Analysis

In the following, I will utilize the derived equations for pore pressure perturbation, seismicity rate and cumulative number of microearthquakes (introduced in Chapter 3.2) for a reservoir characterization.

#### Spatial event density

The first method that is applied to the Basel data considers the spatial density distribution of induced microearthquakes. The method was proposed by Shapiro et al. (2005), and it is based on the statistical model of fluid-induced microseismicity. We have seen in the introduction of this chapter that the event probability is directly proportional to the pore pressure perturbation,  $P(Ev, r, t) \propto p(r, t)$ , in case this perturbation is non-decreasing. It means that a comparison of the injection-induced pore pressure perturbation given by Equation (3.9) with the observed spatial event density allows for estimating the hydraulic diffusivity.

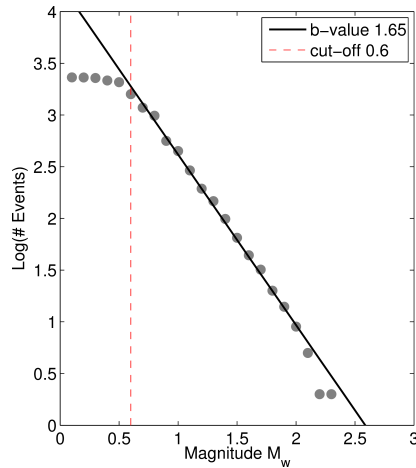


Figure 3.15: Frequency-magnitude distribution of induced microearthquakes. The distribution is used to define the magnitude of completeness,  $M_c$ , which is 0.6 for the Basel catalog (marked by the dashed line).

The event density is determined by applying the following procedure to the located microearthquakes. Since isotropic reservoir conditions are considered, the microseismic data have to be preprocessed to correct for the observed anisotropy. The source coordinates of microearthquakes are rotated and scaled to transfer the microseismic cloud from hydraulically anisotropic conditions into an equivalent cloud in an effectively isotropic medium (see Shapiro et al., 2003). The rotation matrix and the scaling factors, which are the inverse square roots of the principal components of the diffusivity tensor, have been determined as described in Chapter 3.4.1. In addition, only microearthquakes are considered that have a magnitude above the magnitude of completeness. Thus, the incompleteness of the earthquake catalog due to the magnitude-distance detection threshold is taken into account. The threshold value is derived from the frequency-magnitude distribution of in-

duced microearthquakes. For the Basel injection, such a distribution provides a completeness magnitude  $M_c = 0.6$  (Figure 3.15). After preprocessing the data, the event density can be calculated. Microearthquakes are counted in concentric spherical shells centred at the injection point (Figure 3.16). The radius increment is kept constant in this routine. Therefore the total event number in each shell has to be scaled by the shell volume. The resulting scaled numbers are then normalized to the maximum value.

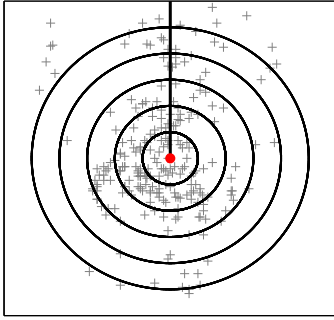


Figure 3.16: Sketch to illustrate the procedure of spatial event density: (I) counting microearthquakes (grey crosses) in spherical shells (black circles) centered at the injection point (red point), (II) scaling event numbers by shell volumes and (III) normalizing to maximal scaled number.

In the next step, the pore pressure perturbation  $p(r, t)$  is calculated according to Equation (3.9) with following parameters for the source term  $q = q_0 + q_t t_I$ :

- source terms  $q_0 = 4\pi D a_0 p_0$  and  $q_t = 4\pi D a_0 p_t$ 
  - constant injection pressure  $p_0 = 11.5 \text{ MPa}$
  - pressure gradient  $p_t = 48 \text{ Pa/s}$
  - $p_0$  and  $p_t$  are derived by linear regression of the measured injection pressure (Figure 3.17)
- effective source radius  $a_0 = 2.38 \text{ m}$ 
  - spherical surface equivalent of a cylindrical surface which is an open hole section with length  $h \sim 45 \text{ m}$  (main zone of fluid entry, see Figure 3.18)
- injection time  $t_I = 4 \cdot 10^5 \text{ s}$ 
  - time interval of significant and non-decreasing flow rates (Figure 3.17)

The hydraulic diffusivity  $D$  in Equation (3.9) is then varied to correlate the normalized pore pressure perturbation with the observed normalized spatial event density. The result is shown in Figure 3.19. Depending on the selected shell radius, best possible matches are obtained with hydraulic diffusivity ranging from  $D = 0.055 \text{ m}^2/\text{s}$  to  $D = 0.07 \text{ m}^2/\text{s}$ .

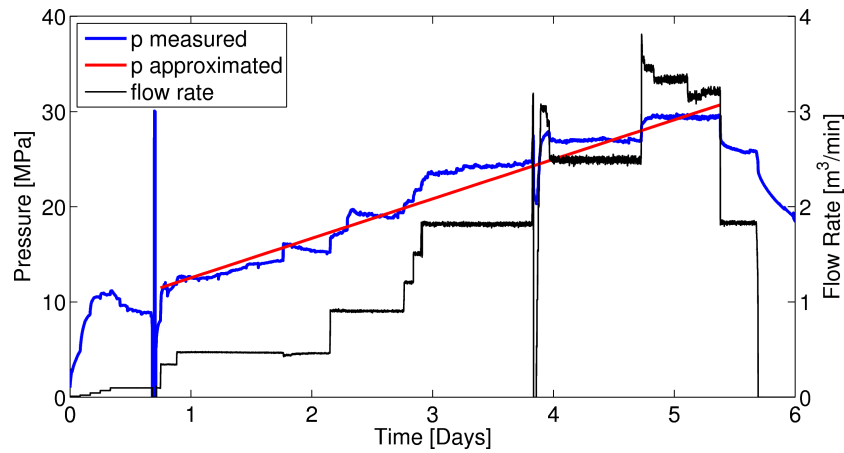


Figure 3.17: Flow rates and injection pressures of the Basel reservoir stimulation performed in 12/2006. The red line represents approximated linear rising pressure function with  $p_0 = 11.5 \text{ MPa}$  and  $p_t = 48 \text{ Pa/s}$  (obtained by linear regression). Begin and end of red line mark the time interval which is considered in our analysis. It covers the period of significant and non-decreasing flow rates.

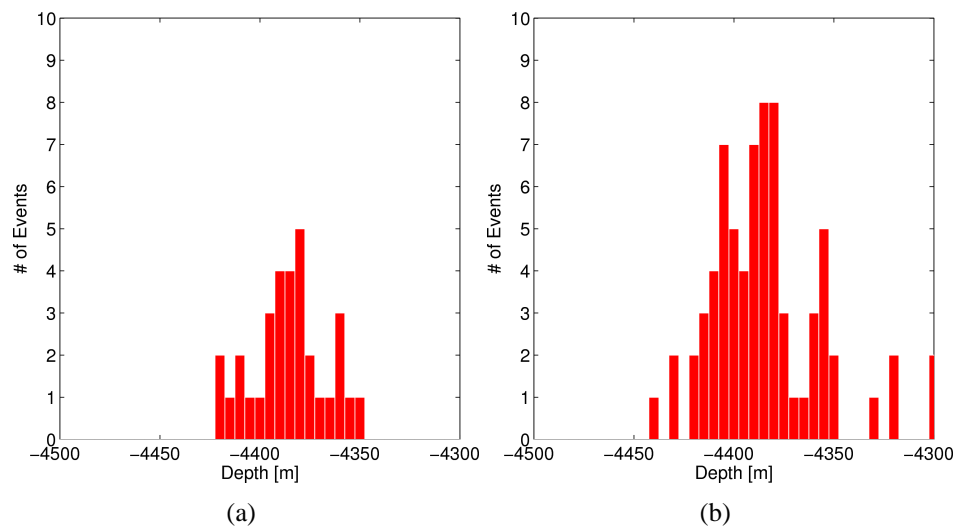


Figure 3.18: Histogram of depth distribution of induced microearthquakes, (a) during the first half day and (b) during the first day of injection. The histograms demonstrate that significant microseismic activity is not occurring below 4425 m in the considered time intervals. Since the open hole section of Basel-1 starts at a depth of 4379 m, it means that main zone of fluid entry covers approximately the first 46 m of the complete open hole section.

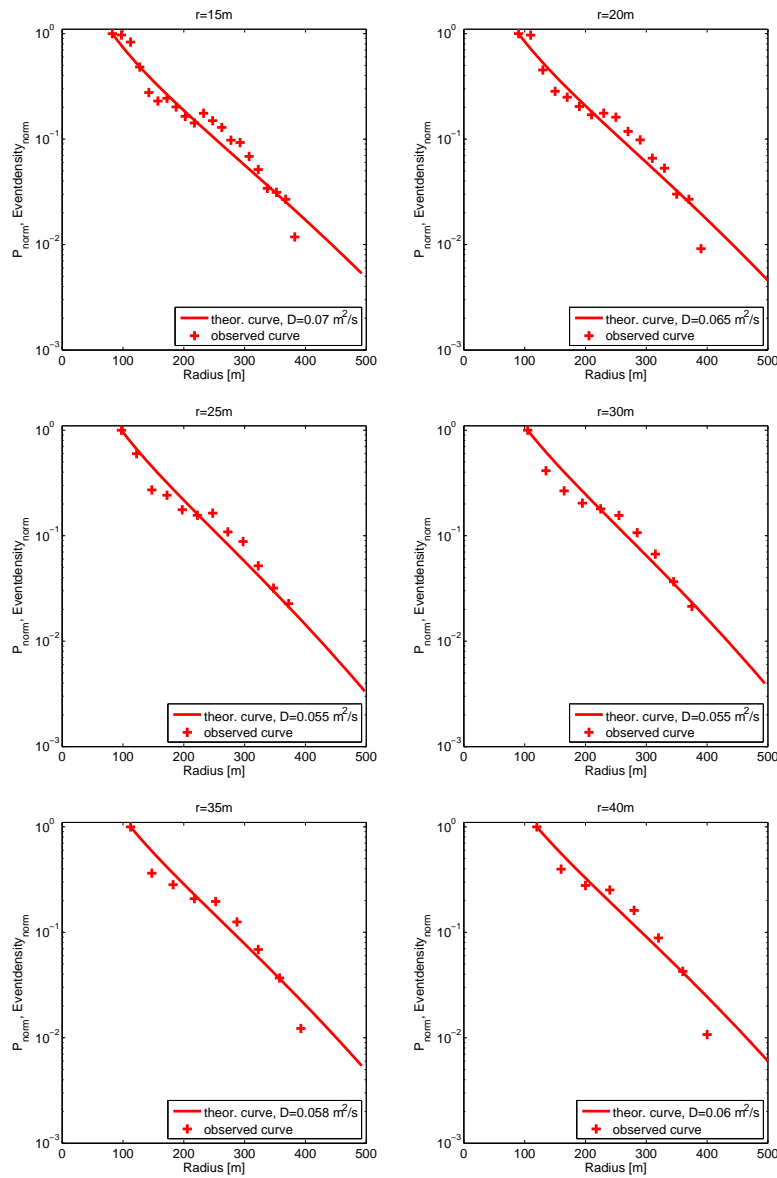


Figure 3.19: Observed spatial event density as function of distance to injection point. Event densities are calculated for varying shell radii ranging from 15 m (top left) to 40 m (bottom right). Theoretical curves represent normalized pore pressure perturbations according to Equation (3.9).

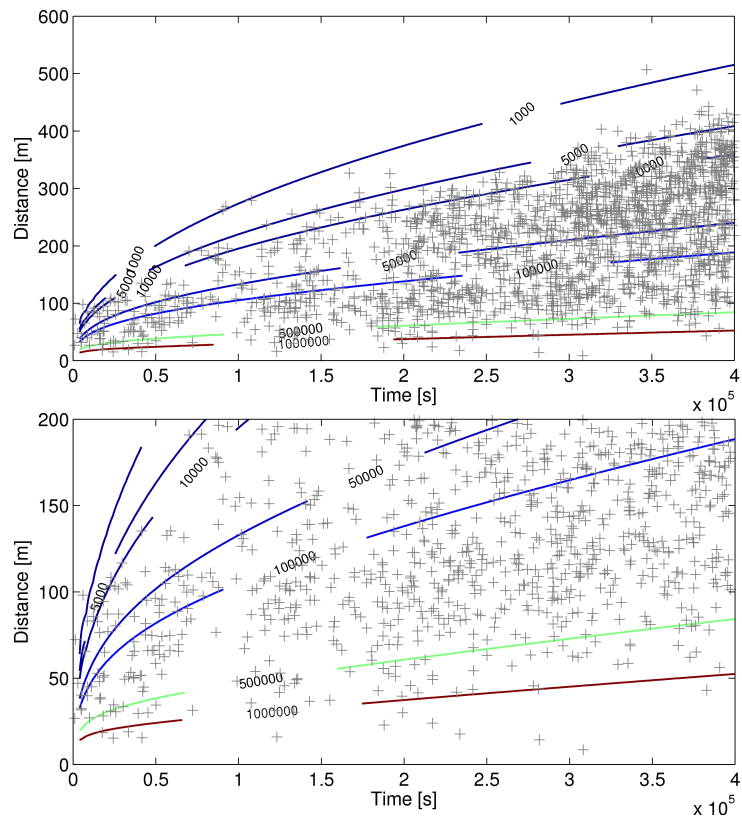


Figure 3.20:  $r - t$  diagram of rotated and scaled microearthquakes induced during the time interval under consideration along with isolines of pore pressure perturbation. The pore pressure perturbation  $p(r, t)$  is calculated using a hydraulic diffusivity  $D = 0.055 \text{ m}^2/\text{s}$ .

Figure 3.20 shows the rotated and scaled cloud of induced microearthquakes in the space - time domain. In addition, isolines of the induced pore pressure perturbations  $p(r, t)$  are presented. The combined presentation allows for quantifying a lower bound and an upper bound of critical pore pressures,  $C_{min}$  and  $C_{max}$ . The critical pore pressure  $C(r)$  defines the value of pore pressure perturbation that must be exceeded in a given point  $r$  of the medium to trigger a microearthquake at exactly this position. Pressure perturbations below the threshold value  $C_{min}$  are not sufficient to induce microseismic events. The isosurface (respectively isoline) of pore pressure perturbation with the value of maximum criticality corresponds to the distance below which all possible fractures have already ruptured. In other words, the whole medium is brought to failure if  $p(r, t)$  equals  $C_{max}$  and no further microearthquakes can be triggered. The  $r - t$  diagram shows that during injection the upper envelope of microseismicity roughly coincides with the isoline of pore pressure perturbation  $p(r, t) = 5000 Pa$  (Figure 3.20). Furthermore, a region of seismic inactivity below the isoline  $p(r, t) = 1 MPa$  can be identified. Both bounding isolines hence provide estimates of controlling parameters of the seismically active volume during the injection, that are  $C_{min} \sim 5000 Pa$  and  $C_{max} \sim 1 MPa$ . However, one should note that the obtained result can be biased by location uncertainties and by magnitude-distance detection threshold.

### Seismicity rate and cumulative event number

In contrast to the spatial event density, which can only be determined for localized events, the catalog of detected microearthquakes will be considered for an analysis of seismicity rate and cumulative event number. Figure 3.21 shows observed and calculated seismicity rates. Both rates are normalized to the time moment where flow rates have been significantly reduced, that is  $t = t_0 = 400,000 s$ . The bars represent number of detected microearthquakes per one hour. The black curve is calculated according to Equation (3.14) and Equation (3.16). The hydraulic diffusivity and the criticality limits are chosen to match the observed seismicity rate and to be in agreement with before estimated values. The best possible fit results in a hydraulic diffusivity  $D = 0.065 m^2/s$ . Minimum and maximum criticality are  $C_{min} = 6000 Pa$  and  $C_{max} = 0.75 MPa$ , respectively.

However, one can notice deviations between both experimental and analytical seismicity rate, in particular during the first half of injection. If the fluid flow rate is additionally shown in this figure, then an interesting characteristic can be observed. The triggering of induced seismicity reacts very sensitive to the applied injection flow rates. Moreover, the two rates run nearly parallel if both are normalized to time  $t = 400,000 s$ . The cumulative number of microearthquakes along with the injected fluid volume show a similar behavior (Figure 3.22).

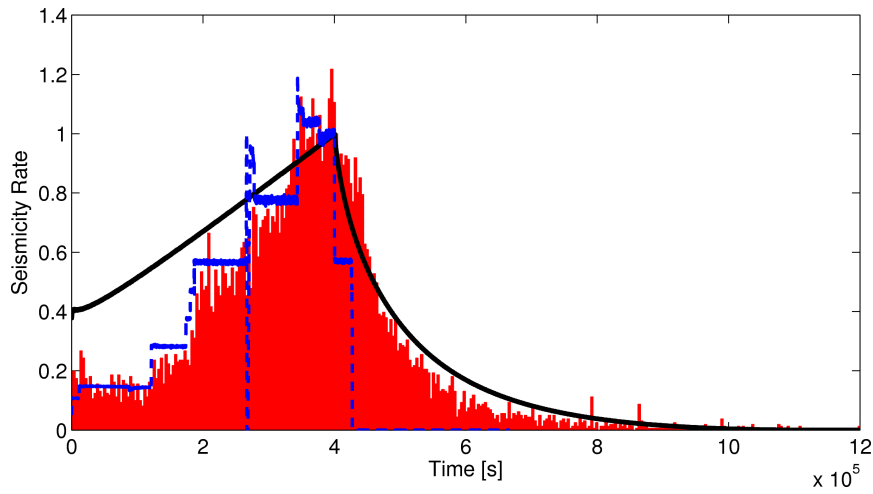


Figure 3.21: Seismicity rate of induced microearthquakes normalized by its value at time  $t_0 = 400,000$  s. Red bars mark number of detected events per hour and black line denotes analytical seismicity rate. The analytical rate is calculated according to Equation (3.14) and Equation (3.16) with criticality parameters  $C_{max} = 0.75$  MPa and  $C_{min} = 6000$  Pa, and with a hydraulic diffusivity  $D = 0.065$  m<sup>2</sup>/s. Dashed blue line denotes injection flow rate.

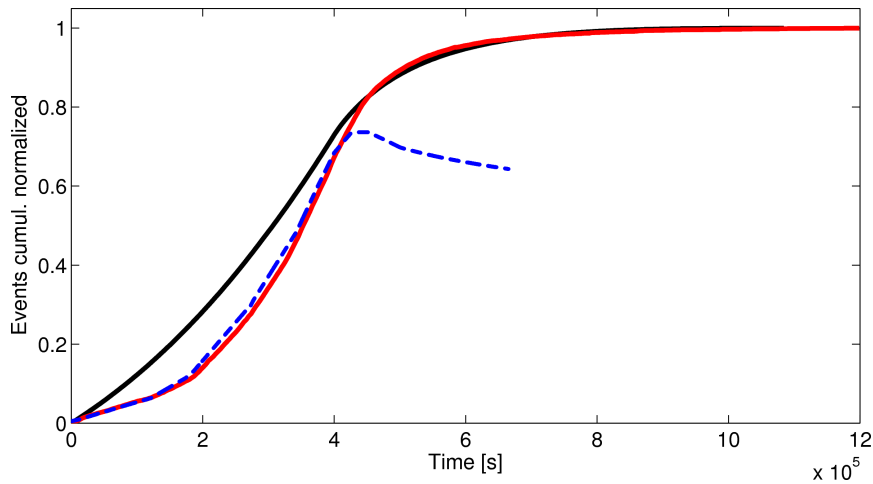


Figure 3.22: Normalized cumulative number of microearthquakes. Red line marks the observed cumulative number, black line denotes analytical cumulative number which is calculated according to Equation (3.21) and Equation (3.22) with parameters as given in the caption of Figure 3.21. Dashed blue line denotes cumulative volume of injected fluid.

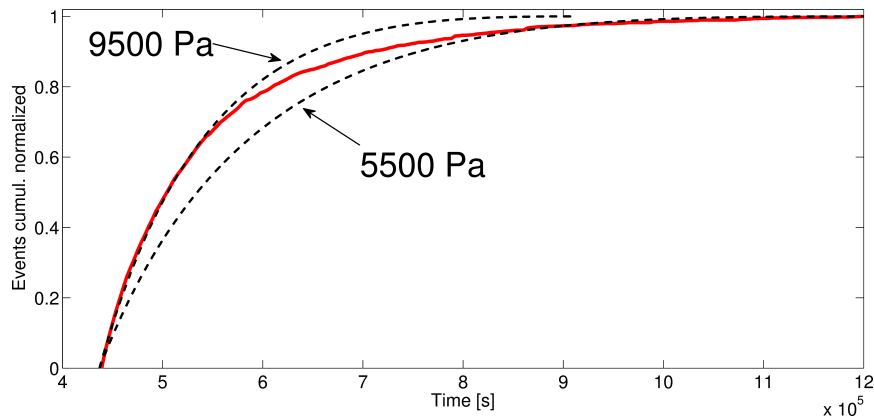


Figure 3.23: Normalized cumulative number of microearthquakes induced after shut-in. Red line marks the observed cumulative number, dashed black lines denote analytical cumulative numbers which are calculated according to Equation (3.22). To achieve good correlation between theoretical curve and observed curve, one has to consider an interval of minimum criticality,  $C_{min}$ , ranging from 9500  $Pa$  to 5500  $Pa$ .

Nevertheless, Figure 3.21 and Figure 3.22 demonstrate that prediction and observation well coincide in the post-injection phase. Therefore the cumulative number of microearthquakes induced after the injection stop is considered for a characterization of reservoir parameters (Note that the shut-in time is at about 430,000  $s$ , compare with Figure 3.17). The decay characteristic of detected microearthquakes requires special data matching, such that the best possible fit provides not only one definite value for the minimum criticality but rather an interval from  $5500 < C_{min} < 9500 Pa$  (Figure 3.23). Precisely, it means that shortly after the shut-in of injection a good correlation is achieved using a diffusivity  $D = 0.055 m^2/s$  and minimum criticality  $C_{min} = 9500 Pa$  for the calculation of the cumulative number whereas with ongoing time  $C_{min}$  decreases to 5500  $Pa$ . Probably, the observed special behavior of seismicity decay is caused by two different sets of pre-existing fractures as reported by Dyer et al. (2008) and as it can also be identified from the hypocenter distribution (map view in Figure 3.12). The two fracture systems are assumed to be statistically represented by individual ensembles of uniformly distributed criticality. Depending on their alignment with respect to the direction of maximum horizontal stress, the two fracture systems can likely be characterized by different values for minimum criticality. However, also unimodal- or Weibull-distributed critical pore pressures can lead to the observed phenomenon of induced seismicity in Basel. Later in this chapter, it will be investigated whether numerical modeling provides an explanation.

### 3.4.3 Numerical Verification of Results

The idea is to validate the obtained estimates for the hydraulic diffusivity and the criticality limits on the basis of finite element (FE) modeling and synthetically generated microseismicity. The individual steps of the modeling approach have been already described in Chapter 3.3.1. The here presented models differ with respect to the source function that has been applied in the numerical modeling. Further parameters such as model dimensions, observation time and hydraulic diffusivity ( $D = 0.055 \text{ m}^2/\text{s}$ ) are the same in all models.

- Model 1: pressure gradient I

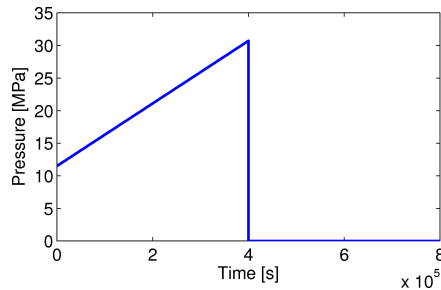


Figure 3.24: Source function applied in Model 1:

- $p_0 = 11.5 \text{ MPa}$
- $p_t = 48 \text{ Pa/s}$
- $t_I = 400,000 \text{ s}$

- Model 2: pressure gradient II

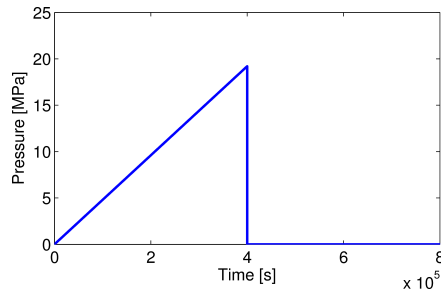


Figure 3.25: Source function applied in Model 2

- $p_0 = 0 \text{ MPa}$
- $p_t = 50 \text{ Pa/s}$
- $t_I = 400,000 \text{ s}$

- Model 3: Basel pressure

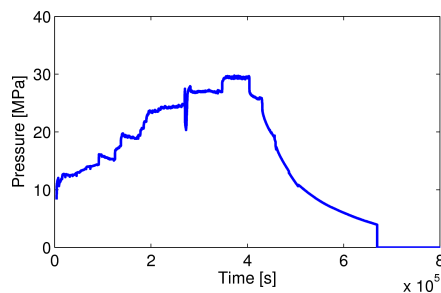


Figure 3.26: Source function applied in Model 3

- measured wellhead (injection) pressures
- $t_I = 430,000 \text{ s}$

A cloud of microearthquakes is generated for each of the presented models using criticality limits, that are  $C_{min}$  and  $C_{max}$ , which provide best possible correlation with characteristics of detected microearthquakes in Basel. In Chapter 3.2.3, it

Model	Source Function	Criticality		Tectonic potential $F_t$	Events
		$C_{min}$	$C_{max}$		
1	pressure gradient I	9600 Pa	0.15 MPa	$0.61 \cdot 10^9 J$	18,948
2	pressure gradient II	9500 Pa	0.08 MPa	$0.33 \cdot 10^9 J$	13,920
3	injection pressure	$10^4 Pa$	0.08 MPa	$0.33 \cdot 10^9 J$	17,890
4	fluid mass flow	9000 Pa	0.09 MPa	$0.37 \cdot 10^9 J$	13,621

Table 3.1: Set-up (source function and criticality range) and resulting event number of different realizations of the modeling. For a comparison, 13,494 events were detected in Basel in the same time interval. Criticality values in Model 4 are rescaled (see text). The tectonic potential is given as the ratio of maximum criticality and fracture volume concentration,  $F_t = \frac{C_{max}}{\zeta}$ . The fracture volume concentration in all models is  $\zeta = 2.44 \cdot 10^{-4} \frac{1}{m^3}$ .

was demonstrated that the two limits have a dissimilar influence on the microseismicity. The minimum criticality strongly affects the decay characteristic of seismicity after injection stop whereas the number of induced microearthquakes is mainly controlled by the value of maximum criticality and by the volume concentration of pre-existing fractures. Table 3.1 summarizes the corresponding values that have been used to obtain synthetical clouds of microseismicity.

The modeled seismicity rates are evaluated and compared to the detected rate in Basel. One can notice from Figure 3.27 that in all models the maximum of seismicity rate and its decay after injection stop well agree with the observations from Basel (Figure 3.30). It means that criticality limits are properly defined and they are also consistent with the result from the deterministic analysis. It is important to say that the value of maximum criticality, which has been used to generate synthetical microearthquakes, depends on the volume concentration of fractures (that is number of cells in the model space divided by the volume of the model space).  $C_{max}$  is therefore not directly comparable with the estimate provided by the analytical solution. The more sensitive parameter for a comparison is the tectonic potential which was introduced as the ratio of maximum criticality and fracture volume concentration,  $F_t = \frac{C_{max}}{\zeta}$  (Shapiro et al., 2007). Assuming that the measured fracture density can roughly be extrapolated to a fracture volume concentration results in  $\zeta_{Basel} = (0.2 \frac{1}{m})^3 = 8 \cdot 10^{-3} \frac{1}{m^3}$ . The tectonic potential then is  $0.13 \cdot 10^9 J$  if  $C_{max}$  is of the order of 1 MPa. Since the

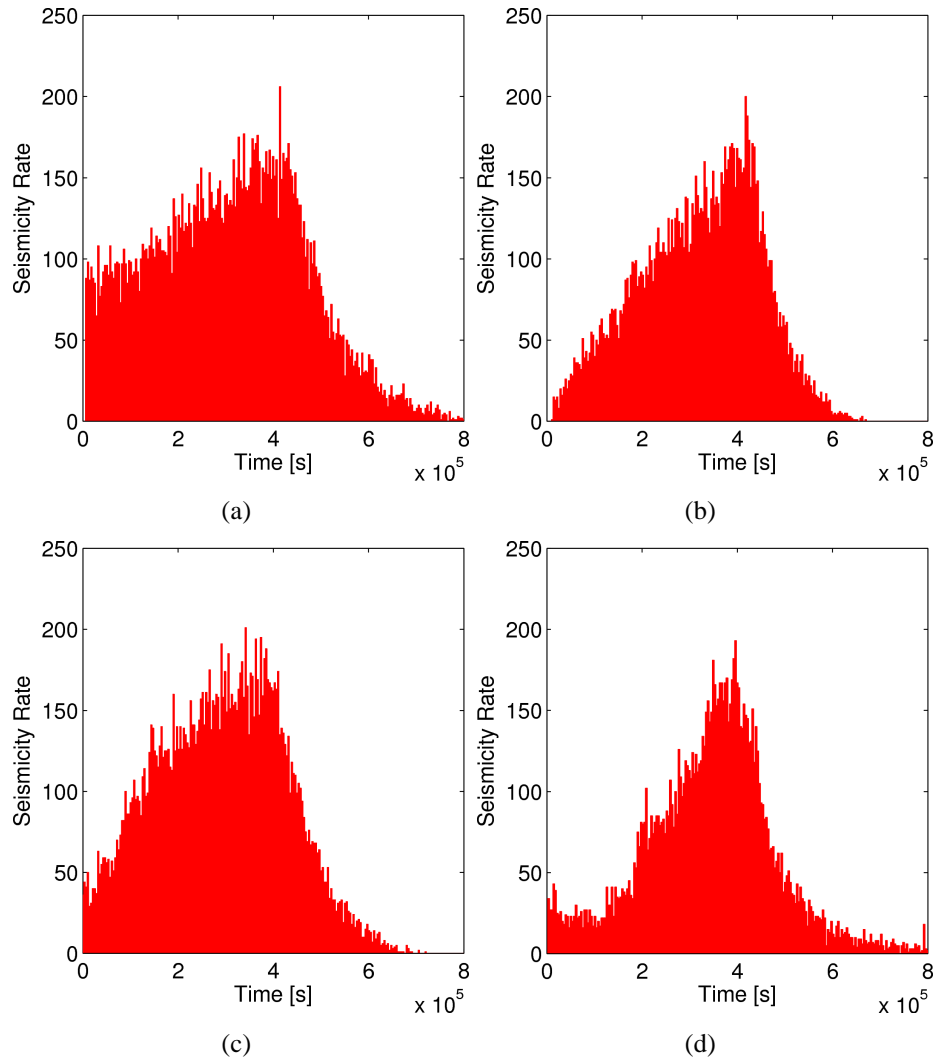


Figure 3.27: Seismicity rates resulting from different model set-ups (see Table 3.1): (a) Model 1, (b) Model 2 and (c) Model 3. (d) For a comparison, the rate of detected microearthquakes in Basel is shown.

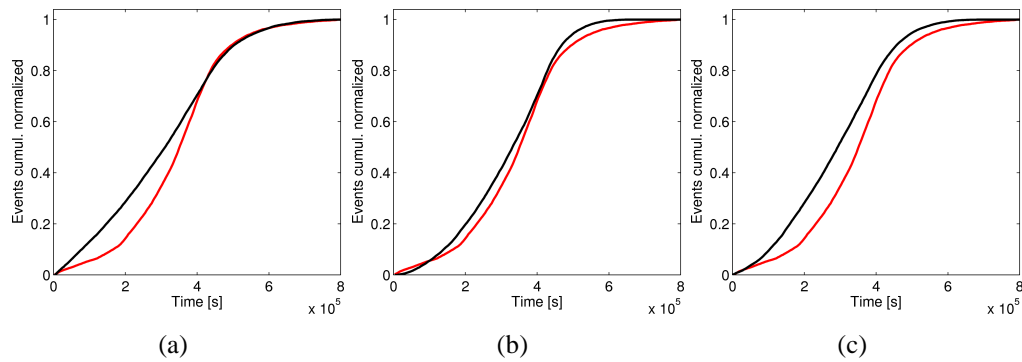


Figure 3.28: Comparison of normalized cumulative number of microearthquakes: (a) Model 1, (b) Model 2 and (c) Model 3. Red line marks the detected cumulative number and black line the modeled cumulative number.

extrapolated fracture volume concentration is most likely overestimated it hence gives an undervalued tectonic potential. I therefore conclude that analytically and numerically obtained tectonic potentials are in a good agreement.

It is also evident from Figure 3.27, however, that seismicity rate during injection and total number of induced microearthquakes differ in the presented models and, if compared to the Basel data, none of those completely reproduces the observed characteristics. The deviations can have following reasons. On the one hand, the approximated linearly increasing function of injection pressure (used in Model 1 and 2) simplifies the real situation. On the other hand, measurements of injection pressures (used in Model 3) can be inaccurate due to near-borehole effects including a non-linear fluid-rock interaction. A comparison of cumulative numbers of synthetical microearthquakes with observed microearthquakes also supports this conclusion (Figure 3.28).

These findings inspired the set-up of a fourth model where the injection flow rate has been used as a fluid mass source. Contrary to a possibly error-prone measurement of injection pressures, the applied flow rate is a precisely known parameter.

- Model 4: Basel mass flow rate

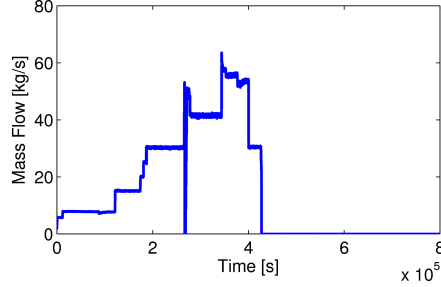


Figure 3.29: Source function applied in Model 4

– mass flow (product of fluid flow rate and fluid density)

–  $t_I = 430,000$  s

The applicability of such a model set-up for numerically calculating the pore pressure perturbation is confirmed by Rudnicki (1986). He rederived analytical solutions of pore pressure diffusion for fluid mass point sources in linear elastic, fluid-saturated, porous solid. The solutions emphasize the relation to solutions of the diffusion equation for injection pressure point sources although they are only presented for continuous injection at a constant rate. However, I assume that the similarity between the two solutions is preserved for the condition of time-dependent sources. According to Rudnicki (1986), the pore pressure perturbation can be calculated with:

$$p(r, t) = \frac{q_f}{\rho_0 D} \frac{A}{4\pi r} \cdot \operatorname{erfc} \left( \frac{r}{\sqrt{4Dt}} \right), \quad (3.23)$$

where  $q_f$  is the fluid flow rate,  $A = \frac{(\lambda_u - \lambda)(\lambda + 2\mu)}{\alpha^2(\lambda_u + 2\mu)}$  is a poroelastic constant including Lamé moduli  $\lambda$  and  $\mu$  for drained respectively  $\lambda_u$  for undrained response as well as Biot-Willis coefficient  $\alpha$ , and  $\rho_0$  is fluid density. Comparing this equation to the analytical solution for an injection pressure source (see also Chapter 3.2.1)

$$p(r, t) = \frac{q}{D} \frac{1}{4\pi r} \cdot \operatorname{erfc} \left( \frac{r}{\sqrt{4Dt}} \right) \quad (3.24)$$

with  $q = 4\pi D a_0 p_0$ , yields the following relation between flow rate  $q_f$  and injection pressure  $p_0$ :

$$q_f = \frac{4\pi D a_0 p_0 \rho_0}{A} \quad \text{respectively} \quad p_0 = \frac{q_f A}{4\pi D a_0 \rho_0}. \quad (3.25)$$

The result demonstrates a direct proportionality with a constant factor that depends on rock properties (diffusivity, poroelastic moduli), fluid density and the effective injections source radius. This scaling factor has to be considered in order to define the criticality limits,  $C_{min}$  and  $C_{max}$ , for generating synthetical microearthquakes.

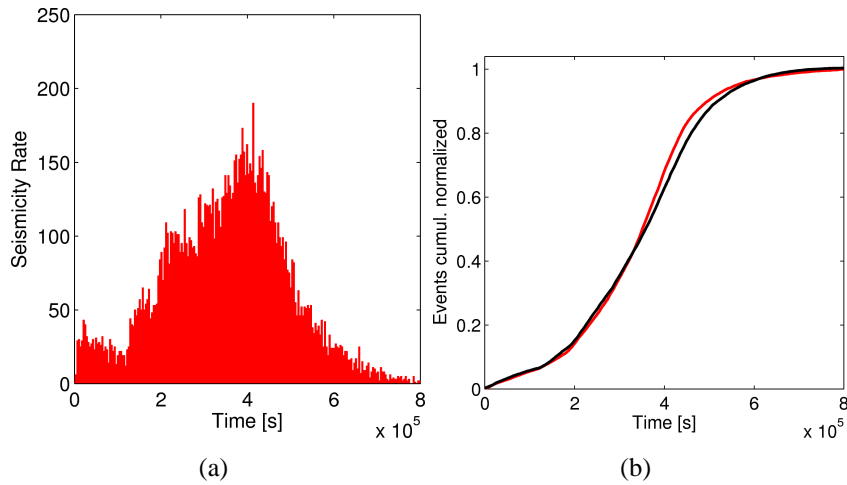


Figure 3.30: (a) Seismicity rate of induced microearthquakes obtained for Model 4 and (b) comparison of normalized cumulative number of microearthquakes. Red line marks the detected cumulative number and black line the modeled cumulative number.

The resulting seismicity rate of microearthquakes obtained from Model 4 is illustrated in Figure 3.30(a). The corresponding parameters  $C_{min}$ ,  $C_{max}$  and  $F_t$  are listed in Table 3.1. Several features, such as the step-like increase during injection, the maximum of seismicity rate and the decay following the injection stop, well coincide with the characteristics of the rate of detected microearthquakes (Figure 3.27(d)). A comparison of the cumulative event numbers presented in Figure 3.30(b) also shows this good agreement. It therefore confirms the correlation and sensitivity of seismicity triggering and applied flow rates in the case of the Basel reservoir stimulation.

### Reconstruction of critical pore pressures

The numerical modeling also allows to determine the critical pore pressure of each microearthquake. This gives the possibility to reconstruct the probability density function of criticality. At first, numerical modeling with the condition of anisotropically distributed hydraulic diffusivity is performed to obtain the pore pressure perturbation. Principal components of the diffusivity tensor,  $D_{11}$ ,  $D_{22}$  and  $D_{33}$ , have been estimated in Chapter 3.4.1 and are accordingly assigned to the model space. After the modeling, the 4D field of numerically obtained pore pressure perturbations,  $p(x, y, z, t)$ , is compared to the hypocenters and occurrence times of induced microearthquakes. The source locations are rotated

into the principal coordinate system of the tensor of hydraulic diffusivity. In this way, the critical pore pressure which was necessary to trigger a specific microearthquake is found for the whole set of events.

Figure 3.31(a) shows the cloud of induced microearthquakes. Each seismic event is color-coded according to its critical pore pressure. A similar representation is chosen for the corresponding  $r - t$  diagram which is presented in Figure 3.31(b). Since the two figures reveal nothing unexpected, highest critical pore pressures are in the vicinity of the fluid entry point and lowest are at the edge of the microseismic cloud, the focus now is on reconstructing the distribution function of criticality. For this purpose, the range of critical pore pressures is subdivided and the number of microearthquakes induced during injection is counted in each criticality interval. The resulting histogram of critical pore pressures in linear scale and in equally spaced logarithmic scale is shown in Figure 3.32. One can notice from this figure that the majority of microearthquakes were triggered by pressure perturbations less than  $50,000 Pa$  (Note that the second peak at  $200,000 Pa$  in Figure 3.32(b) is an artifact due to the equal spacing in logarithmic scale.). It is clear that the histogram is not reflecting the distribution function. The rock volume in which the pressure is perturbed, for instance, by  $1000 Pa$  is much larger than the volume of perturbation of  $1 MPa$ . Therefore the number of microearthquakes in each interval has to be scaled with the respective volume to obtain the probability density function (*PDF*) of criticality,  $f(C)$ . In addition, the *PDF* has to satisfy the condition that its integral over the range of critical pore pressures must equal unity:

$$P[C_{min} \leq X \leq C_{max}] = \int_{C_{min}}^{C_{max}} f(C) dC = 1, \quad (3.26)$$

This condition indicates that the probability  $P$  of a fluid-induced microearthquake to have a critical pore pressure between minimum and maximum criticality,  $X \in [C_{min}, C_{max}]$ , is equal to one.

The reconstructed probability density function of criticality is shown in Figure 3.32. Evidently, critical pore pressures are not uniformly distributed on the pre-existing fractures. Otherwise, the *PDF* would have a constant probability between minimum and maximum criticality. One can notice from Figure 3.32 that the probability of a microearthquake to occur at a pore pressure perturbation between approximately  $3000 Pa$  and  $13,000 Pa$  is about three to four times larger than at a higher perturbation and about two times larger than at a lower perturbation. Furthermore, the probability function indicates that maximum criticality is in the order of  $1 MPa$ . It thus confirms the result obtained from the analytical solutions. Following up the short discussion at the end of Chapter 3.4.2, the re-

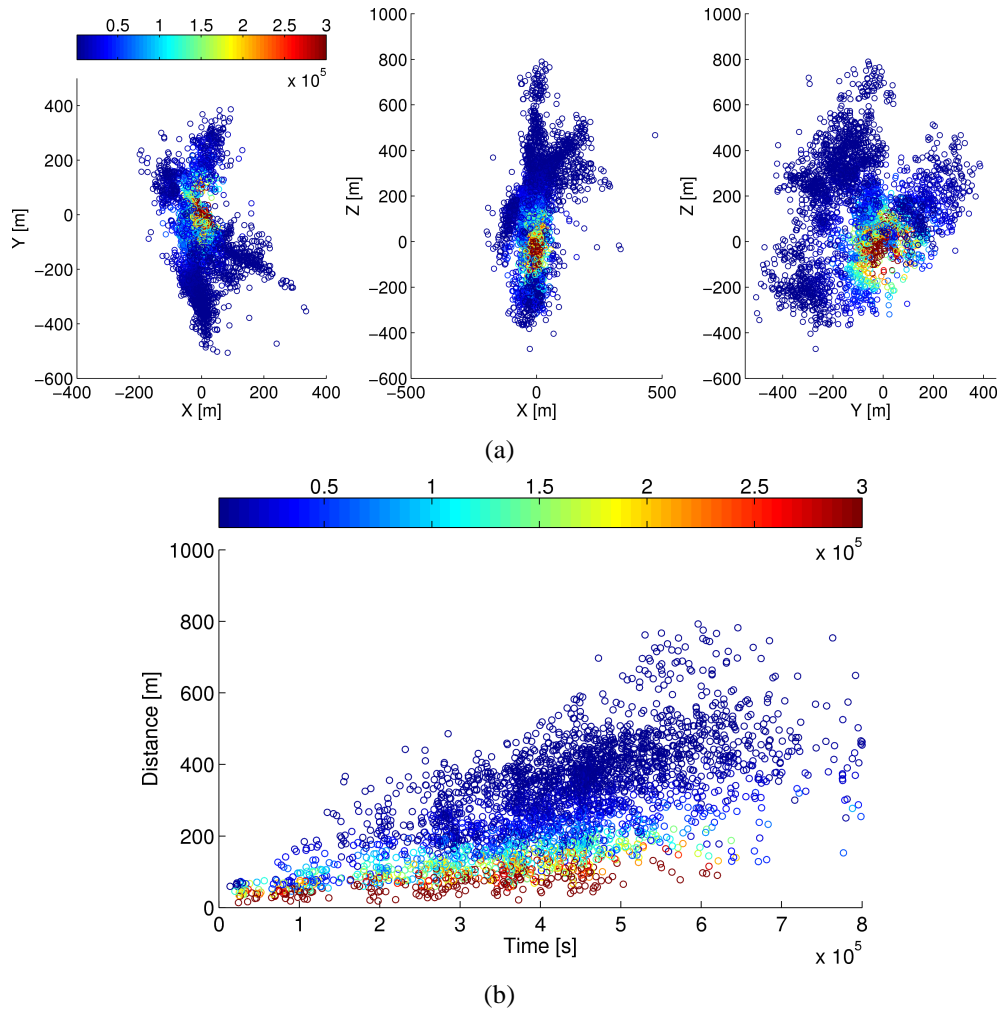


Figure 3.31: (a) Cloud of induced microearthquakes (02.12.-11.12.2006). Source locations are rotated into principal coordinate system of the diffusivity tensor. Microearthquakes are color-coded with their critical pore pressure in the interval  $1000 \text{ Pa}$  to  $0.3 \text{ MPa}$ . Coordinate origin  $\{0, 0, 0\}$  marks dominant fluid-entry point in  $4422 \text{ m}$  depth. (b)  $r-t$  diagram of microearthquakes. Color corresponds to critical pore pressure in the interval  $1000 \text{ Pa}$  to  $0.3 \text{ MPa}$ .

constructed probability density function of criticality allows no clear conclusions. Either a superposition of two uniform distributions of criticality addressing two differently oriented pre-existing fracture systems in the Basel reservoir or another type of distribution of criticality, such as unimodal or Weibull, can explain the reconstructed *PDF* of critical pore pressures. Therefore further investigations are required to precisely determine the statistical characteristics of pre-existing fractures in the Basel reservoir.

### 3.5 Summary and Conclusions

In many cases of borehole fluid injection experiments, injection pressures are kept constant or vary only a little over time. In these situations, pressure diffusion related signatures of fluid-induced seismicity can be examined and used for a reservoir characterization in consideration of solutions of the diffusion equation given by Carslaw and Jaeger (1973). If the condition of nearly constant injection pressure is not fulfilled, like for example by the hydraulic reservoir stimulation in Basel, application of *SBRC* methods, which base on the constraint of constant source, produces inaccurate results. These methods thus require a modification by introducing a set of equations which take into account a time-dependent source strength. I have here presented an analytical solution of diffusion equation valid for the special condition of linearly rising injection source pressure. The derived equations for pore pressure perturbation, seismicity rate and cumulative event number have been verified under usage of finite element modeling and synthetically generated microseismicity. I have then applied *SBRC* methods, which consider the spatial event density, the seismicity rate and the cumulative number of induced microearthquakes, to obtain estimates for the hydraulic diffusivity of the stimulated geothermal reservoir in Basel. Table 3.2 shows that the different methods provide consistent results which are conform to the results from the heuristically based approach of seismicity triggering fronts. The hydraulic diffusivity is proportional to the Darcy permeability of rock (Shapiro et al., 2003):

$$K = \frac{\eta}{N}D. \quad (3.27)$$

With a dynamic viscosity of the pore fluid at reservoir temperature,  $\eta(T = 190^\circ) = 1.75 \cdot 10^{-4} Pa \cdot s$ , and an approximation of the poroelastic modulus for granitic rock,  $N \approx [\frac{\phi}{K_f} + \frac{\alpha}{K_s}]^{-1} \approx 75 GPa$  (following parameters have been used here: porosity  $\phi = 0.01$ , Biot-Willis coefficient  $\alpha = 0.47$ , bulk moduli of water  $K_f = 3.3 GPa$  and solid constituents  $K_s = 45 GPa$  (see Detournay and Cheng, 1993)), the permeability is in the order of 150 *micro-Darcy*. This finding is in good agreement with a permeability estimate

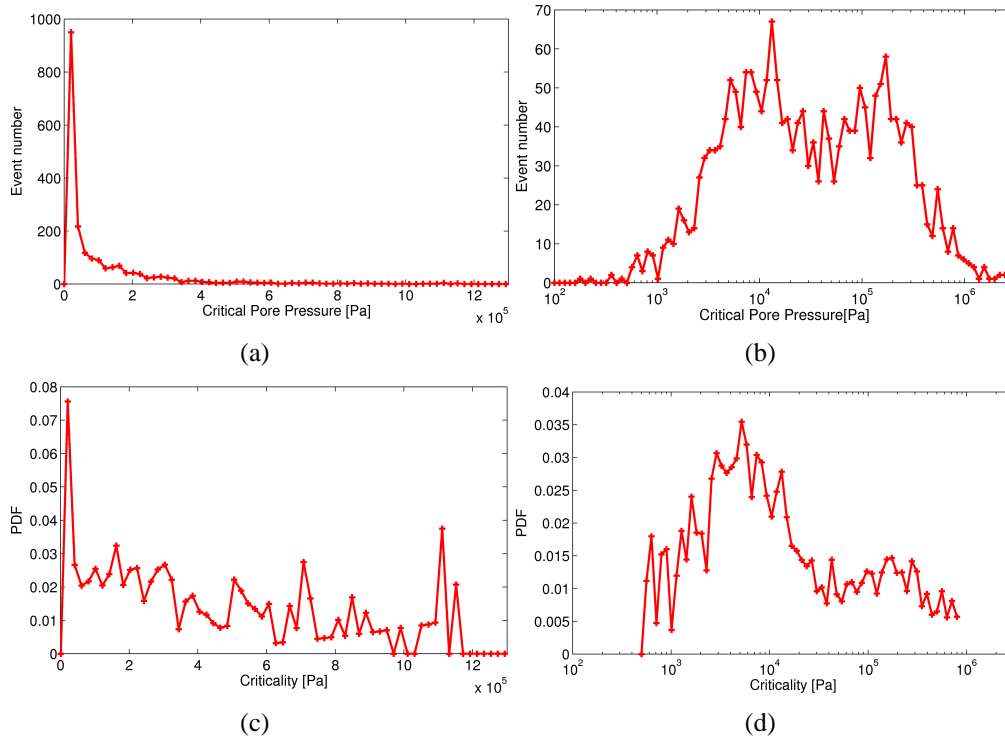


Figure 3.32: (Top) Histogram of critical pore pressures of induced microearthquakes. (Bottom) Reconstructed probability density function (*PDF*) of criticality. (Note that the accuracy of reconstructed *PDF* depends on the precision of hypocenter determination.) Figures (a) and (c): equally spaced linear scale, representing 100 samples in the interval  $[100 \text{ Pa} - 2 \text{ MPa}]$ . Figures (b) and (d): equally spacing in logarithmic scale, representing 100 samples in the interval  $[\log(100 \text{ Pa}) - \log(10 \text{ MPa})]$ . The advantage is a higher resolution of the presentation for critical pore pressures below 100,000 *Pa*.

	Method	Diffusivity D [ $10^{-2} \frac{m^2}{s}$ ]
heuristic	triggering front, isotropic	6.3
	triggering front, anisotropic	$diag(0.6, 2.9, 5.2)$
	triggering front, effective-isotropic	3.7
deterministic	back front	6.3
	event density	5.5
	seismicity rate	6.5
	event number after shut-in	5.5

Table 3.2: Summary of estimates of hydraulic diffusivity of the stimulated geothermal reservoir in Basel. The different methods of the *SBRC* approach provide consistent results.

from hydraulic data analysis conducted before the stimulation. Häring et al. (2008) give a value of 10 *micro-Darcy* for the rather undisturbed near-borehole area. It means that the permeability is enhanced by more than one order of magnitude due to the hydraulic stimulation.

Furthermore, I have evaluated the strength of pre-existing fractures of the Basel reservoir using the concept of criticality. According to the analytically as well as numerically obtained results, I conclude that this strength is defined by a criticality whose upper bound is below the maximum of pore pressure perturbation. It has been demonstrated that in such a situation the seismicity rate will reach its peak value after the injection is already stopped. In other words, the released seismic energy per time step should also be largest shortly after injection stop. It means that both higher number as well as larger magnitudes of induced microearthquakes can occur in this time period. This phenomenon is indeed observed in Basel where seismic events with largest magnitudes occurred after shut-in (Häring et al., 2008). For the lower bound of criticality I have obtained the following result. Application of the derived analytical equations to localized and detected seismicity yields a minimum criticality ranging from 5000 *Pa* to 9500 *Pa*. The latter value has been confirmed by modeling synthetical microseismicity which provided consistently defined criticality limits for all considered model set-ups. Determination of the critical pore pressures of microearthquakes induced during injection and reconstruction of the probability density function of criticality even give a lower

value of less than 1000  $Pa$ . The different estimates are likely caused by several factors, such as the consideration of hydraulically anisotropic or isotropic condition, of co-injection or post-injection seismicity and of located or detected microearthquakes. Interestingly, the reconstructed probability density function of criticality yields non-uniformly distributed critical pore pressures. It can be interpreted either as a superposition of two uniform distributions with different minimum and maximum criticality, or as a unimodal distribution with its maximum at about 5000  $Pa$ . Although the first interpretation can be concluded from the presence of two distinct fracture systems, the latter one can not be excluded and therefore further investigations are required.



# Chapter 4

## Interpretational Model for Single-Planar Hydraulic Fractures

### 4.1 Introduction

Hydraulic fracturing is the process of initiation and propagation of a fracture by injecting fluid at high flow rates resulting in pressures higher than the minimum horizontal stress  $S_{hmin}$ . It is one of several techniques for creating fractures which, for instance, are used to enhance the productivity of hydrocarbons, or to develop waste disposal sites (Fehler et al., 1987; Block et al., 1994; Keck and Withers, 1994). Since its introduction in the 1970's, the passive seismic monitoring has been used widely and successfully to estimate geometric parameters of hydraulic fractures (Albright and Pearson, 1982; Fehler et al., 1987; Warpinski et al., 1995; Urbancic and Rutledge, 2000; Fischer et al., 2008). The fracture azimuth, its lateral extension from the wellbore and its vertical growth can be evaluated using microearthquakes recorded from the fractured area during and after the injection. Relative source location techniques applied to the induced seismicity provide high resolution images which allow for resolving discrete fracture zones and better understanding source mechanisms of induced microearthquakes (Phillips et al., 1997; Rowe et al., 2002).

The microseismic imaging provides not only a spatial map of the final geometry of the fracture, it also has a significant potential to evaluate dynamic growth processes and to characterize physical processes related to fluid forced fracturing of reservoir rocks. Shapiro et al. (1997) introduced the *SBRC* (Seismicity Based Reservoir Characterization) method for analyzing spatio-temporal characteristics of fluid-induced microearthquakes. On the basis of linear diffusion of pore pressure perturbations, the *SBRC* methods allow to determine hydraulic properties

of the seismically active rock volume. The principle of these methods have been presented in the previous chapter by means of analyzing fluid-induced seismicity in a geothermal reservoir. However, the assumption of linear pressure diffusion is violated by the process of fracturing of a reservoir. As already mentioned in Chapter 2.3, fluid transport properties can strongly be enhanced by such an operation which led to the conclusion that a consideration of pressure-dependent hydraulic diffusivity has to be taken into account. In this case, a rather general non-linear diffusion law characterizes more accurately the physical process and mechanism of microearthquake triggering. The presented non-linear diffusion equation, Equation (2.12), provides us with a proportionality relation of the seismicity triggering front in dependence on the considered dimension of the diffusion problem. In the case of single-planar hydraulic fractures, which are in focus of this chapter, it predicts a linear with time behavior of the triggering front if a constant flow rate is applied during injection. The question arises how one can interpret fracturing-induced seismicity. The difficulty here is twofold. On the one hand, exact analytical solutions of the non-linear diffusion equation do not exist for the special conditions of a fluid injection. On the other hand, it should be intuitively to assume that other mechanisms can occur in addition to the fracturing process. Indeed, investigations of the dynamical evolution of fracturing-induced seismicity in the distance - time domain show that triggering of microearthquakes can be related to different processes: creation of new fracture volume, loss of fracturing fluid due to its infiltration into reservoir rocks, and diffusion of injection pressure into the surrounding rock and inside the fracture.

In this chapter an approach for interpretation of fracturing-induced seismicity is proposed which can be applied to single-planar hydraulic fractures. It allows to quantify both geometric as well as hydraulic characteristics of the fractured system. Simultaneously, hydraulic properties of the virgin reservoir can be determined too. This approach is applied to microseismic data recorded during several hydraulic fracturing experiments in the Carthage Cotton Valley gas field (Texas, USA). These well-documented fracturing experiments (e.g. Walker, 1997; Arco Exploration and Production Technology, 1997; Pinnacle Technologies, 1999; Rutledge and Phillips, 2003; Rutledge et al., 2004) allow testing of my findings. Since the hydraulic treatments were performed under different conditions, such as variations in treatment fluid, flow rate and proppant volume, influences of the treatment design on fracturing and induced seismicity can additionally be studied by comparing the results of two distinct situations.

## 4.2 Hydraulic Fracture Growth and Induced Seismicity

A hydraulic fracture will be initiated if the downhole pressure gets larger than the minimal principal stress. The direction of propagation of a fracture is in accordance with the orientation of the local stress field. In a homogeneous medium, the fracture grows perpendicular to the axis of minimal principal stress (Hubbert and Willis, 1957). The hydraulic fracturing of a rock usually activates microearthquakes. Their triggering mechanism is very similar to those one of stimulation-induced seismicity. The injected fluid causes an increase of the pore pressure and hence a decrease in the effective stress. In addition, the propagating fracture affects the stress state in its immediate vicinity due to tensile opening. Microearthquakes are then triggered along pre-existing natural fractures that are favorably oriented for slip (Pearson, 1981; Rutledge and Phillips, 2003; Shapiro et al., 2006a). Recent studies by Sileny et al. (2008) have shown that also microearthquakes are observed whose moment tensor solutions have only volumetric components which indicate them as tensile events.

For the investigation of fracturing processes and corresponding signatures of microseismicity it is firstly appropriate to consider a particular fracture geometry model. In general, several models are known which can be subdivided into three groups: planar  $2D$ , general and planar  $3D$ , and Pseudo- $3D$  models (Economides and Nolte, 2003). Since it is useful to start with a rather simple approximation the group of planar  $2D$  geometry models will be considered in the following.

The fracturing-induced microseismic data that will be discussed in this thesis were collected during hydraulic fracturing in horizontally layered sands and shales. The lateral extension of seismicity clouds is far longer than the vertical extent. For such situations, Perkins and Kern (1961) and Nordgren (1972) derived a  $2D$  fracture geometry model (the so-called PKN model, Figure 4.1(a)). In this model, fracture mechanics and fracture tip effects are not considered, but the focus is on fluid flow, and corresponding pressure gradients in the fracture (Economides and Nolte, 2003). Perkins and Kern (1961) assumed that a straight planar height-limited vertical fracture is propagating in a well-confined layer. Normal stresses in the layers above and below are large enough to prevent an out-of-zone growth of the fracture and plane strain conditions in the vertical direction are assumed. A plane strain deformation means that planes which were parallel before deformation remains parallel afterwards. This assumption is valid for fractures where one dimension, length or height, is much greater than the other. It is further assumed, as shown in Figure 4.1(a), that the cross section of the fracture body is of elliptical shape. However, Perkins and Kern (1961) neglected

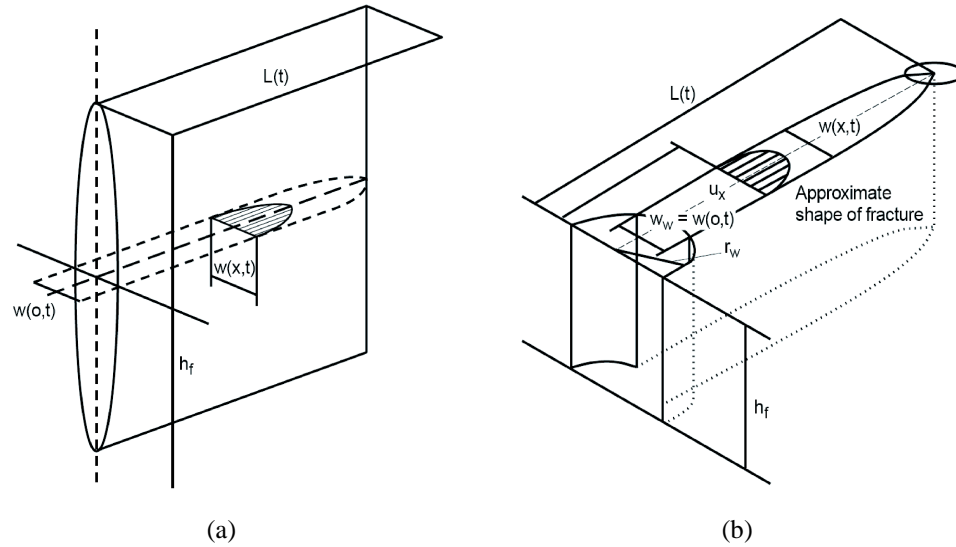


Figure 4.1: 2D hydraulic fracture geometry models: (a) PKN model and (b) KGD model (after Economides and Nolte, 2003).

fluid leakoff and storage of fluid within the fracture. They suggested to combine their model with the Carter leakoff model (Carter, 1957) to calculate both fracture width and fracture length. Nordgren (1972) introduced the equation of continuity (i.e., conservation of mass) to add fluid leakoff and storage to the Perkins and Kern model. To complete the group of planar 2D models, another geometry model should be mentioned which was derived by Khristianovich and Zheltov (1955) and later simplified and extended by Geertsma and de Klerk (1969) (the so-called KGD model, Figure 4.1(b)). It differs in two main aspects from the here used PKN model. Firstly, it assumes plane strain in the horizontal direction which becomes true in practice if the fracture height is much greater than the length. Secondly, the focus is on fracture mechanics and only simple assumptions are made concerning the fluid flow. Of particular interest in the KGD model is the region of fracture tip having zero fluid pressure and a sharp pressure gradient near the tip region whereas the fluid pressure is constant in the majority of the fracture.

To understand the dynamical behavior of the induced microseismicity an approximation of the process of fracture growth is applied that results from a volume balance principle of an incompressible treatment fluid. The volume balance states that the total volume of the injected fluid,  $V_I$ , equals the sum of the fluid volume which is stored in the created fracture,  $V_F$ , and the fluid volume which is lost into

the surrounding formation by leakoff,  $V_L$ :

$$V_I = V_F + V_L. \quad (4.1)$$

One can rewrite this equation by replacing  $V_I = Q_I t$ , where  $Q_I$  is the average injection rate of the treatment fluid and  $t$  is the injection time. The fracture volume  $V_F$  can be expressed by  $2 L h_F w$ , where  $L$  is the fracture half-length,  $h_F$  is the average fracture height and  $w$  is the average fracture width. The fluid loss volume  $V_L$  can be approximated by  $4 L C_L h_F \sqrt{2t}$  (Harrington and Hannah, 1975) that introduces the fluid-loss coefficient  $C_L$ . This leads to the following formulation for the half-length of a (symmetric) hydraulic fracture  $L$  as a function of injection time  $t$ :

$$L(t) = \frac{Q_I t}{4h_F C_L \sqrt{2t} + 2h_F w}. \quad (4.2)$$

In this equation, the two processes that are involved in the growth of a fracture are combined. On the one hand, there is the rupture process where new fractured volume will be created. On the other hand, leakage of fluid from the fracture into the surrounding rock takes place forming a fluid-invaded zone. It is assumed that both processes leave a characteristic imprint on the spatio-temporal evolution of induced microseismicity. Let us therefore consider Equation (4.2) in more detail. The first term in the denominator describes the total fluid loss from the fracture walls into the surrounding formation. It is proportional to  $\sqrt{t}$  and hence it has a diffusional character. The fluid-loss coefficient  $C_L$  is an important reservoir engineering parameter and is an active research topic. It depends on several factors, including, for instance, the relative permeability of the formation to the fluid-invaded zone, the hydraulic diffusivity of the reservoir, the pressure difference between fracture and reservoir, and the viscosity of the reservoir fluid (see also Equation (4.8)). The second term in the denominator of Equation (4.2) represents the contribution of the effective fracture volume and depends mainly on the geometry of the fracture vertical cross-section. The shape of the hydraulic fracture, in particular the width of a fracture, is a major objective in reservoir engineering.

Equation (4.2) is considered as a one-dimensional approximation for the triggering front of microseismicity in the case of a propagating hydraulic fracture. It is therefore an alternative formulation to the triggering front equation of microseismicity induced by a borehole fluid injection in a homogeneous, isotropic, permeable medium without creating a new fracture,  $r_t(t) = \sqrt{4\pi Dt}$  (see Equation (2.4)).

Although the fracture growth is a combination of two processes, it is still possible to consider two asymptotic situations. First, let us assume that in the beginning of an injection the treatment fluid is completely spent to create new fracture volume only and the loss of fluid is insignificant. Then Equation (4.2) can be simplified by neglecting the first term in the denominator:

$$L(t) = \frac{Q_I t}{2h_F w}. \quad (4.3)$$

Here the fracture half-length  $L$  is a linear function of the injection time  $t$ . The spatio-temporal characteristic of induced microearthquakes should obey this linear dependence. This means that microseismic events migrate roughly linear with time away from the injection well, indicating the rupture process.

On the other hand, the loss of treatment fluid from the fracture walls into the surrounding formation is getting large in the long-term limit of the injection. Therefore the corresponding term in Equation (4.2) is the dominant one and the geometry term can be neglected. The equation is then identical with the triggering front equation for a linear pore pressure diffusion (Equation (2.4)), with an apparent hydraulic diffusivity  $D = D_{ap}$  given by:

$$\begin{aligned} r(t) \equiv L(t) &= \frac{Q_i t}{4h_f C_L \sqrt{2t}} = \sqrt{4\pi D_{ap} t}, \\ D_{ap} &= \frac{Q_i^2}{128\pi h_f^2 C_L^2}. \end{aligned} \quad (4.4)$$

The evolution of the microseismic event cloud in space and time should show the typical diffusional signature ( $r \propto \sqrt{t}$ ).

Equations (4.2) to (4.4) provide a model that describes the process of hydraulic fracture growth as long as a treatment fluid is injected into reservoir rock. These equations relate the spatio-temporal dynamics of fracturing-induced seismicity to the fracture propagation. But also in the case of hydraulic fracturing, microseismicity can continue to occur even after shut-in of an injection. We have seen in Chapter 2.4 that this observation is well described by the concept of the back front of microseismicity Parotidis et al. (2004). Most of the microearthquakes occurring after the injection stop are located in the newly created hydraulic fracture volume. It means that pressure diffusion here takes place mainly in one dimension. For such a problem, the following equation for the back front of seismicity has already been introduced in Chapter 2.4:

$$x_{bf} = \sqrt{2Dt\left(\frac{t}{t_0} - 1\right)\ln\left(\frac{t}{t-t_0}\right)}. \quad (4.5)$$

In this equation,  $D \equiv D_f$  is the hydraulic diffusivity of the newly created fractured area.

### 4.3 Interpretation Flow Chart

The main idea of the interpretational approach is to estimate fluid loss using engineering data and geometric parameters of the fracture which can be derived from the induced microseismicity. Afterwards, the fluid loss can be used to estimate the permeability of the reservoir.

I have pointed out before that in the beginning of a treatment new fracture volume will be opened and the fluid loss can be neglected. If so, the width of a fracture can be calculated after rearranging Equation (4.3). Half-length  $L(t)$  and time  $t$  can directly be derived from the spatio-temporal distribution of events induced during the fracture volume opening phase. However, one can also apply an additional method to estimate geometric parameters of the fracture. Let us consider the time derivative of Equation (4.2) which is the tangent:

$$\begin{aligned} \frac{d\tilde{L}}{dt} &= \frac{X + \frac{1}{2}Y\sqrt{t}}{(X + Y\sqrt{t})^2}, & (4.6) \\ \text{where : } X &= (2h_F w)/Q_I, \\ Y &= (\sqrt{32}h_F C_L)/Q_I, \quad \text{and} \\ \tilde{L} &= L/Q_I. \end{aligned}$$

At time  $t = 0$  the tangent coefficient  $\frac{d\tilde{L}}{dt}$  is  $1/X$ . It provides the width of a fracture, or in combination with the fracture height, the cross section area:  $A = (X/2) \cdot Q_I$ . The tangent coefficient can simply be obtained by data fitting. Knowing the geometric parameters, one can then quantify the fluid loss from the fracture body using the volume balance principle (Equation 4.1). For this purpose, the comparison of injected fluid volume and newly created fracture volume gives the fluid leakage volume:  $V_L = Q_I t - 2L A$ . In the next step, the fluid loss coefficient  $C_L$  can be calculated after rearranging Equation (4.5):

$$C_L = \frac{Q_I t - 2L A}{4L h_F \sqrt{2t}}. \quad (4.7)$$

Furthermore, it now becomes possible to estimate the permeability  $\kappa$  of the virgin reservoir. If the definition of reservoir leak-off coefficient given in (Economides

and Nolte, 2003, chap A9) is considered and fracture surface effects are neglected, then one can write:

$$\kappa = \frac{C_L^2 \pi \eta}{\Delta p^2 \phi c_t}, \quad (4.8)$$

where  $\eta$  and  $c_t$  are viscosity respectively compressibility of the reservoir fluid,  $\phi$  is the porosity of the unfractured reservoir, and  $\Delta p$  is the difference of the pressure in the fracture (approximated by measured downhole pressure) and the initial reservoir pressure (approximated by hydrostatic pressure). Moreover, the fluid loss estimate permits to calculate the apparent hydraulic diffusivity according to Equation (4.4). The so defined hydraulic diffusivity can further be used in Equation (2.4). The resulting triggering front can be compared with the induced microearthquakes in the space-time domain for evaluation of the interpretational model.

The most important aspect of hydraulic fracturing is a strong enhancement of permeability for the production of hydrocarbons in rather low-permeable formations. The derived interpretational approach also allows for estimating the permeability of a newly created fracture. However, it is only possible if a back front of induced seismicity evolves after injection stop which can be identified from the spatio-temporal distribution of microearthquakes. According to Equation (4.5), the diffusion constant  $D_{bf}$  then corresponds to the hydraulic diffusivity of the fractured system. It can further be used to obtain the permeability of the fracture,  $\kappa_F$ , by the following relation (Shapiro et al., 2003; Economides and Nolte, 2003):

$$\kappa_F = c_F \eta_F \phi_F D_{bf}. \quad (4.9)$$

Here  $\eta_F$  and  $c_F$  are viscosity respectively compressibility of the treatment fluid, and  $\phi_F$  is the porosity of the fracture body. With both reservoir as well as fracture permeability one can finally calculate the dimensionless fracture conductivity,  $C_D$ , which is a key design parameter in hydraulic fracturing (Economides and Nolte, 2003, chap 12):

$$C_D = \frac{w \kappa_F}{L \kappa} = \frac{A \kappa_F}{h_F L \kappa} = \frac{4A \kappa_F}{S \kappa}, \quad (4.10)$$

with  $S$  being the surface of the fracture body. The geometric parameters, fracture width  $w$  and fracture half-length  $L$ , are included in this formulation. The dimensionless fracture conductivity is a measure of the ability of the fracture to transport fluid divided by the ability of the reservoir to feed the fracture. Another important design goal in reservoir fracturing is the effective wellbore radius,  $r_w$  (Economides and Nolte, 2003):

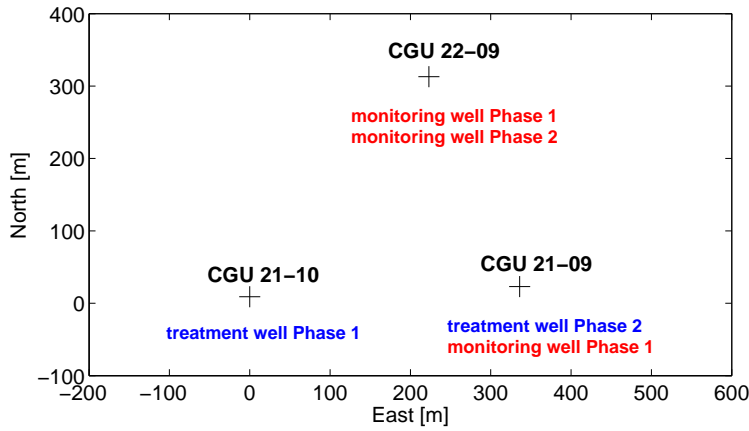


Figure 4.2: Well configuration and operational setup of the Carthage Cotton Valley hydraulic fracturing experiments in 1997 (Phase 1: gel proppant treatments, Phase 2: water treatments).

$$r_w \approx \frac{2}{\pi} L, \quad (4.11)$$

whereas here the altered pore pressure field around the fracture is not taken into account. It is an expression of the enlarged contact between wellbore and reservoir.

## 4.4 Application to Cotton Valley Data

In May and in July 1997, a consortium of oil field operators and service companies carried out a series of hydraulic fracturing experiments in the Carthage Cotton Valley gas field in East Texas, USA (Walker, 1997). The geological setting of the gas reservoir is defined by its location in the northern Gulf of Mexico sedimentary basin. The Cotton Valley formation consists of multiple, low-permeability sand layers within an interbedded sequence of sands and shales. The formation is approximately  $325m$  thick, its top is at a depth of about  $2600m$  within the study area (Rutledge and Phillips, 2003). A detailed description of the geology and of the stratigraphy of the Cotton Valley formation is given in Wescott (1984) and Walker (1997).

During the operation of the experiments different target zones within the Cotton Valley formation were hydraulically fractured. The operational setup is shown in Figure 4.2 and hydraulic treatment data are summarized in Table 4.1. In

	Phase 1		Phase 2		
	gel proppant frac		water frac		
	Stage A	Stage B	Stage C	Stage D	Stage E
Flow rate [ $l/s$ ]	119	106	26.5	26.5	26.5
Injected volume [ $m^3$ ]	1340	1253	419	396	400
Bottom hole pressure [ $MPa$ ]	39-43	41-47	45-52	45-52	45-54
Injected proppant [ $kg$ ]	230,000	190,000	15,000	12,000	7000
Perforated interval [ $m$ ]	81	81	36	24	17

Table 4.1: Treatment data of Carthage Cotton Valley hydraulic fracturing experiments in May (Phase 1) and July (Phase 2) 1997.

Phase 1, fracturing was performed using well CGU21-10 as the treatment well. The treatment fluid was a cross-linked polymer gel with added proppant. The induced microearthquakes were detected and registered by borehole geophone arrays placed in two monitoring wells, CGU21-09 and CGU22-09. Initial source locations were determined using P- and S-wave traveltimes and P-wave particle motion data (Rutledge and Phillips, 2003). Subsequently, the event locations were improved through high-precision repicking of P- and S-phase onsets (Rutledge and Phillips, 2003). In Phase 2, fracturing was performed via perforated domains of well CGU21-09 and monitored by the borehole sensors in well CGU22-09 only. Here a water based fluid was used for the treatment. Induced microearthquakes were located using the same approach as in Phase 1.

Each of the two phases included several stages of hydraulic fracturing, but precisely determined hypocenters of induced microearthquakes are only available for three stages: two gel treatments and one water treatment. In the following, two fracturing experiments will be considered in more detail. These are Stage A, a gel treatment, and Stage C, a water treatment. Since both treatments were performed under different treatment conditions (such as fluid type, flow rate, proppant volume) a comparative analysis can be undertaken to additionally investigate the influence of the treatment design on the fracturing process. The precisely determined source locations of the two corresponding microseismic event clouds are shown in Figure 4.3. The observed asymmetric distribution of Stage A microearthquakes with respect to the treatment well is likely to be caused by the po-

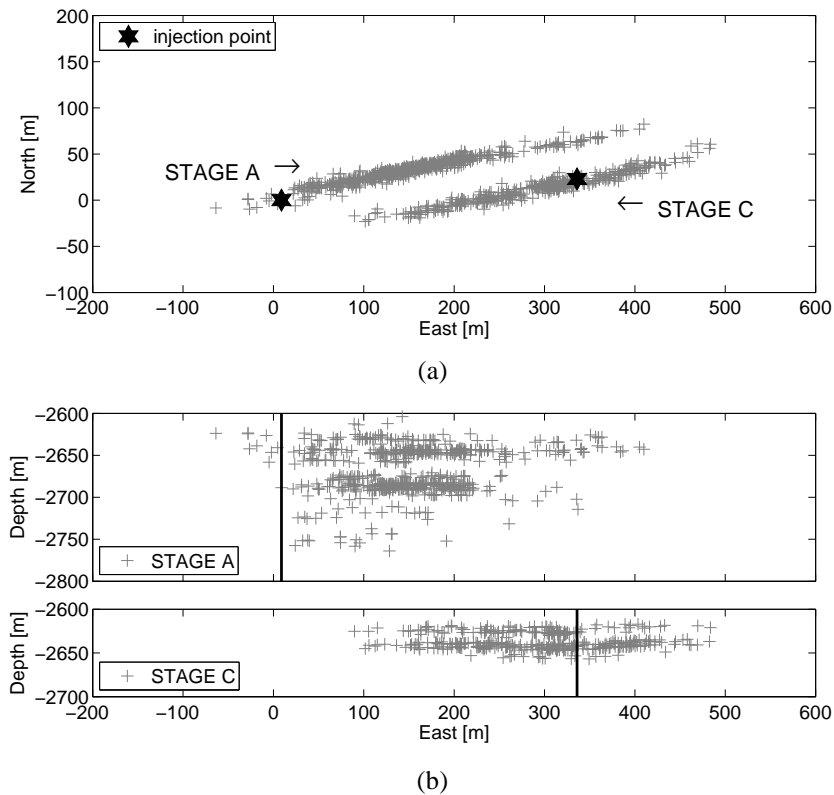


Figure 4.3: (a) Map view and (b) depth view of source locations of microearthquakes induced in Stage A gel treatment and in Stage C water treatment.

sition of receivers (Figure 4.2). Rutledge and Phillips (2003) argued for a limited detection range of the monitoring system. They calculated a magnitude-distance threshold and could show that about 93% of microseismic events east of the treatment well would not have been detected if they had been triggered in same distance west of the well. Thus, the treatment could have resulted in a symmetric fracture.

#### 4.4.1 A Gel Treatment

Here the interpretation of microseismicity recorded in the Stage A treatment is presented. To study the dynamical behavior via the spatio-temporal evolution of the seismicity cloud, the distance of a microearthquake to the nearest wellbore perforation point is plotted as function of the occurrence time relative to the time of begin of the treatment ( $r - t$  diagram, Figure 4.4(c)). The fracturing was per-

formed in multiple cycles of injection in a typical hydraulic fracturing sequence: mini-frac, step rate test and main treatment (Figure 4.4(a)). The cessations of injection allow the fracture to close if no proppant is added, and to reopen in the following injection cycle. Such behavior can be identified in the  $r - t$  diagram of microseismicity (Figure 4.4(e)). Let us consider only the first minutes of each of the injection cycles. One can see the quasi-linear event migration with time away from the treatment well. In my understanding, it represents opening, and in subsequent injection cycles, reopening, and further propagation of the fracture. The similarity in the velocity of fracture (re)opening in the three individual injection cycles (velocity of fracture propagation,  $v \sim 0.17 \text{ m/s}$ ) indicates that reopening takes place with approximately the same geometry (width and height) of the fracture.

### Estimate of Fluid Loss Volume

The first step is to determine the volume of the newly created fracture. I have only used microearthquakes which were triggered in the main treatment period to estimate the fracture cross-section area according to Equation (4.7). The tangent coefficient at time  $t = 0 \text{ s}$  is obtained by data fitting which results in  $A = 0.22 \text{ m}^2$ . The best fit is shown in Figure 4.5(a). Under the assumption that the fracture height is equal to the total perforated section of the treatment well,  $h_F \sim 80 \text{ m}$ , then the average fracture width  $w$  is  $\sim 3 \text{ mm}$ . The uncertainty in the estimate of fracture width is relatively high due to the simplified assumption on fracture height. However, with known cross-section area and length of the fracture one can calculate its volume and compare it with the injected volume: in Stage A the total injected fluid volume was  $V_I = 1340 \text{ m}^3$  and the resulting fracture volume is  $V_F = 176 \text{ m}^3$ . Since a conservation of fluid volume is assumed, it means that  $\sim 85\%$  of the injected volume was lost into the formation.

### Estimate of Reservoir Permeability

The controlling parameter of fluid leakage is the fluid-loss coefficient  $C_L$ . According to Equation (4.7) it is  $5.2 \cdot 10^{-5} \text{ m/s}^{1/2}$ . In addition, a diffusion constant which is characterizing the diffusional fluid leakage process can be determined. Introducing  $C_L$  into Equation (4.4), the apparent hydraulic diffusivity is  $D_{ap} = 2 \text{ m}^2/\text{s}$ . However, this diffusion constant is apparent only and not directly related to triggering of microearthquakes by a diffusion of pore pressure perturbations. Nevertheless, for a simple quality control a triggering front according to Equation (2.4) with  $D = 2 \text{ m}^2/\text{s}$  can be calculated and then plotted along with the induced microseismicity. One can see in Figure 4.5(c) that the growth of the event cloud following the fracture volume opening obeys a behavior similar to triggering by

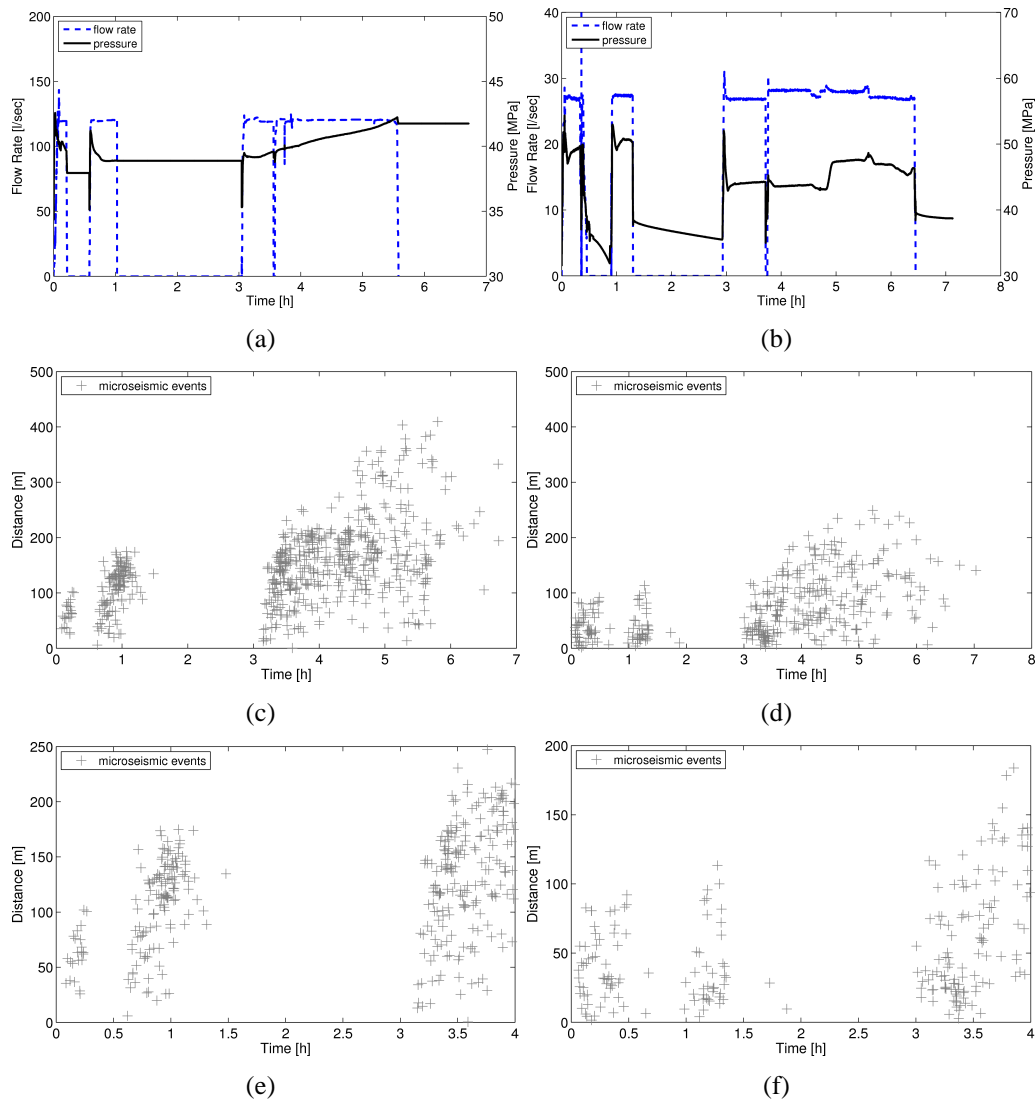


Figure 4.4: (a) Hydraulic fracturing treatment data, (c)  $r-t$  diagram of induced microearthquakes of Stage A gel treatment. (e) Detail of (c) to highlight the phases of fracture volume opening. Figures (b), (d), and (f) are the equivalent of Stage C water treatment.

linear pore pressure diffusion. The fluid-loss coefficient in turn is related to the reservoir permeability as it is shown by Equation (4.8). With typical values for the Cotton Valley tight gas reservoir (hydrocarbon gas at a temperature of  $120^\circ C$  and hydrostatic pressure of  $p = 28 MPa$ ): viscosity  $\eta = 3 \cdot 10^{-5} Pa \cdot s$ , compressibility  $c_t = 3.5 \cdot 10^{-8} Pa^{-1}$ , reservoir porosity  $\phi \leq 0.1$  (Walker, 1997), and pressure difference  $\Delta p = 16 MPa$ , the virgin reservoir permeability  $\kappa$  is of the order of 1 *microDarcy*. To verify the results, a modified  $r - t$  diagram where times of shut-in phases between the three injection cycles have been removed is shown in Figure 4.5(e). In addition, the triggering front for fracturing-induced seismicity according to Equation (4.2) is presented. It is calculated with the parameters as estimated before (fracture cross-section area and fluid-loss coefficient). One can see that the curve well limits (as the upper envelope) the distribution of induced microearthquakes in the spatio-temporal domain.

A further possibility for validating the obtained results, in particular the estimate of permeability, is explained by the following consideration. It is clear that a large part of fracturing-induced microearthquakes are likely to be triggered due to the diffusion-like leakage of fluid from the fracture walls into the surrounding formation. This diffusion is controlled by the permeability respectively hydraulic diffusivity of the virgin reservoir. The fracture itself can be seen as a fluid feeding zone (comparable to an open hole section of a wellbore). I have now calculated the minimum distance of each microearthquake to a hypothetical fracture plane which is obtained by linear regression of the microseismicity cloud. The corresponding  $r - t$  diagram is presented in Figure 4.6(a). The fitting upper envelope according to Equation (2.4) should provide an estimate of hydraulic diffusivity that is equivalent to the diffusivity of the reservoir. For comparison, the latter can be calculated from the permeability  $\kappa$  using  $D = \frac{N}{\eta} \kappa$ . The dynamic viscosity of hydrocarbon gas is  $\eta = 3 \cdot 10^{-5} Pa \cdot s$ , and the poroelastic modulus is defined as  $N \approx [\phi/K_f + \alpha/K_s]$  with porosity  $\phi = 0.1$ , bulk modulus of fluid phase  $K_f = 30 MPa$ , Biot-Willis coefficient  $\alpha = 0.5$ , and bulk modulus of solid constituents  $K_s = 40 GPa$ . In this way, it results in a hydraulic diffusivity of the order of  $10^{-5} m^2/s$ . The triggering front in the  $r - t$  diagram yields a value of  $D = 5 \cdot 10^{-4} m^2/s$ . Since several factors have an influence on both estimates, such as precision of hypocenter locations, definition of fracture plane or assumptions regarding the poroelastic constants, I conclude that they are of similar order of magnitude.

### Estimate of Fracture Permeability and Conductivity

After completion of the hydraulic treatment, a back front of seismicity develops which can be identified from the  $r - t$  diagram (Figures 4.5). The signature provides  $D_{bf} = 4 \text{ m}^2/\text{s}$  for the hydraulic diffusivity of the fractured area. This value is obtained by varying  $D_{bf}$  in Equation (4.5) to match the microseismic data. Introducing the hydraulic diffusivity into Equation (4.9) and assuming an enhanced porosity of  $\phi_f = 0.3$  gives a fracture permeability  $\kappa_F$  in the order of some 10 *Darcy*. Thus, there is an increase in permeability about seven orders of magnitude due to the fracturing of the reservoir rock. Finally, two further characteristics of reservoir engineering can be derived: dimensionless fracture conductivity,  $C_D$ , and effective wellbore radius,  $r_w$ . Using Equation (4.10) and Equation (4.11) results in  $C_D = 2000$  and  $r_w = 255 \text{ m}$ , respectively.

### 4.4.2 A Water Treatment

The focus here is on the interpretation of Stage C induced microseismicity. Additionally, I will compare the results obtained for both water and gel treatment. Microearthquakes in the distance-time domain are shown in Figure 4.4(d). Contrary to the intuitive expectation that more fluid will be lost into the formation by leakage (because of the lower viscosity of the treatment fluid) the  $r - t$  diagram is not showing such an effect. An explanation for this phenomenon could be the lower fluid volume that was injected at lower flow rates (Table 4.1) on the one hand, or a less dense population of pre-existing natural fractures at the location of Stage C on the other hand.

### Estimate of Fluid Loss Volume

The characteristic fracture opening and subsequent reopening phases are observable in the  $r - t$  diagram (Figure 4.4(f)). The velocity of fracture propagation is  $\sim 0.2 \text{ m/s}$ . Although the treatment design differed from the gel fracturing (Table 4.1), the water treatment resulted in a similar fracture geometry. Estimation of the cross-section area yields  $A = 0.13 \text{ m}^2$ . It is again assumed that the fracture height  $h_F$  is equal to the total perforated domain of the treatment well ( $\sim 36 \text{ m}$ ), which then yields an average fracture width  $w \sim 4 \text{ mm}$ . The water treatment resulted in a fracture volume  $V_F = 65 \text{ m}^3$ . Hence it is much less than the volume of the Stage A fracture. However, by taking into account that the volume of injected fluid was significantly lower ( $V_I = 419 \text{ m}^3$ ), then the ratio of fracture volume and fluid loss volume is nearly identical in both treatments. Therefore the fracturing process seems to be decoupled from the type of treatment fluid. Another point which supports this speculation is the seismic moment release. Rutledge et al. (2004)

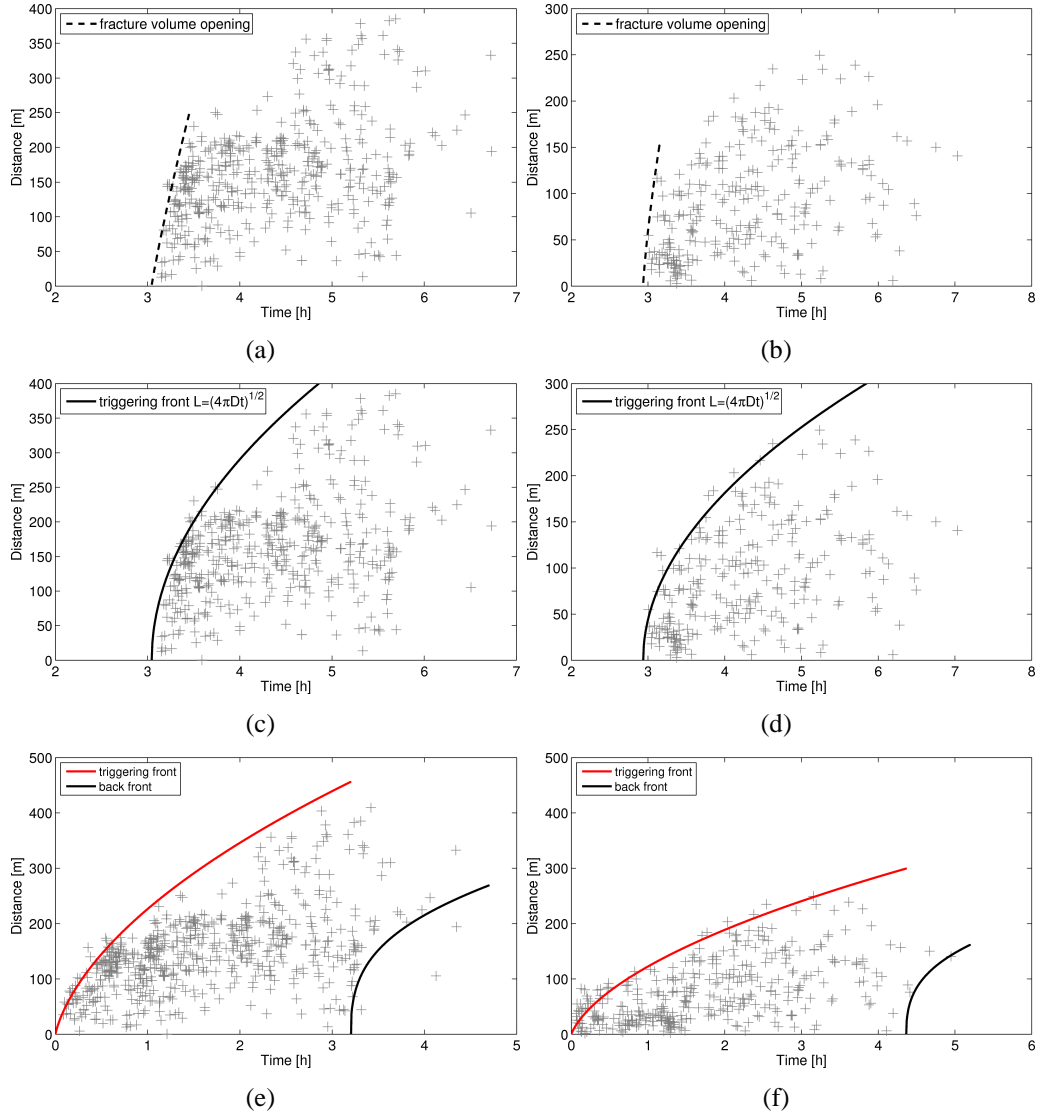


Figure 4.5: (a)  $r - t$  diagram of microearthquakes induced in main treatment period of Stage A gel treatment, dashed line indicates fracture volume opening. (c)  $r - t$  diagram as in (a) but with triggering front curve according to Equation 2.4 to describe the diffusion-like propagation of seismicity. (e) Modified  $r - t$  diagram with removed shut-in phases. Triggering and back front curves according to Equations (4.2) and (4.5) well limit the microseismic event cloud. (b), (d) and (f) are the equivalent of Stage C water treatment.

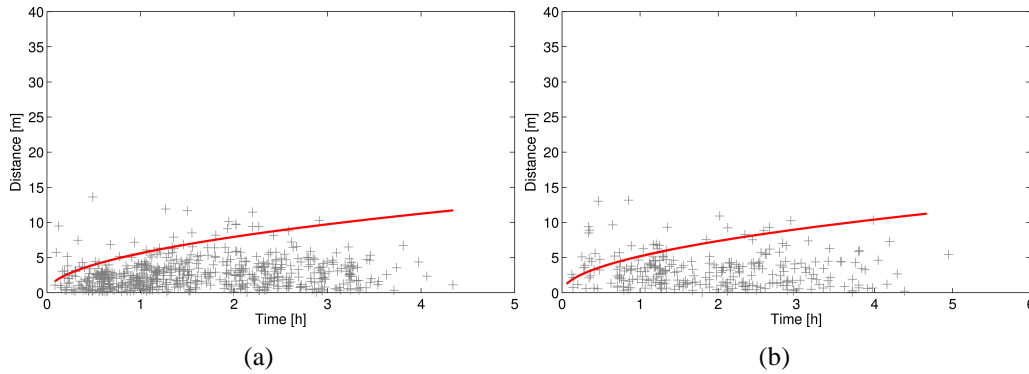


Figure 4.6: (a) Modified  $r - t$  diagram of microearthquakes induced in Stage A gel treatment and (b) in Stage C water treatment. The distance corresponds to the distance of each microearthquake to a hypothetical fracture plane under the assumptions given in the text. The triggering front curve according to Equation 2.4 is then used to derive a hydraulic diffusivity which should be equivalent to the diffusivity of the virgin reservoir.

compared cumulative moment release versus cumulative injected volume for the various treatments. Because cumulative seismic moment describes total seismic deformation, it should be proportional to the created volume. The gel treatment and the water treatment have an identical moment release per unit volume injected (Figure 4.7). It supports the conclusion that the fluid loss was similar in both treatments. If fluid leakage in water treatment was higher, it should be reflected by a smaller normalized moment release.

### Estimate of Reservoir Permeability

The fluid-loss coefficient  $C_L = 4.6 \cdot 10^{-5} \text{ m/s}^{1/2}$  is therefore similar to the one obtained in the gel treatment. The coefficient is again transferred to an equivalent diffusion constant ( $D_{ap} = 0.6 \text{ m}^2/\text{s}$ ). A triggering front curve (Equation 2.4) based on this apparent hydraulic diffusivity limits the microseismicity apart from the volume opening phase in the  $r - t$  diagram as shown in Figure 4.5(d). The fluid-loss coefficient is then used to calculate the reservoir permeability which yields  $\kappa = 9 \cdot 10^{-8} \text{ Darcy}$ . This permeability value is in fact smaller by a factor four than the estimate from the gel treatment. One reason may be the higher pressure difference  $\Delta p = 26 \text{ MPa}$ . Nonetheless, in my opinion the following aspect also has to be taken into account. If proppant is pumped into a fracture it will be transported to the fluid-invaded zone around the fracture body as well. As a consequence, it affects fluid loss, pressure field, and hence also the estimate of reservoir

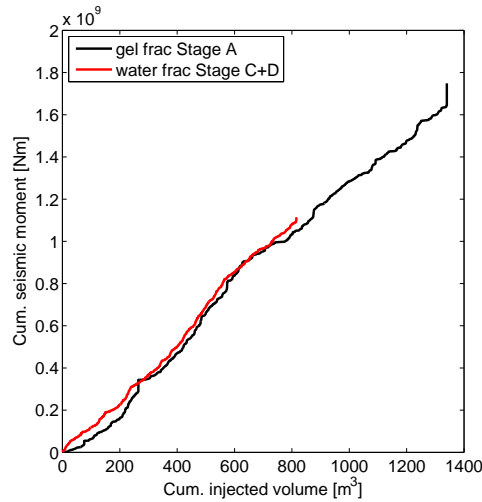


Figure 4.7: Cumulative seismic moment versus cumulative injected fluid volume. Stages C and D of water treatments were combined to correspond to the same depth interval as Stage A gel treatment (Rutledge et al., 2004).

permeability using induced seismicity. The water treatment was performed without a significant amount of proppant (Table 4.1), which can be an explanation for the rather slightly different estimates of reservoir permeability. From this estimate I have calculated a hydraulic diffusivity and compared it to an estimate obtained from  $r - t$  analysis as described in the previous subsection. Also for Stage C seismicity, the comparison yields a good agreement between both estimates.

### Estimate of Fracture Permeability and Conductivity

The back front of induced seismicity (Figure 4.5(f)) provides for the hydraulic diffusivity of the fractured area  $D_{bf} = 1.8 \text{ m}^2/\text{s}$ , which is smaller compared to the gel treatment. Despite rather insufficient statistics of post-treatment seismicity, the presented best fit curve is still reasonable. The fracture permeability  $\kappa_F$  of approximately 1 *Darcy* is one order of magnitude lower than the fracture permeability of the gel treatment. I suppose that this difference is likely to be caused by the strongly reduced volume of pumped proppant. It results in a decline of the fracture width after shut-in due to missing resistance against horizontal stresses. Consequently, the fracture permeability will be affected by this closure. A decreasing fracture width also affects the dimensionless fracture conductivity (see Equation 4.10). Keeping this in mind, the here obtained value  $C_D = 165$  should be seen as an upper limit only. For completeness, the effective wellbore radius in

the case of Stage C treatment is  $r_w = 159 \text{ m}$ .

### 4.4.3 Summary of Results

I have analyzed three stages of hydraulic fracturing in Cotton Valley. These are two gel treatments (Stage A, Stage B) and one water treatment (Stage C) (see figure section in Appendix for Stage B microseismicity). Table 4.2 summarizes geometric and hydraulic parameters resulting from the application of the interpretational approach to the induced microearthquakes. We can notice two interesting points if we compare the obtained results. Independent on the design parameters of the treatments, such as treatment fluid and injection flow rates, the ratio of fractured volume and lost fluid volume is nearly identical in all considered stages. This finding suggests that rather the fluid-loss coefficient, which is to some extent related to the reservoir permeability, is a significant factor in the process of fracturing than the treatment design. But, obviously the permeability of a fracture is affected by the treatment parameters in two ways. On the one hand, the cross-linked gel has a higher viscosity compared to water ( $\eta_{gel} = 150 \cdot 10^{-3} \text{ Pa s}$ ,  $\eta_{water} = 3 \cdot 10^{-3} \text{ Pa s}$  (Rutledge et al., 2004)) which results in a larger permeability (see Equation 4.9). On the other hand, the pumped proppant also positively influences the fluid transport properties within the fractured area since it keeps newly created fluid pathways open after shut-in of the injection.

## 4.5 Modeling of Fracture Propagation

The inversion of microseismic event data in order to model the growth of hydraulic fractures is done using the maximum likelihood estimation (MLE) method. The idea behind MLE is to determine the parameters that maximize the probability, or likelihood, of given data. The method of maximum likelihood is considered to be robust (Hainzl, 2007) and it can be applied to most models and different types of data. In addition, MLE provides efficient methods for quantifying uncertainty through confidence intervals (Kay, 1993).

The MLE method is based on the probability density function *PDF* for each microseismic data point  $x$  which is represented by its spatio-temporal position:

$$PDF = f(x; C_1, C_2, \dots, C_k), \quad (4.12)$$

where  $C_1, C_2, \dots, C_k$  are  $k$  unknown constant parameters which needs to be estimated. Then the likelihood function is given by the following product:

$$L(x_1, x_2, \dots, x_N | C_1, C_2, \dots, C_k) = L = \prod_i^N f(x_i; C_1, C_2, \dots, C_k), \quad (4.13)$$

	Stage A	Stage B	Stage C
Fracture half-length $L$ [m]	400	280	250
Cross-section $A$ [m <sup>2</sup> ]	0.22	0.29	0.13
Fracture width $w$ [mm]	2.8	3.6	3.6
Fracture volume $V_F$ [m <sup>3</sup> ]	176	163	65
Fluid loss volume $V_L$ [m <sup>3</sup> ]	1164	1090	354
$V_L$ , in relation to $V_I$	86 %	87 %	85 %
Fluid-loss coefficient $C_L$ [ $\frac{m}{s^{1/2}}$ ]	$5.2 \cdot 10^{-5}$	$7.7 \cdot 10^{-5}$	$4.6 \cdot 10^{-5}$
Reservoir permeability $\kappa$ [Darcy]	$3.7 \cdot 10^{-7}$	$4.4 \cdot 10^{-7}$	$9 \cdot 10^{-8}$
Fracture diffusivity $D_{bf}$ [ $\frac{m^2}{s}$ ]	4	0.9	1.8
Fracture permeability $\kappa_F$ [Darcy]	80	20	1
Fracture conductivity $C_D$	2000	890	165
Effective wellbore radius $r_w$ [m]	255	178	159

Table 4.2: Summary and comparison of the results that were obtained by interpretation of fracturing-induced seismicity resulting from gel and water treatments in Carthage Cotton Valley gas field. Despite different treatment parameters, the ratio of fractured volume and lost fluid volume is nearly identical in both type of treatments. Differences in the hydraulic characteristics of the two fractures are likely to be caused by the different mass of pumped proppant in gel and water treatments (see Table 4.1).

with  $N$  being the number of observed microseismic events and  $i$  being the index of each individual event. The maximum likelihood estimators of parameters  $C_k$  are obtained by maximizing  $L$ . It is mathematically much easier to work with the logarithm of Equation (4.13) which is the so-called log likelihood function:

$$\Lambda = \ln L = \sum_i^N \ln f(x_i; C_1, C_2, \dots, C_k). \quad (4.14)$$

To estimate the parameters  $C_k$  that describe the fracture growth, it is sufficient to consider the triggering front given in Equation (4.2). The probability that a microearthquake occurs at point  $x$  can then be expressed by the probability density function  $f(x, L(t))$ . In case of uniformly distributed source locations of induced microearthquakes the probability density function is given by:

$$\begin{aligned} f(x, L(t)) &= \frac{1}{2L(t)} & \text{if } |x| \leq L(t) \\ f(x, L(t)) &= 0 & \text{else.} \end{aligned} \quad (4.15)$$

However, to apply this model the location uncertainties have also to be taken into account. Assuming that those are Gaussian distributed:

$$f_G(x) = \exp\left(\frac{-x^2}{2\sigma^2}\right) / \sqrt{2\pi}\sigma, \quad (4.16)$$

then the probability density function of an event becomes:

$$f(x, L(t)) = 0.5 \left( \operatorname{erf}\left(\frac{L(t) - x}{\sqrt{2}\sigma}\right) + \operatorname{erf}\left(\frac{L(t) + x}{\sqrt{2}\sigma}\right) \right) \cdot (2L(t))^{-1}, \quad (4.17)$$

with the Gaussian error function  $\operatorname{erf}(x) = \frac{2}{\sqrt{\pi}} \int_0^x e^{-t^2} dt$ . Thus the following log likelihood function is obtained:

$$\Lambda = \sum_i^N \left[ \ln \left( \operatorname{erf}\left(\frac{L(t_i) - x_i}{\sqrt{2}\sigma_i}\right) + \operatorname{erf}\left(\frac{L(t_i) + x_i}{\sqrt{2}\sigma_i}\right) \right) - \ln(4L(t_i)) \right] \quad (4.18)$$

Using this equation, the set of parameters which control the growth of a fracture can be estimated. In the application to the data, the triggering front equation for fracturing-induced seismicity, Equation (4.2), is simplified to have only two independent parameters to be maximized,  $C_1$  and  $C_2$ :

$$\begin{aligned} L(t) &= \frac{t}{C_1 + C_2\sqrt{t}}, & (4.19) \\ \text{where : } C_1 &= 2h_f w / Q_i \quad \text{and} \\ C_2 &= 4h_f C_L \sqrt{2} / Q_i. \end{aligned}$$

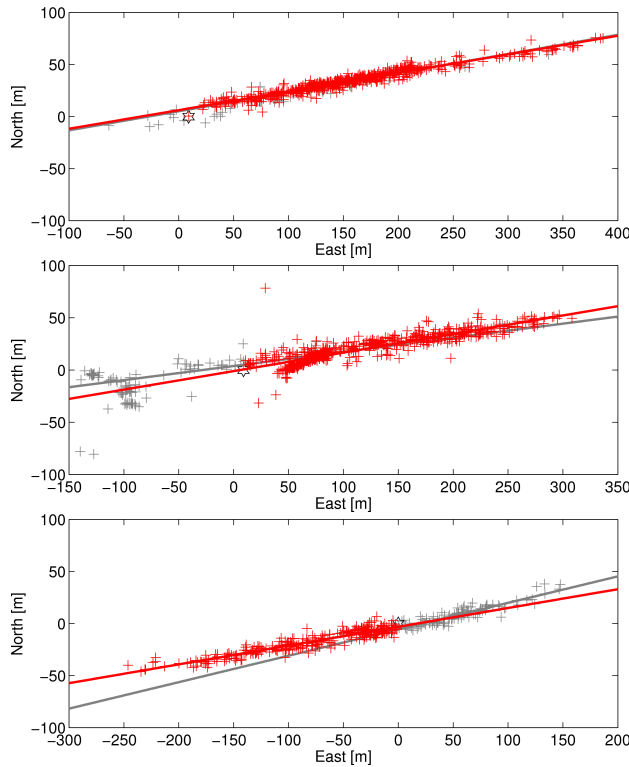


Figure 4.8: Map view of induced microearthquakes during Stage A, Stage B and Stage C treatment (top to bottom). Grey color denotes complete set of located events, red color marks events used in the likelihood modeling. The fracture lines are obtained by linear regression. Epicenters of microearthquakes have been projected to the fracture line for transferring source coordinates from  $(x, y, z)$  to  $(\hat{x}, z)$  system since it is required by the modeling approach.

### Result of Modeling

The modeling of the fracture growth using the likelihood method allows to test the result of the before presented interpretational approach. In a first step, the locations of induced microearthquakes are transferred from  $(x, y, z)$  coordinate system to a new  $(\hat{x}, z)$  system. This is done by calculating hypothetical positions of the microearthquakes along a fracture line which was obtained by linear regression of the original source locations. The corresponding fracture lines are shown in Figure 4.8 for the three Stages A, B and C. The fracture initiation time equals the occurrence time of the first event and only times of continuous injection are considered, which means that no post-injection seismicity is used for modeling. The location errors are set to  $\sigma_x = 10$  and  $\sigma_z = 5$  for all events.

Figure 4.9 illustrates the outcome of modeling  $C_1$ ,  $C_2$  and  $h_f$  for the three individual fractures. The resulting maximum of the log likelihood function (Equation 4.18) yields for the Stage A the parameters  $C_1 = 0.59 [0.05 - 2.18] s/m$  and  $C_2 = 0.26 [0.25 - 0.27] \sqrt{s}/m$ , and for the Stage B  $C_1 = 3.72 [2.5 - 4.95] s/m$  and  $C_2 = 0.31 [0.29 - 0.33] \sqrt{s}/m$ , respectively. For the Stage C, a water treatment, both fracture wings are considered separately. The likelihood based modeling gives for the left wing the estimated parameters  $C_1 = 5.2 [2.03 - 7.99]$

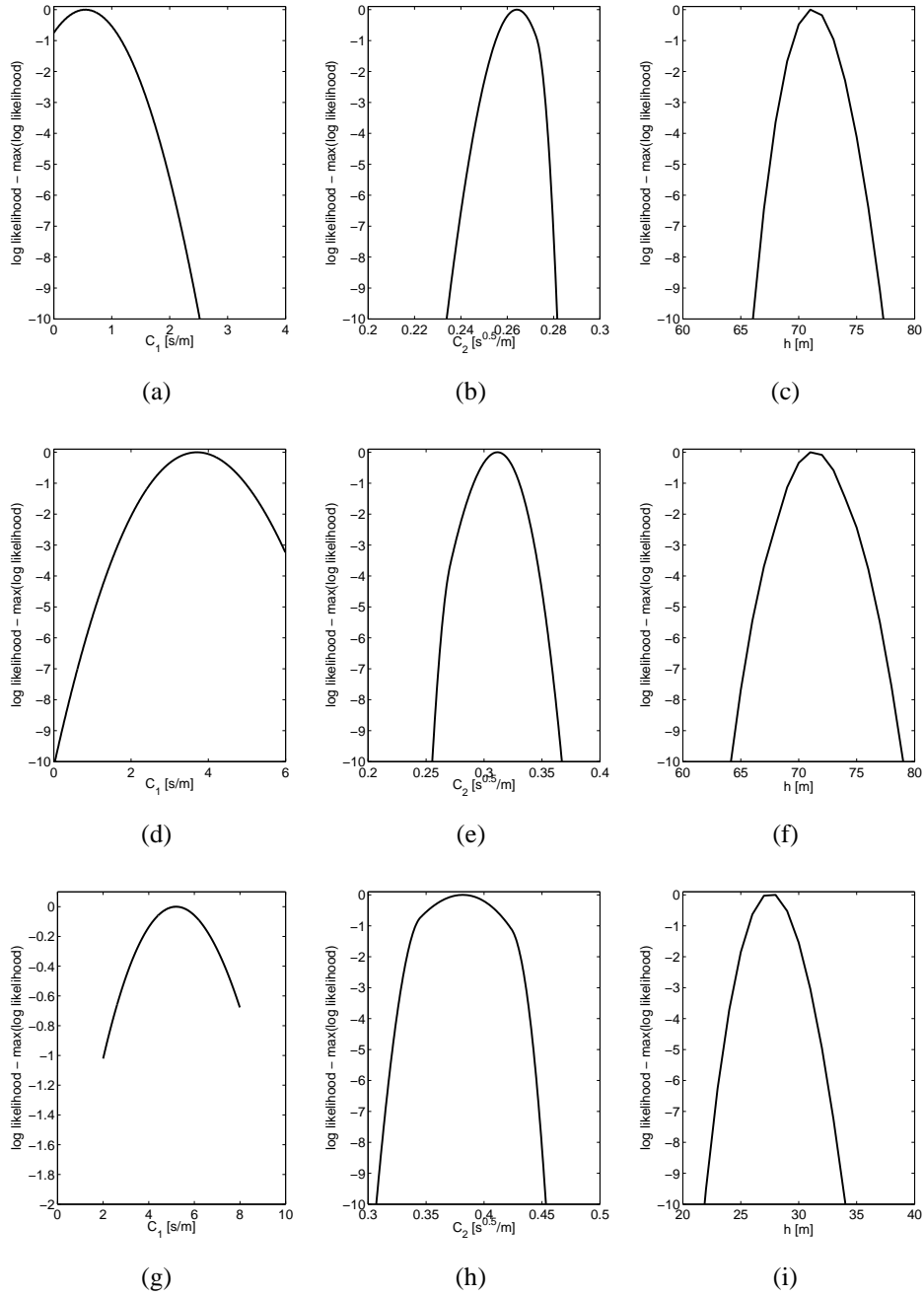


Figure 4.9: Maximum log-likelihood values for the parameter set  $C_1$ ,  $C_2$  and  $h_f$ . Top row: Stage A, middle row: Stage B, and bottom row: Stage C treatment.

Fracture	Width MLE	Width IA	Fluid loss MLE	Fluid loss IA
Stage A	2 mm	2.8 mm	$8.0 \cdot 10^{-5} \text{ m/s}^{1/2}$	$5.2 \cdot 10^{-5} \text{ m/s}^{1/2}$
Stage B	3 mm	3.6 mm	$8.5 \cdot 10^{-5} \text{ m/s}^{1/2}$	$7.7 \cdot 10^{-5} \text{ m/s}^{1/2}$
Stage C	4 mm	3.6 mm	$6.2 \cdot 10^{-5} \text{ m/s}^{1/2}$	$4.6 \cdot 10^{-5} \text{ m/s}^{1/2}$

Table 4.3: Results of maximum likelihood modeling (MLE) in comparison to results obtained by the interpretational approach (IA).

$s/m$  and  $C_2 = 0.38 [0.34 - 0.42] \sqrt{s}/m$ . The obtained parameter set  $C_1$  and  $C_2$  for the three fractures is plotted to the corresponding microseismic event clouds in Figure 4.10. The maximum likelihood fracture heights are 71 m for each of the two gel treatments (Stages A and B), and 28 m for the water treatment (Stage C).

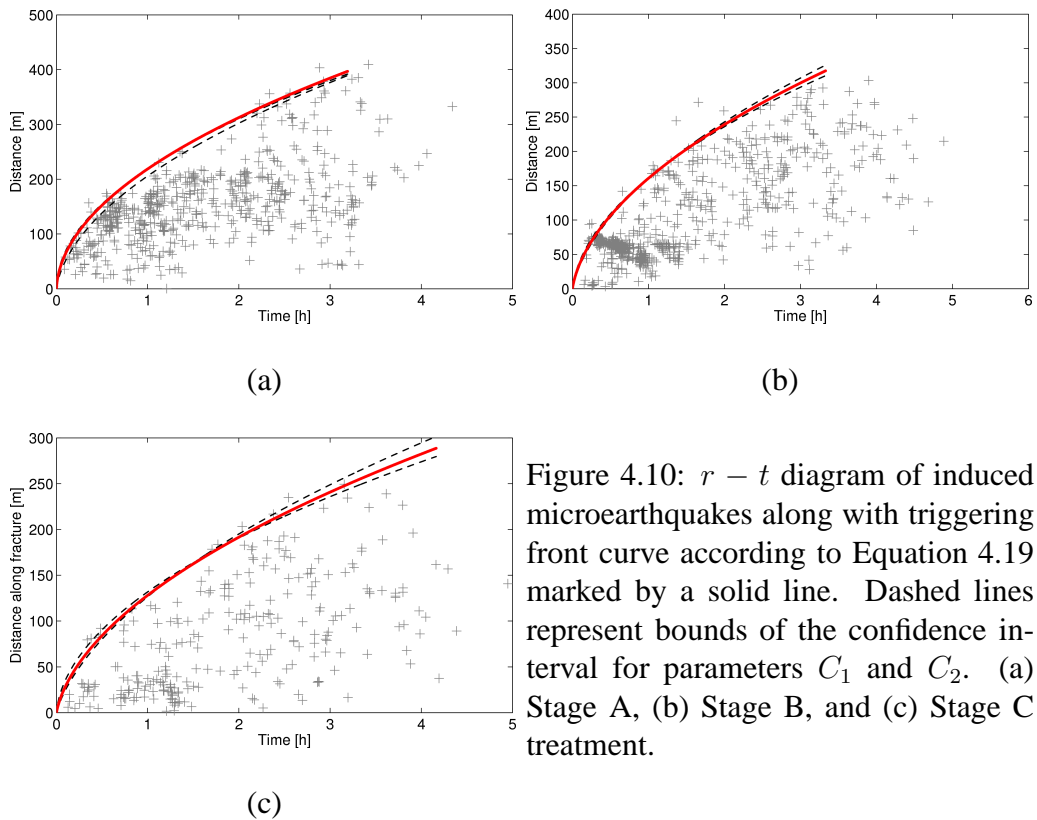


Figure 4.10:  $r - t$  diagram of induced microearthquakes along with triggering front curve according to Equation 4.19 marked by a solid line. Dashed lines represent bounds of the confidence interval for parameters  $C_1$  and  $C_2$ . (a) Stage A, (b) Stage B, and (c) Stage C treatment.

The modeled values  $C_1$ ,  $C_2$  and  $h_f$  can be further interpreted by calculating the average fracture width  $w$  and the fluid-loss coefficient  $C_L$  using the notations given

in Equation (4.19). The resulting width and fluid loss of the corresponding hydraulic fractures are summarized in Table 4.3. A comparison with the estimates obtained using the volume balance principle shows a good coincidence between the two different approaches. This agreement confirms the applicability of the derived interpretational model for single-planar hydraulic fractures.

## 4.6 Fracturing Related Phenomena

### 4.6.1 Flow Pattern Heterogeneities

So far, we have considered envelopes of induced microseismicity in  $r - t$  diagrams, the triggering and the back front. However, the spatio-temporal characteristic of induced microearthquakes also provides information on the influence of flow pattern heterogeneities on the growth of a fracture and its corresponding microseismicity. Two different phenomena, the opening of a pre-existing fracture system and the back-flow of the injected fluid, can be identified in the  $r - t$  diagram of the water treatment Stage E (Figure 4.11(b)). The observations are explained by the following considerations. The treatment fluid flows over a pre-existing, thin aseismic channel to a natural weakness or fractured zone at a distance of about 250 m east of the treatment well (Figure 4.11). The forced fluid is opening a fracture in this zone mainly in a direction away from the treatment well, but also in a direction towards the well. This will be more intuitive by assuming the microearthquake that occurred first in this region to be the location of a secondary injection source (Figure 4.11(a)). Now, representing the induced microearthquakes which belong to this cluster in a separate directional  $r - t$  diagram indicates that the microseismicity, and hence the injected fluid, migrates in both directions from the assumed secondary fluid source (Figure 4.11(c)). Interestingly, a clear intensification of the flow in direction back to the treatment well can be observed after the injection is stopped. The back-flow appears to be generated by some manner of “air balloon” effect. It is caused by an increase of the pressure gradient directed towards the treatment well: zero injection rate and, consequently, a pressure drop at the perforated injection well but remaining high pressures in the fracture. This developing pressure gradient forces the fluid to flow back in the direction of the treatment well.

A slightly different phenomenon can be observed in gel treatment Stage B. Figure 4.12(b) clearly demonstrates that part of the microseismic events migrate also in a direction back to the borehole. Note, that the propagation in backward direction occurs here during the injection period as well as after termination of the injection. These events occur within a fracture off-trend cluster that accounts for about

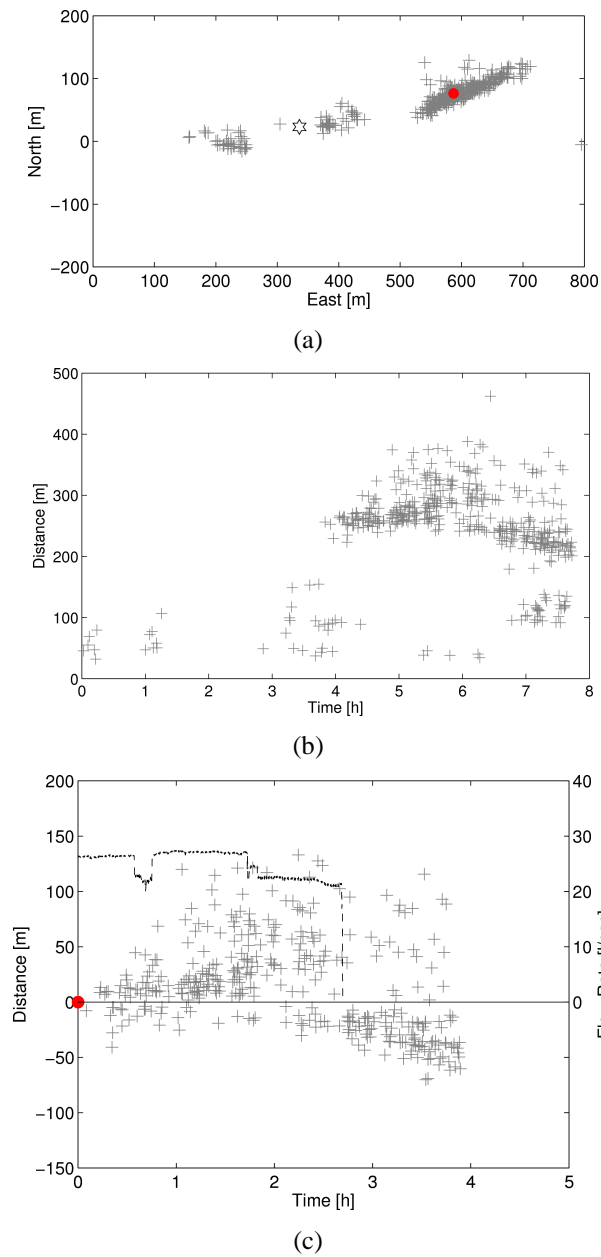


Figure 4.11: (a) Map view of induced microearthquakes in Stage E water treatment. The red point marks the first triggered event within an event cluster in a distance of  $\sim 250m$  east of the injection well (star). (b)  $r-t$  diagram of Stage E seismicity. (c) Directional  $r-t$  diagram of the event cluster, dashed line denotes fluid flow rate. Note, that after shut-in seismicity migrates towards the treatment well.

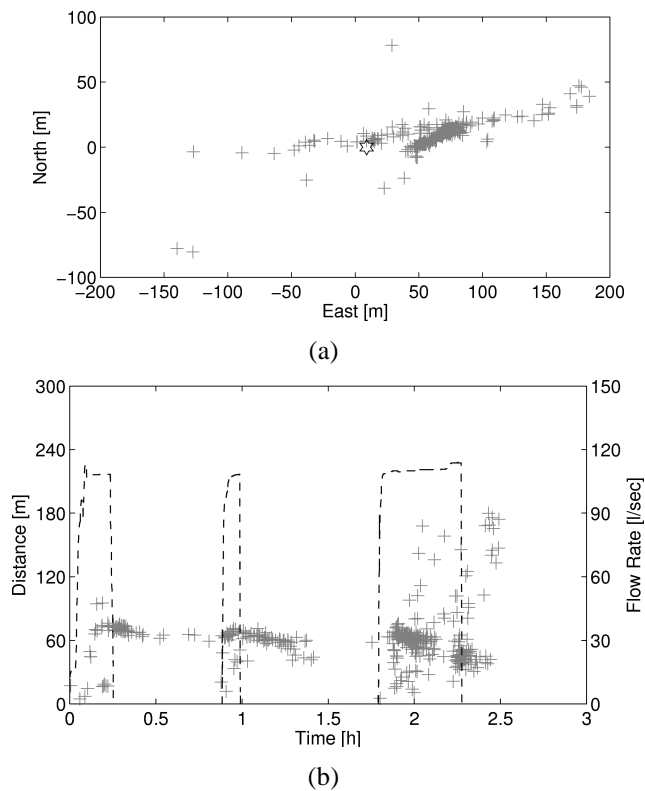


Figure 4.12: (a) Map view of induced microearthquakes in Stage B gel treatment. Shown are the first 3h of the treatment only. (b) Corresponding  $r - t$  diagram, dashed line denotes fluid flow rate. Note, that most of seismicity occurs in a natural fracture system which intersects the hydraulic fracture trajectory. In the  $r - t$  diagram, these events migrate towards the treatment well.

40% of detected events in Stage B (Rutledge et al., 2004). This means that the injected fluid opens a pre-existing fracture which intersects the hydraulic fracture trajectory. Because both Stage E and Stage B treatments were performed in the same sand horizon, the observed characteristics of induced microseismicity likely reflects the influence of a more heterogeneous natural fracture system compared to the targeted sand layers in Stage A and Stage C treatments.

#### 4.6.2 Kaiser Effect Breakdown

Several studies of microseismic and acoustic emission in rocks subjected to cyclic mechanical loading and unloading by applying stress or by borehole fluid injections (Lockner, 1998; Zoback and Harjes, 1997; Zang et al., 2000; Baisch

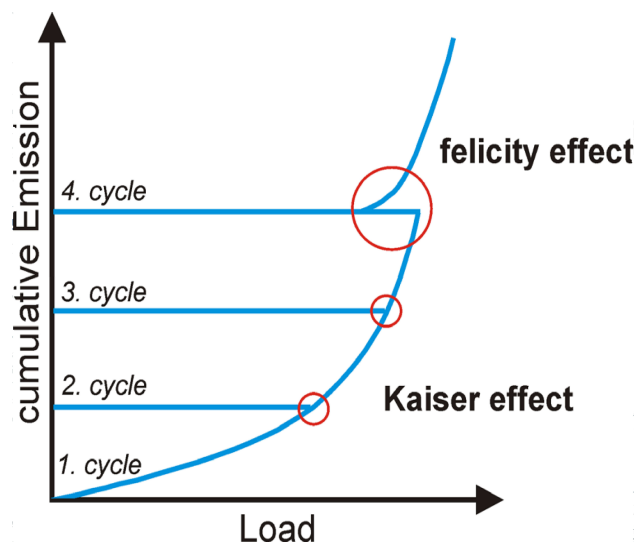


Figure 4.13: Sketch illustrating the principle of the Kaiser effect which is an expression of memorized stress history of rocks or materials in general. If a sample is exposed to a cyclic load, it emits acoustic waves only after the load peak value in preceding cycles is exceeded. A violation or a breakdown of the Kaiser effect is termed felicity effect where acoustic respectively seismic emission appears at a lower load value.

et al., 2002) indicate existence of the Kaiser effect. It can be characterized by the absence of detectable seismic or acoustic emission events while the load imposed on the rock is lower than the previous applied load. As the former peak value of stress is exceeded, the seismic or acoustic emission activity increases dramatically (Figure 4.13). The Kaiser effect was first observed in metals by Kaiser (Kaiser, 1950); investigations in geoscience were first reported in the end of 1970's (Tanimoto et al., 1978; Kurita and Fuji, 1979). Recently, an interesting example of the presence of the Kaiser effect by fluid injections was reported by Baisch et al. (2009). The authors investigated microearthquakes that were induced during a reservoir stimulation in Cooper Basin, Australia, in September 2005. They found that seismic activity starts at several positions at the outer boundary of the seismically active volume of a stimulation in December 2003 (Baisch et al., 2006) and, with ongoing injection, migrates in both directions toward and away from the injection well. In particular, only few microearthquakes are located close to the injection well which is surrounded by large zone of seismic inactivity (see Figure 4 and 5 in Baisch et al. (2009)).

In case of fracturing-induced microseismicity, in particular in the here considered Cotton Valley data set, both violation as well as existence of the Kaiser effect can be identified from the microseismic data. In the following, I will describe the observations and try to give explanations for this phenomenon. At first, the cumulative number of microearthquakes induced during gel treatment Stage A is considered. One can notice from Figure 4.14 that the cumulative event number continuously increases during the first approximately 15 *min* of fluid injection which means during the first injection cycle. In this time period, the bottom hole pressure mainly decreases. Further, the cumulative number of microearthquakes continues its increase during the second injection cycle (time period of injection is approximately 25 *min*, starting at about 35 *min* after begin of the treatment), in spite of the fact that the bottom hole pressure is again mainly decreasing. Note also that the pressure level in this injection cycle, including its peak value, is slightly smaller than in the previous cycle. Finally, the cumulative event number is again increasing immediately with the begin of the third injection cycle (at about 3 *h*) again by a pressure level smaller than the maximum levels reached in the first and second injection cycle. This is in contradiction with the Kaiser effect - the cumulative number of microearthquakes continuously increases during extensive time periods where the bottom hole pressure was lower than the maximum pressures in the previous loading cycle. Very similar features can be seen in the microseismic data of gel treatment Stage B as well as in water treatment Stage C (see Appendix, Figure A.4 and Figure A.5).

Let us now have a closer look to the phenomenon of a lacking Kaiser effect and

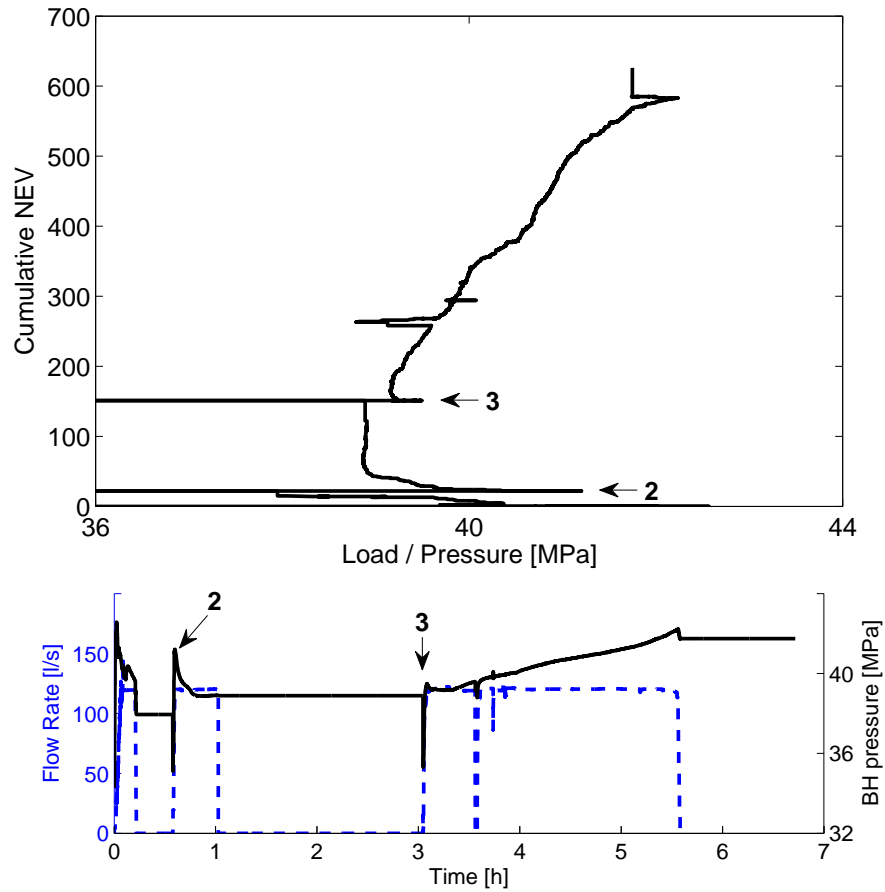
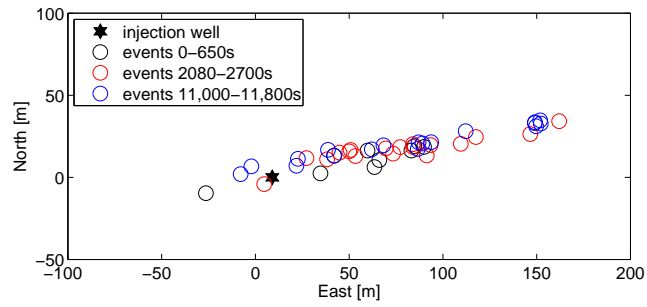


Figure 4.14: (Top) Cumulative number of microearthquakes (NEV) induced in Stage A gel treatment as function of bottom hole pressure. (Bottom) Hydraulic treatment data (dashed line: flow rate, solid line: bottom hole pressure) of Stage A gel treatment. Numbers 2 and 3 show the same time moments in both figures. They mark starting points of an injection cycle.

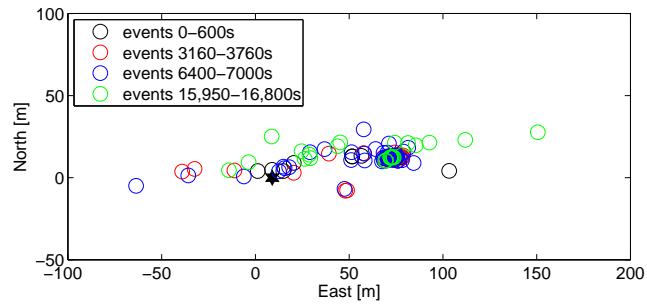
its relation to the growth processes of a hydraulic fracture and to the dynamics of induced microearthquakes. The fracture reopening phases correspond to similar patterns of the pressure behavior: firstly, a quick increase and then a gradual decrease of the bottom hole pressure. Microseismicity still occurs during complete injection cycles. Even more, locations of microearthquakes map very well reopening of the fracture. Figure 4.15 shows horizontal projections of the locations of microseismic events which occurred during opening and reopening phases (that are periods of a quasi-linear with growth). It is evident that microseismicity happens roughly in same places. One can therefore conclude that fracture reopening phases are characterized by the felicity effect, or in other words, by absence of the Kaiser effect. Obviously, Figure 4.15 demonstrates the violation of the Kaiser effect rather on a global level, which means in the hydraulically fractured domain as a whole. Due to a limited precision of event localization (location errors are about 5 – 10 *m*) one can not insist that the Kaiser effect is also violated on a local level, i.e., that locations of events exactly match the same locations where microseismic activity has been already registered in previous loading cycles. However, it is still surprising that there are seismic events activated in different loading cycles and located very closely from each other.

Nevertheless, it is known that the Kaiser effect is also observed by fluid injections (Lockner, 1998; Zang et al., 2000; Backers et al., 2005; Baisch et al., 2009) and in fact, its signatures are present in the Cotton Valley microseismic data as well. Let us consider microearthquakes induced immediately after the stop of an injection cycle. In this situations, microseismicity becomes significantly reduced on long distances from the borehole with ongoing time. However, at the same time microseismicity becomes very improbable on short distances from the borehole. The second effect, which is less obvious, is explained with the concept of back front of induced seismicity (see Chapter 2.4). The existence of the back front is in agreement with the Kaiser effect: Negative pore pressure changes are not triggering microseismicity. As it was shown before, the back front signature is clearly observable in the  $r - t$  diagrams of induced microearthquakes for the three treatments under consideration (see Figure 4.5(e), Figure 4.5(f) and Figure A.3 in Appendix).

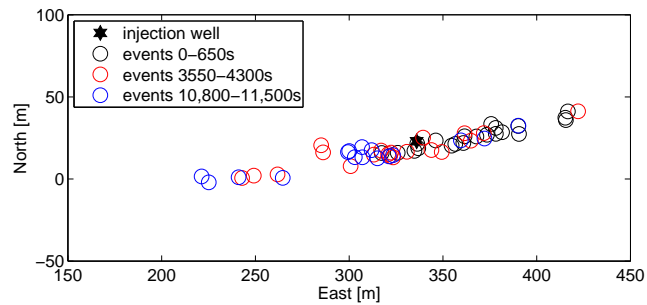
To summarize, the observation results in the conclusion that the Kaiser effect is absent by reopening of a fracture but it is present after stop of a fluid injection. The question arises, how to explain such a contrasting behavior of fracturing-induced microseismicity? The following scheme is proposed. After a stop of an injection cycle the fluid pressure load on the fracture walls gradually vanishes in a slow, quasi-diffusional process as supported by the back front signature of microseis-



(a)



(b)



(c)

Figure 4.15: Plane view of source locations of microearthquakes which occurred during opening/reopening phases of the hydraulic fractures. From top to bottom: Stage A gel treatment, Stage B gel treatment and Stage C water treatment.

micity. Consequently, the fracture surface gradually closes which is assumed to be a mainly aseismic process. During a fluid pressure reload by a following injection cycle reopening of the hydraulic fracture takes place and the fracture surface consequently expands. This reopening is a quick, quasi-linear with time process. The separation of the fracture walls can cause a kind of "rubbing noise" via shear slip events. Such a mechanism is quite identical to mechanisms that are known in material sciences by reopening of tensile defects (Tensi, 2004).

Furthermore, a diffusion-like pressure penetration behind the fracture walls can additionally trigger microearthquakes during the phases of reopening of the fracture. Especially, if the medium is strongly hydraulically heterogeneous then even on a local scale microseismic events can continue to occur in adjacent positions by a cyclic diffusion-like load. In such a situation, the pore pressure perturbation in some part of the rock can further increase although it decreases close to the borehole as indicated by the measurements of bottom hole pressure.

## 4.7 Summary and Conclusions

In this chapter, the focus was on microseismicity which results from hydraulic fracturing. To apply a seismicity based reservoir characterization I have presented an interpretational approach for single-planar ( $1D$ ) hydraulic fractures. One of the fundamental aspects of the proposed approach is the analysis of spatio-temporal dynamics of induced microearthquakes. It is evident from the Cotton Valley data that the space-time diagrams ( $r - t$  diagram) show signatures of fracture volume growth, loss of treatment fluid, and diffusion of injection induced pore pressure perturbations within the fracture and from the fracture walls into the surrounding formation. The interpretation of envelopes of the spatio-temporal distribution of fracturing-induced seismicity allows to determine geometrical parameters as well as hydraulic characteristics of the fracture. By assuming a conservation of the injected fluid volume, fluid transport properties of the virgin reservoir can additionally be estimated. The interpretational approach uses the following work flow. Firstly, the volume of the newly created hydraulic fracture can be estimated from the induced microseismicity. Next, the volume of treatment fluid which was lost into formation by filtration through the fracture walls can be computed. Knowing the fluid loss, one can define the virgin reservoir permeability. Additionally, an apparent diffusivity describing the fluid leakage process can be calculated and compared with the microseismic data for a rough quality control. Finally, the back front of induced seismicity gives an estimate of fracture permeability. I have applied the proposed approach to microearthquakes induced by several stages of hydraulic fracturing in a tight-gas reservoir. A comparison of microseismicity from gel and water treatments shows that the

fracturing resulted in similar fracture characteristics. The ratio of new fracture volume to the total injected volume is nearly identical in the three considered treatments. I therefore conclude that the fracture growth process is decoupled from the type of treatment. This is confirmed by comparing the released seismic energy as function of the cumulative injected volume. Furthermore, it is evident that permeability of the fractures is influenced by the amount of pumped proppant which keeps the fracture open after shut-in of the injection. To verify the results of fracture geometry and fluid loss I have performed a modeling of the fracture propagation using the maximum likelihood method. It yields fracture widths and fluid-loss coefficients which well agree with before obtained findings. Hence the applicability of the interpretational approach is supported by the independently performed maximum likelihood modeling.

In the last part of this chapter, I have briefly discussed some phenomena which are observed in the Cotton Valley data set. On the one hand, it concerns heterogenous flow patterns whose signatures are also present in the dynamics of microseismicity. These signatures provide information about interactions of the pressurized fluid with the pre-existing fracture system. The heterogeneities can be explained by the orientation of pre-existing natural fractures in respect to the hydraulic fracture trajectory, and by pressure gradients within the fracture after termination of the injection.

On the other hand, a breakdown of the Kaiser effect is found for tensile in-situ hydraulic fracturing experiments. Such experiments with a cyclic load (fluid injection) and simultaneous microseismic monitoring are quite unique which is possibly a reason why such a phenomenon has not been reported before. Interestingly, such a violation of the Kaiser effect for tensile fracturing due to hydraulic forcing on rocks is similar to the violation of the Kaiser effect in the case of shear faulting by seismogenic processes, such as subduction earthquakes. Large patches of the Wadati-Benioff zone indeed stay seismically active before and after the occurrence of big earthquakes during many cycles of corresponding tectonical loading. This analogy demonstrates that a violation of the Kaiser effect might indicate creation and further development of new contacting surfaces in rock like fractures, fissures and joints, and thus, it is possibly a common feature of active faulting processes.

## **Chapter 5**

# **Magnitudes of Fluid-Induced Seismicity**

Fluid-induced microearthquakes are to some extent induced by hydraulic fracturing and hydraulic stimulation operations. The seismic activity related to these injections had occasionally not been considered as a hazard. The hydraulic stimulation of the Basel geothermal reservoir in 2006, however, caused several significant events which were felt by the community (Majer et al., 2007; Häring et al., 2008). The occurrence of these microearthquakes has led to the awareness that a more in-depth knowledge of seismic risk associated with fluid injections is required. Understanding of the characteristics of earthquake magnitudes is the starting point for an evaluation and finally a mitigation of potential seismic risk.

In this chapter, I will introduce a statistical model which describes the distribution of magnitudes of fluid-induced seismicity. Since the cumulative injective fluid mass can be considered as a key parameter, it is independent of non-linear fluid-rock interactions such as a pressure-dependent permeability. It means that the presented formalism is valid for seismicity resulting from hydraulic fracturing as well as from hydraulic stimulation. Moreover, it gives answers to the controlling factors of the magnitude distribution and how one can reduce the probability of inducing microearthquakes characterized by a significant magnitude.

## 5.1 Theoretical Model of Magnitude Distribution of Fluid-Induced Seismicity

The fundamental ideas that resulted in the theoretical concept proposed by Shapiro et al. (2007) can be divided into two parts. First, the probability of a fluid-induced microearthquake having a magnitude larger than a given magnitude is an increasing function of the overall event number. Secondly, the authors hypothesize that magnitudes of fluid-induced seismicity follow a Gutenberg-Richter statistics. It means that the frequency-magnitude distribution is in accordance with the Gutenberg-Richter scaling law (Gutenberg and Richter, 1954). In the following, I will comment on these ideas and their consequences for the statistics of magnitude distribution of fluid-induced microearthquakes.

### Cumulative number of induced microearthquakes

Let me begin with revisiting the statistical model for describing the occurrence of seismicity during fluid injections which was introduced in Chapter 3. The cumulative number of microearthquakes resulting from a fluid injection can be obtained from this model. For simplicity, a point-like injection pressure source of constant strength is firstly considered. It is assumed that the hydraulic diffusivity is homogeneously distributed in an infinite, permeable, porous medium. The injection-induced pressure relaxation alters the pore pressure in the pore space and hence modifies the effective normal stress. It is further assumed that a random set of non-interacting, pre-existing fractures with volume concentration  $\zeta$  is statistically homogeneous distributed in the medium. Each of the fractures is characterized by a critical pore pressure value necessary for the occurrence of a slip event along the fracture in accordance with the Coulomb failure criterion (Scholz, 2002). The critical pore pressure are randomly selected from a uniform distribution between a minimum value,  $C_{min}$ , and a maximum value,  $C_{max}$ .  $C_{min}$  and  $C_{max}$  address most unstable and most stable fractures, respectively. A fracture location  $\vec{r} = (x, y, z)$  (and defined by its distance  $r = \sqrt{x^2 + y^2 + z^2}$  to the source point) will now become the hypocenter of a microearthquake with occurrence time  $t_0$ , if the pore pressure perturbation  $p(r, t)$  exceeds the local value of critical pressure at time  $t_0$ . It is assumed that once a microearthquake occurred at a certain fracture location, then no further earthquakes are possible at this position. This condition is due to the observation that recharging of fractures to a near-critical state takes longer than the diffusion-like relaxation of a pore pressure perturbation (Shapiro et al., 2007).

These preliminary considerations lead to the following. The probability

$P(Ev, \vec{r}, t)$  that an earthquake occurs at a given fracture location  $\vec{r}$  and until the time  $t$  is equal to the probability that the critical pore pressure at position  $\vec{r}$  is lower than or equal to the maximum pore pressure perturbation reached at this position until time  $t$ . It means, the probability is  $P(C(\vec{r}) \leq \max(p(r, t)))$ . With the condition of non-decreasing injection pressures one obtains:

$$P(Ev, \vec{r}, t) = \int_{C_{min}}^{p(r,t)} f(C) dC, \quad (5.1)$$

where  $f(C)$  is the probability density function (*PDF*) of critical pressures  $C(\vec{r})$  of pre-existing fractures. If a uniformly distributed criticality field is assumed, then the *PDF* of critical pressures is given as:

$$f(C) = \frac{1}{C_{max} - C_{min}} \approx \frac{1}{C_{max}}. \quad (5.2)$$

The latter, approximated term in this equation takes into account the observation that  $C_{max}$  is generally several orders of magnitude larger than  $C_{min}$  which hence becomes vanishing small. With the assumption that the maximum criticality is larger than the pore pressure perturbation (excluding the very near borehole area) and the minimum criticality equals zero (the so-called reference case (Langenbruch and Shapiro, 2010)), then Equation (5.1) yields for the earthquake probability a direct proportionality to the pore pressure perturbation:

$$P(Ev, \vec{r}, t) = \frac{p(r, t)}{C_{max}} = \frac{q_0}{4\pi D r C_{max}} \cdot \text{erfc} \left( \frac{r}{\sqrt{4Dt}} \right). \quad (5.3)$$

The total number of microearthquakes  $N(t)$  induced in the time interval  $(0, t)$  can now be obtained by multiplying the event probability with the fracture volume concentration  $\zeta$ , and spatial integration of the product:

$$\begin{aligned} N(t) &= \frac{q_0 \zeta}{4\pi D C_{max}} \cdot \int_V \frac{1}{r} \cdot \text{erfc} \left( \frac{r}{\sqrt{4Dt}} \right) d^3r \\ &= \frac{q_0 \zeta}{D C_{max}} \cdot \int_0^\infty r \cdot \text{erfc} \left( \frac{r}{\sqrt{4Dt}} \right) dr \\ &= \frac{q_0 \zeta t}{C_{max}}. \end{aligned} \quad (5.4)$$

One can notice from this equation that the cumulative number of fluid-induced microearthquakes grows linearly with time with constant rate  $q_0 = 4\pi D a_0 p_0$  (see Chapter 3.2.1, and Rothert and Shapiro, 2007) in case of an injection with constant injection pressure  $p_0$ .

If the injection pressure during a fluid injection is not constant over time but linearly increasing with time, then Equation (5.4) changes to (see also Chapter 3.2.2 and Chapter 3.2.3, assuming  $q_0 = 0$ ):

$$N(t) = \frac{q_t \zeta t^2}{C_{max}}, \quad (5.5)$$

with  $q_t$  being a constant rate of source strength increase during injection. Note that in both cases, that are the condition of constant as well as the condition of non-constant injection pressures, possible nonlinear fluid-rock interactions are not taken into consideration. A more general formalism has therefore been derived by Shapiro and Dinske (2009b) which is valid for any kind of nonlinearities in the interdependence of injected fluid and rock mass. It uses the fluid continuity equation which is an expression of the conservation of fluid mass (see Chapter 2.3, Equation (2.9)). With this principle, it can be found that the number of microearthquakes  $N(t)$  induced during a fluid injection is proportional to the injected fluid mass  $m_c(t)$ , respectively proportional to the injected fluid volume  $V_I$  if a constant fluid density  $\rho$  is assumed (Shapiro and Dinske, 2009b):

$$N(t) = \frac{m_c(t) \zeta}{C_{max} \rho S} = \frac{V_I(t) \zeta}{C_{max} S}, \quad (5.6)$$

where  $S = \alpha^2 \left( \frac{1}{M_{dry}} + \frac{1}{K_s - K_{dry}} \right) + \phi \left( \frac{1}{K_f} - \frac{1}{K_s} \right)$  is a poroelastic compliance defined by the bulk moduli of dry rock, grain material and fluid phase,  $K_{dry}$ ,  $K_s$ ,  $K_f$ , the P-wave modulus of dry rock  $M_{dry}$ , porosity  $\phi$ , and Biot coefficient  $\alpha$ .

### Magnitudes statistics of fluid-induced microearthquakes

The question arises, how one can now specify the magnitude distribution of induced microearthquakes. To determine the probability of one event having a magnitude larger than or equal to a given one during the time interval  $(0, t)$ ,  $P(Ev, M \geq M_0, t)$ , it is supposed that magnitudes of fluid-induced seismicity follow a Gutenberg-Richter type statistics constant in time. It means that the frequency-magnitude distribution of induced microearthquakes is in accordance with the Gutenberg-Richter scaling law (Gutenberg and Richter, 1954). It relates the magnitude and the number of earthquakes of at least that magnitude in any given region and time period. Precisely, the logarithm of number of earthquakes having a magnitude larger than magnitude  $M_0$  is equal to  $a - bM_0$  where  $a$  and  $b$  are constants. The  $a$ -value describes the earthquake productivity whereas the  $b$ -value is the ratio of small to large events. This assumptions provides the following equation system. The product of the cumulative number of microearthquakes (Equations (5.4), (5.5), and (5.6)) with the probability  $P(Ev, M \geq M_0, t)$  yields

the cumulative number of events with a magnitude larger than or equal to a given magnitude  $M_0$  (Shapiro et al., 2007):

$$N_{M \geq M_0}(t) = P(Ev, M \geq M_0, t) \cdot N(t). \quad (5.7)$$

Introducing a Gutenberg-Richter type statistics, that is:

$$P(Ev, M \geq M_0, t) = 10^{a-bM_0}, \quad (5.8)$$

results in the following expressions:

$$\text{for constant source strength: } N_{M \geq M_0}(t) = \frac{q_0 \zeta t}{C_{max}} \cdot 10^{a-bM_0}, \quad (5.9)$$

$$\text{for increasing source strength: } N_{M \geq M_0}(t) = \frac{q_t \zeta t^2}{C_{max}} \cdot 10^{a-bM_0}, \quad (5.10)$$

$$\text{for injected fluid volume: } N_{M \geq M_0}(t) = \frac{V_I(t) \zeta}{C_{max} S} \cdot 10^{a-bM_0}, \quad (5.11)$$

respectively, in logarithmic scale:

$$\log N_{M \geq M_0}(t) = \log \left( \frac{q_0 \zeta}{C_{max}} \right) + \log t + a - b M_0, \quad (5.12)$$

$$\log N_{M \geq M_0}(t) = \log \left( \frac{q_t \zeta}{C_{max}} \right) + 2 \log t + a - b M_0, \quad (5.13)$$

$$\log N_{M \geq M_0}(t) = \log \left( \frac{V_I(t) \zeta}{C_{max} S} \right) + a - b M_0. \quad (5.14)$$

The ratio  $\frac{C_{max}}{\zeta}$  has been introduced as a new quantity, the tectonic potential  $F_t$  (Shapiro et al., 2007). It is defined by two seismotectonic parameters of an injection site. One of the parameters is the maximum criticality  $C_{max}$  which is the upper limit of critical pore pressures of pre-existing fractures. The second one is the volume concentration  $\zeta$  of pre-existing fractures. The tectonic potential has critical implications for the microseismic activity due to an injection. If, for instance, injection flow rate and poroelastic compliance are assumed to be equal at two injection sites but the locations are characterized by a different tectonic potential, then the location with a lower tectonic potential will experience a higher rate of seismicity. It means that the larger the tectonic potential the more efforts are necessary to induce microseismicity.

The Equations (5.12) - (5.14) describe the distribution of magnitudes of fluid-induced seismicity. They also clarify which parameters control the statistics of magnitudes. Let me therefore briefly discuss the significance of the result.

On the one hand, the presented equations allow for specifying the evolution and distribution of earthquake magnitudes by fluid injections. One can notice that the probability of inducing a microearthquake with a significant magnitude increases with injection time and with injection source strength (injection pressures). In volume domain, this occurrence probability increases with injected fluid volume (cumulative fluid mass). The cumulative number of earthquakes with a magnitude larger than or equal to a given magnitude and the injection duration respectively the cumulative injected fluid volume are linearly related in double logarithmic scale. For the condition of constant source strength, the proportionality factor between quantities  $\log N_{M \geq M_0}(t)$  and  $\log t$  is equal to one, whereas it is equal to two for the condition of linearly increasing source strength. If the statistics of magnitudes is considered in volume domain, then the proportionality coefficient is always equal to one. It is also evident from Equations (5.12) - (5.14) that curves of function  $\log N_{M \geq M_0}(t)$  for different magnitudes  $M_0$  are parallel in a bilogarithmic plot.

Equations (5.12) - (5.14) also provide an additional method to determine the  $b$ -value. Assuming that the logarithm of cumulative numbers of earthquakes with a magnitude larger than a given magnitude are considered for two arbitrary magnitudes  $M_i$  and  $M_{i+1}$ . Application of either Equation (5.12), Equation (5.13) or Equation (5.14) gives the following formulation for the  $b$ -value:

$$\begin{aligned} \log N_{M \geq M_i}(t) + b M_i &= \log N_{M \geq M_{i+1}}(t) + b M_{i+1} & (5.15) \\ \log N_{M \geq M_i}(t) - \log N_{M \geq M_{i+1}}(t) &= b M_{i+1} - b M_i \\ b &= \frac{\log N_{M \geq M_i}(t) - \log N_{M \geq M_{i+1}}(t)}{M_{i+1} - M_i}. \end{aligned}$$

On the other hand, the parameters that define the size and distribution of earthquakes magnitudes by fluid injections can be identified from Equations (5.12) - (5.14). As mentioned before, injection engineering parameters, such as injection duration, injection pressures, or injection fluid volume, are one part of magnitude-controlling factors. The second group of parameters are site-specific characteristics of the reservoir-building rock and fracture system. Precisely, these are seismotectonic parameters, such as Gutenberg-Richter  $a$ - and  $b$ -value, and the tectonic potential  $F_t$ . They also include hydraulic diffusivity (via  $q_0$  and  $q_t$ ) or the poroelastic compliance. For the assessment of seismic risk resulting from a fluid injection knowledge of the site-specific seismotectonic parameters is required. It can be achieved by estimating these quantities from a short-term fluid injection test prior to a long-term injection of large fluid volumes.

## 5.2 Magnitude Distributions of Basel and Cotton Valley Data Catalogs

In the following, I will illustrate the before described considerations and the derived formalism for two case studies. Fluid-induced microseismicity from the Basel geothermal reservoir stimulation and from hydraulic fracturing in the Cotton Valley hydrocarbon reservoir are presented.

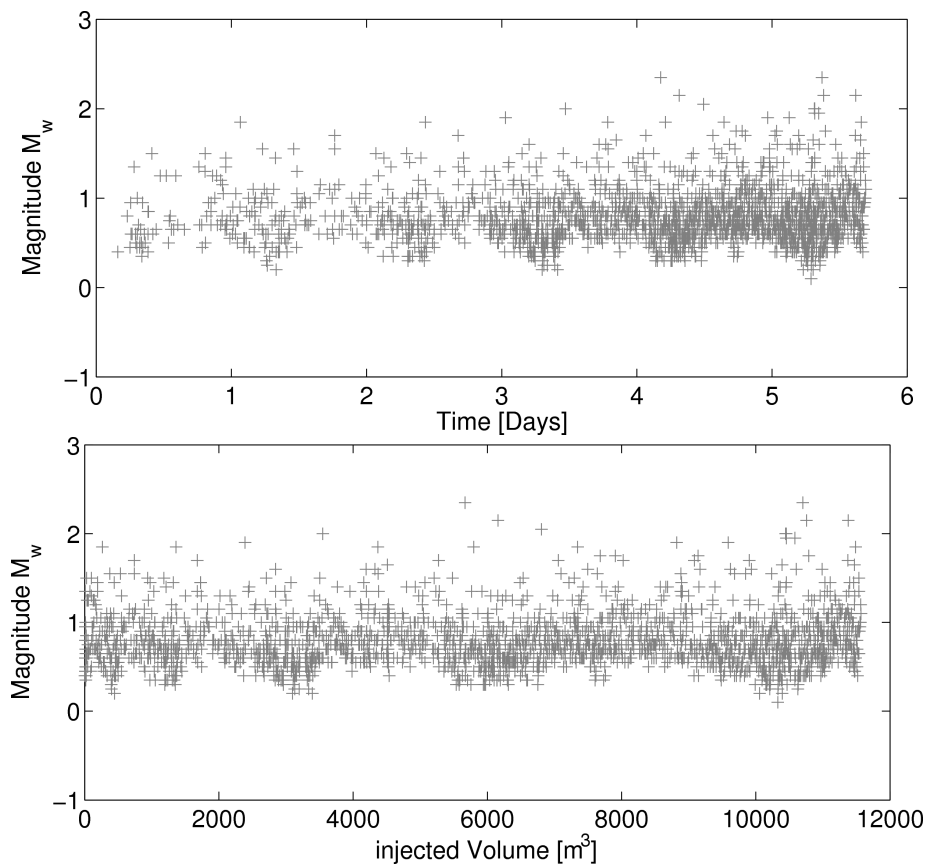


Figure 5.1: Distribution of moment magnitudes of microearthquakes induced during injection in the Basel geothermal reservoir as function of time (top) and as function of cumulative injected fluid volume (bottom). Note that for non-constant increasing fluid flow rates the observed heterogeneous distribution of magnitudes in time domain becomes homogeneous if considered in volume domain.

The temporal evolution of moment magnitudes of induced microearthquakes is shown in Figure 5.1. If earthquake magnitudes are plotted as function of time, then they are heterogeneously distributed (Fig. 5.1(top)). This heterogeneity is due to the applied non-constant injection flow rate. The distribution becomes more homogeneous, however, if the injected fluid volume is considered (Fig. 5.1(bottom)). This homogenization is supported by Equation (5.6) which states that the number of microearthquakes increases proportional with the injected fluid volume.

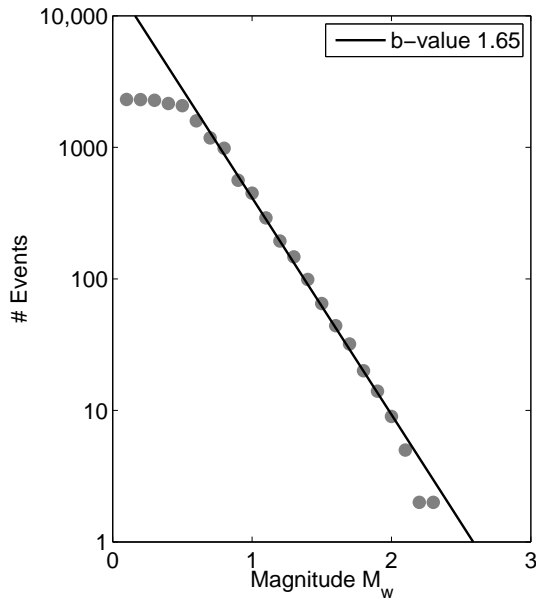


Figure 5.2: Frequency-magnitude distribution of microearthquakes induced during injection in the Basel geothermal reservoir. The fluid-induced seismicity clearly obeys a Gutenberg-Richter statistics. Gutenberg-Richter  $b$ -value is 1.65 (obtained by linear regression).

Figure 5.2 shows the frequency-magnitude distribution of Basel seismicity. The logarithm of the number of events having a magnitude  $M$  larger than or equal to a given magnitude  $M_0$  is linearly proportional to the given magnitude. Thus, it confirms the assumption that fluid-induced seismicity obeys the Gutenberg-Richter scaling law, that is,  $\log N_{M \geq M_0} = a - b M_0$ . Interestingly, the  $b$ -value of Gutenberg-Richter is  $\sim 1.65$  and hence higher than typical  $b$ -values of natural seismicity which are of the order of 1.0. Compared to natural seismicity, it means that larger magnitude earthquakes are underrepresented in case of the hydraulic stimulation in Basel. To study whether the  $b$ -value is constant during injection, the frequency-magnitude distribution is evaluated for several time steps of the injection period. If the frequency-magnitude distribution is plotted for each consecutive  $1000 \text{ m}^3$  of injected fluid separately, then temporal changes of the statistical magnitude distribution become evident (Figure 5.3(left)). In this case, the  $b$ -value of Gutenberg-Richter is highest during injection interval  $3000 - 4000 \text{ m}^3$  ( $b \approx 2$ ) and lowest for seismicity occurring during the last injection interval  $10,000 - 11,000 \text{ m}^3$  ( $b = 1.2$ ). It is a reasonable observation since larger magnitude earthquakes increasingly occurred closer to the end of

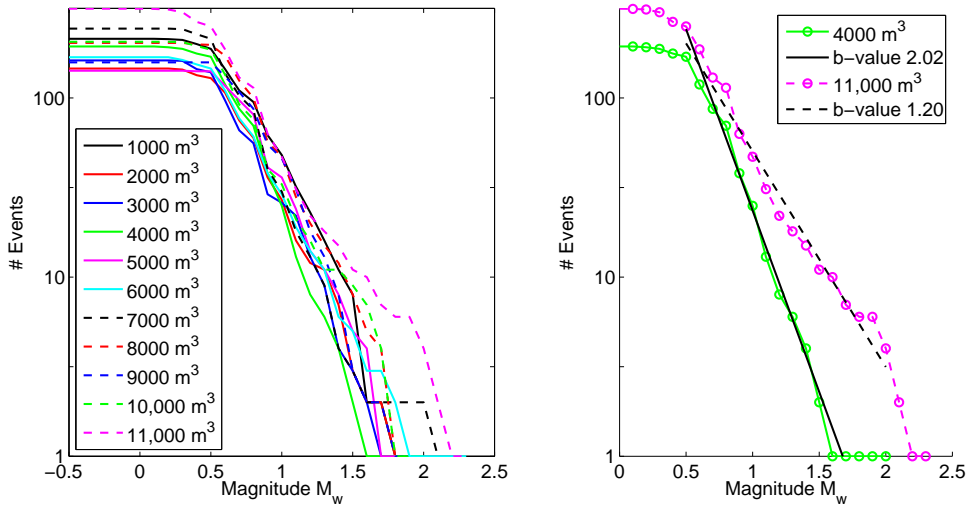


Figure 5.3: (Left) Frequency-magnitude distributions of microearthquakes induced during injection in the Basel geothermal reservoir plotted for differentially injected fluid volume. Changes in the magnitude distribution with injected volume are obvious. (Right) Estimation of highest and lowest  $b$ -value in case of differential analysis of frequency-magnitude distribution.

injection. An explanation for the observed decreasing  $b$ -value over time could be the increasingly stimulated reservoir volume allowing for shear slip along larger fracture planes.

Equation (5.13) predicts a linear relation with a constant proportionality factor two for the logarithm of the number of events having magnitude  $M$  larger than or equal to a given magnitude  $M_0$  and the logarithm of injection time  $t$ . Such a bilogarithmic diagram is illustrated in Figure 5.4. The prediction of the equation is in accordance with the observations from Basel. If the analysis is considered in the volume domain, then the relation between  $\log(N_{M \geq M_0})$  and  $\log(V_I)$  is satisfied by a proportionality factor one (compare with Equation (5.14)).

The magnitudes of microseismicity induced in Cotton Valley are evaluated in the same way. Here the idea is to show that the characteristics of magnitude distribution of fracturing-induced seismicity are identical to the one of stimulation-induced seismicity. This similarity would confirm the global validity of the derived concept for any kind of fluid-induced seismicity independent of the type of fluid-rock interaction. The temporal evolution of microearthquakes moment magnitudes induced in two gel treatments, Stage A and Stage B, and

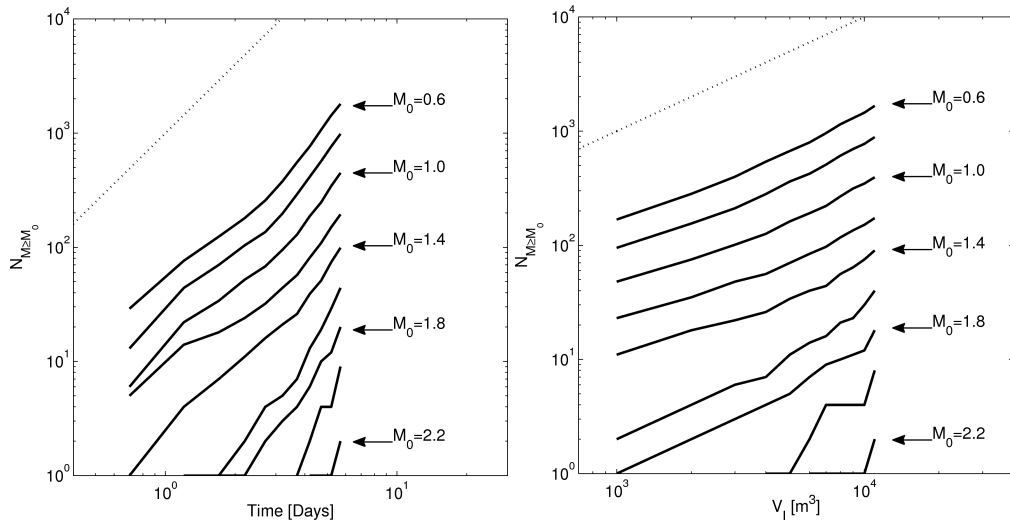


Figure 5.4: Cumulative number of microearthquakes having a magnitude  $M$  larger than or equal to magnitude  $M_0$  ( $N_{M \geq M_0}$ ) induced during injection as function of time (left) and as function of cumulative injected fluid volume (right) in double logarithmic scale. Dotted line is shown for convenience and has slope two (time domain) and slope one (volume domain) illustrating the linear proportionality between the two quantities in double logarithmic scale.

one water treatment, Stage C, are presented in Figure 5.5. The treatments were performed using constant injection flow rates resulting in nearly constant injection pressures. Therefore the three magnitudes distributions are only shown in time domain.

In the following, only microearthquakes that were induced during the main treatments of the three stages (see hydraulic treatment data in Chapter 4.4, Fig. 4.4, and Appendix, Fig. A.2) are considered. The frequency-magnitude distributions of microearthquakes are shown in Figure 5.6(left). One can clearly notice from the figure that the distributions obey the Gutenberg-Richter scaling law, but the  $b$ -values are higher in the case of hydraulic fracturing compared to hydraulic stimulation. Here they are of the order of  $b = 2.7$  (gel treatment Stage A),  $b = 2.2$  (gel treatment Stage B) and  $b = 4.6$  (water treatment Stage C). These high values of  $b$  reflect the almost complete absence of larger events. Additionally, magnitudes of fracturing-induced seismicity tend to be limited to a narrow band.

Finally, bilogarithmic plots of the cumulative number of events having magnitude  $M$  larger than or equal to a given magnitude  $M_0$  as functions of injection time  $t$  for

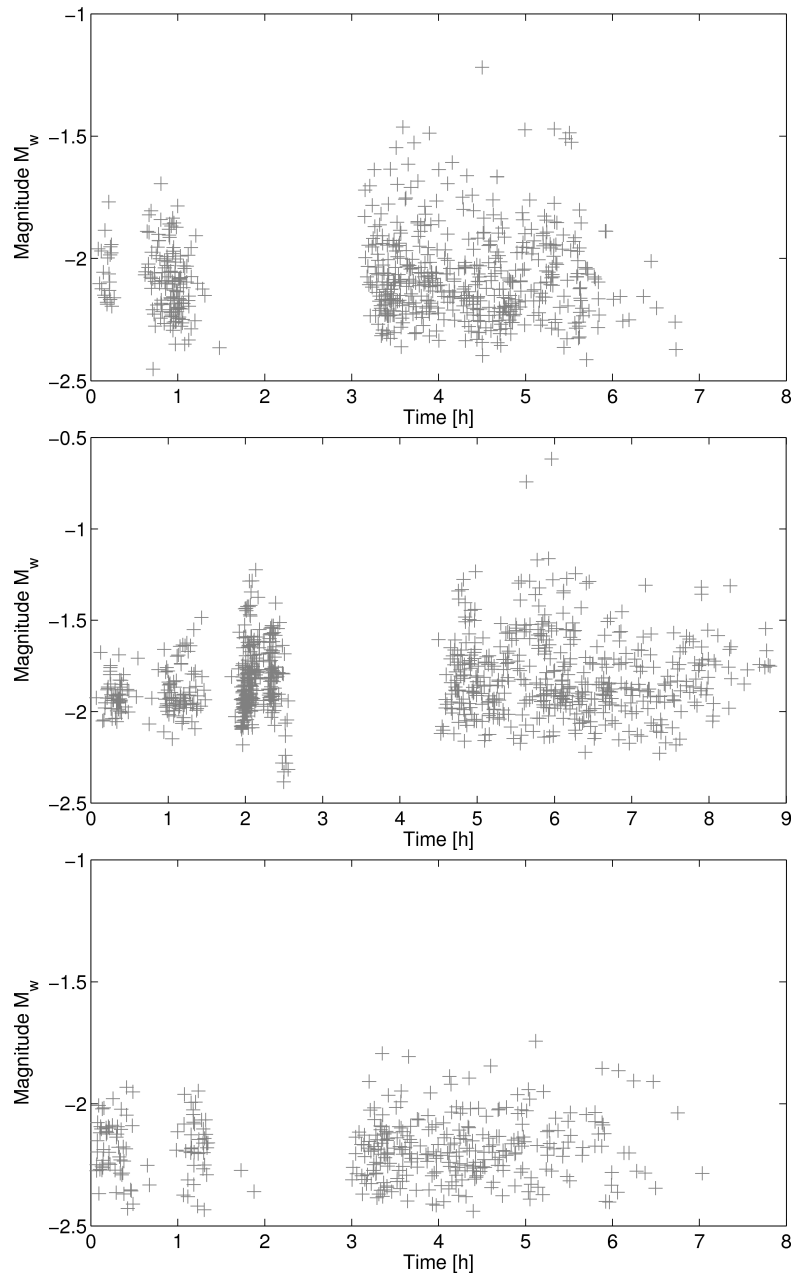


Figure 5.5: Distribution of moment magnitudes of microearthquakes induced during hydraulic fracturing in Carthage Cotton Valley gas reservoir as function of time. (Top) gel treatment Stage A, (middle) gel treatment Stage B, (bottom) water treatment Stage C.

the three treatment stages are presented in Figure 5.6(right). In double logarithmic scale, both quantities obey the predicted linear relation with a proportionality factor one in accordance with Equation (5.12) (*after 20 – 30 min*).

### 5.3 Summary and Conclusions

In this chapter, the focus was the evaluation of size and distribution of earthquake magnitudes resulting from fluid injections. I have introduced a model for describing the statistical distribution of magnitudes. It is valid for co-injection seismicity induced during time periods of non-decreasing source strength. The model is based on two main assumptions. First, the probability of a fluid-induced microearthquake having a magnitude larger than or equal to a given magnitude is an increasing function of the total number of induced microearthquakes. Second, the frequency distribution of magnitudes of fluid-induced seismicity follows the Gutenberg-Richter scaling law. Using these assumptions, a formalism has been derived. On the one hand, it well explains the observations from injection experiments. Furthermore, this formalism allows to distinguish the controlling parameters of magnitudes of fluid-induced microearthquakes. Although I have presented this formalism for the conditions of linear diffusion, constant and linearly increasing injection source pressures, a more general formulation is provided if the cumulative injected fluid mass / fluid volume is considered. The formalism is then independent of possible non-linearities in the interaction of the injected fluid with the reservoir rock (such as in case of pressure-dependent permeability).

Identifying the parameters that define the magnitude and its frequency is a key point for evaluating the seismic risk by fluid injections. Among the injected fluid mass, other parameters that control the magnitude distribution of fluid-induced seismicity are of seismotectonic nature. It means that those parameters are site-specific. They include Gutenberg-Richter  $a$ - and  $b$ -value as well as the tectonic potential which is defined by characteristics of pre-existing fractures. It expresses the ratio of the maximum of critical pressures over the fracture volume concentration. By comparing the magnitude distributions for two different injection locations, the following conclusions can be drawn. Hydrocarbon reservoirs, particularly the Cotton Valley tight-gas reservoir, are characterized by high  $b$ -values. It means, also in consideration of the small fluid volume required in fracturing operations, that microearthquakes with a significant magnitude are less likely to occur. However, it likewise means that a seismic monitoring system at such locations has to have a high level of sensitivity in order to detect the induced microearthquakes and hence to capture as much information as

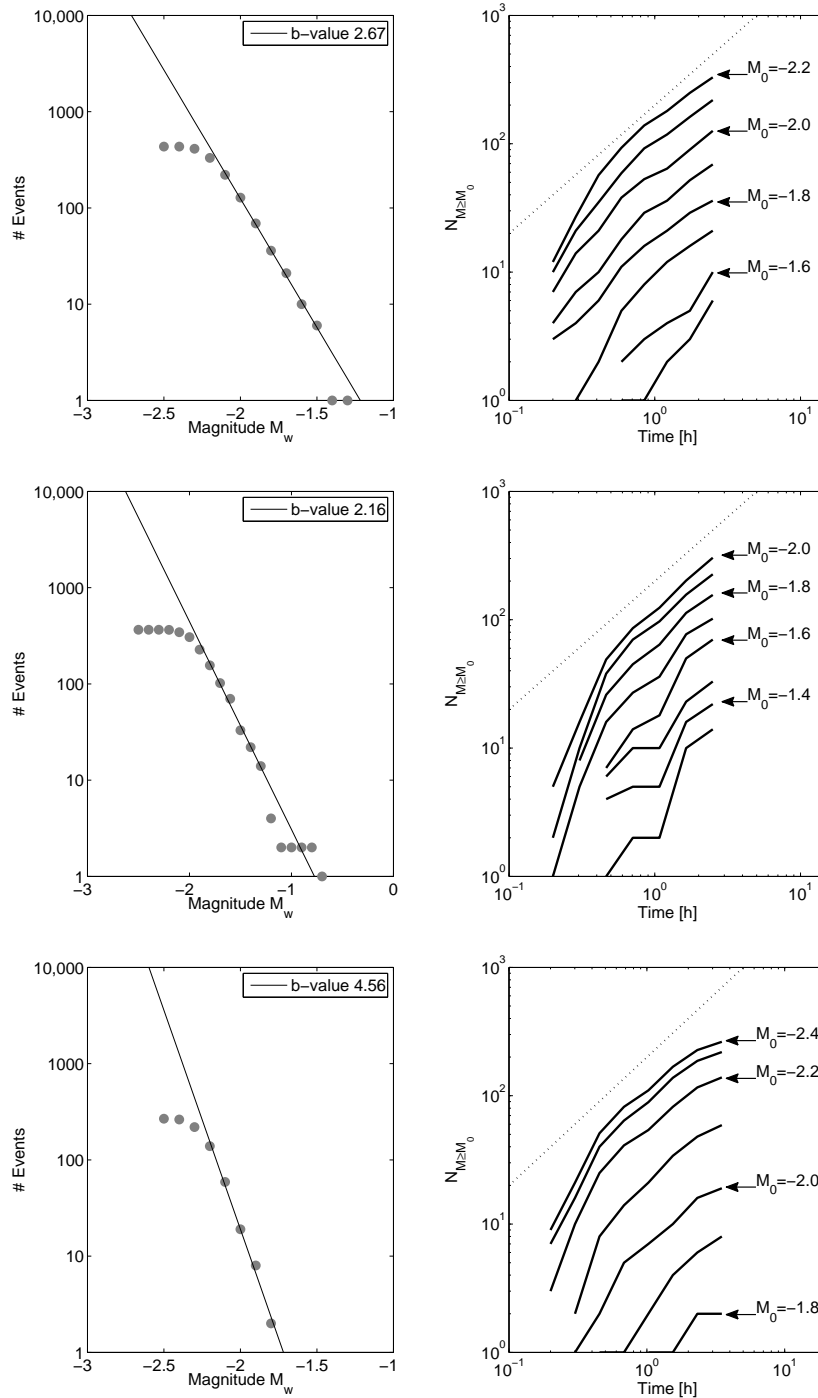


Figure 5.6: (Left) Frequency-magnitude distributions of microearthquakes induced during main treatments. Magnitudes of fracturing-induced seismicity also obeys Gutenberg-Richter scaling, but shows higher b-values compared to fluid-induced seismicity in geothermal reservoirs. (Right) Cumulative number of microearthquakes having a magnitude  $M$  larger than or equal to magnitudes  $M_0$  ( $N_{M \geq M_0}$ ) induced during main treatments as functions of time in double logarithmic scale. Dotted line is shown for convenience and has slope one illustrating the linear proportionality between the two quantities in double logarithmic scale. (Top) gel treatment Stage A, (middle) gel treatment Stage B, (bottom) water treatment Stage C.

possible. In contrast to hydrocarbon reservoirs, fluid injections which are aimed to develop geothermal systems have caused noticeable earthquakes at several locations (see e.g. Majer et al., 2007). These observations can again be explained by applying the presented formalism. It was found that induced seismicity from the geothermal reservoir in Basel is characterized by a lower  $b$ -value compared to the Cotton Valley hydrocarbon reservoir. In addition, here the  $b$ -value is decreasing with ongoing injection which is likely caused by reactivation of larger fracture planes due to increasingly stimulated reservoir volume.

# Chapter 6

## Summary and Perspectives

The thesis was aimed to further develop the seismicity based reservoir characterization approach (*SBRC*). In general, *SBRC* is applied to microearthquakes resulting from fluid injections into the subsurface which are carried out for a diversity of reasons. It hereby allows firstly to estimate the fluid-transport properties of hydraulically treated reservoir rock, secondly to examine the interactions of injected fluid and rock, and thirdly to characterize pre-existing fracture networks and fault zones within the reservoir. Thus, *SBRC* has substantially contributed to the present understanding of physical processes that are related to fluid-induced seismicity. To extend the applicability of *SBRC* the following topics have been addressed in this thesis.

### **Seismicity resulting from time-dependent injection source strength**

The deterministic *SBRC* methods so far assumed a constant source strength of a fluid injection. This condition, however, is not always given by injection experiments. In Chapter 3, *SBRC* has been extended to consider fluid injections where the strength of the source is linearly increasing with time. This special condition required in a first step the derivation of an analytical solution of the diffusion equation since an appropriate solution can not be found in literature. The derived analytical solution and the resulting expressions for seismicity rate and cumulative number of microearthquakes have been numerically verified using finite element modeling and synthetically generated seismicity. Afterwards, application of *SBRC* to the catalog of fluid-induced earthquakes recorded in Basel was presented providing consistent estimates of fluid transport properties of the stimulated geothermal reservoir. Furthermore, critical pressures of induced microearthquakes were determined using numerical modeling and their statistical distribution was reconstructed.

### **Seismicity resulting from hydraulic fracturing in tight-gas reservoirs**

If a fluid injection is aimed to create a hydraulic fracture, then the assumption of linear diffusion of pore pressure perturbations as the governing process of seismicity triggering is violated. The opening of newly fractured volume results in a sudden, strong increase in rock permeability. Consequently, the injected fluid can be faster transported to the regions of fracture tip. It also means that permeability becomes pressure-dependent and, thus, the diffusion process becomes non-linear. For such situations, following two problems pose. On the one hand, a theoretical construct to physically describe the triggering of fracturing-induced seismicity in terms of non-linear diffusion was not existing. On the other hand, an interpretational model for this type of seismicity in order to derive fluid transport properties was not available. Both problems have been addressed in the thesis. In Chapter 2.3, a general formulation of the diffusion equation was presented which enables a description of seismicity triggering resulting from simple hydraulic stimulation as well as from complex hydraulic fracturing. In Chapter 4, an approach was proposed to interpret seismicity related to single-planar hydraulic fractures in terms of *SBRC*. The model was applied to catalogs of fracturing-induced microearthquakes recorded during three fracturing stages in the Carthage Cotton Valley gas reservoir. The obtained results which include, for instance, fracture width and fluid-loss coefficient, are in agreement with results from independently performed maximum likelihood modeling.

### **Scaling relations of fluid-induced earthquake magnitudes**

Fluid injections into the subsurface can sometimes induce earthquakes that have a significant magnitude. In particular, seismic events with larger magnitudes are reported from injection operations in geothermal environment. Since geothermal energy recovery is considered as an energy source of long-term increasing demand, understanding of the statistics of magnitudes of fluid-induced seismicity is of essential importance. In Chapter 5, a theoretical model was introduced which describes the distribution of magnitudes of microearthquakes induced during injection. The model combines a Gutenberg-Richter statistics of magnitude probability with the cumulative number of induced microearthquakes. Magnitudes catalogs of microseismicity resulting from both hydraulic stimulation as well as hydraulic fracturing are in accordance with this model. In addition, the presented model allows to identify controlling parameters of the distribution of magnitudes and, thus, to develop strategies for a mitigation of possible seismic risk related to fluid injections. On the one hand, it is the injected fluid volume, precisely the injected fluid mass, which is a man-made, and hence a controllable parameter. On

the other hand, the statistical distribution of magnitudes is defined by seismotectonic quantities. These include Gutenberg-Richter  $a$ - and  $b$ -value and statistical properties of pre-existing fractures.

## Outlook

Although various characteristics of fluid-induced microseismicity can already be explained using the underlying model of the *SBRC* approach, there are several open questions. The following ideas which are partly studied at the moment address these questions and help to completely understand the physical processes and to optimize the reservoir characterization:

1. One aspect that has not been considered so far is the effect of poroelastic coupling on the triggering mechanism. Rudnicki (1986) presented analytical solutions of coupled deformation-diffusion processes for isotropic media and for the condition of a constant fluid mass source. These equations can be implemented in *SBRC* to evaluate this phenomenon. Further developments could then include extending the known solutions to consider anisotropic media and time-dependent sources.
2. More detailed studies on non-linear fluid-rock interactions can be carried out to better understand processes that are involved in hydraulic fracturing operations. A key point here is deriving an interpretational model for a reservoir characterization that can be applied to the special class of volumetric hydraulic fractures, such as they develop in the Barnett Shale tight-gas formation.
3. At present, there is an apparent disagreement in the estimates of critical pressures if compared to geomechanically based approaches. In Chapter 3, critical pore pressures of the induced seismicity in Basel were found to be between 1000 Pa and 1 MPa. For a subset of the same data, Mukuhira et al. (2009) determined critical pore pressures of the order of 50 – 80 MPa using information about the stress state and the orientation of fault planes. However, shortcomings of the geomechanical model are the assumptions of homogeneous distribution of normal stresses and a constant, static coefficient of friction. It is intuitive to suggest that material parameters, such as elastic moduli, are neither constant nor homogeneously distributed in the whole reservoir volume (see e.g. Cooke, 1997; Carpenter et al., 2009; Valley and Evans, 2010). It means that heterogeneities of stress distribution and a varying friction coefficient have to be considered in the calculation of critical pore pressures. On the other hand, the diffusion-based model of the *SBRC* approach also simplifies real situations because heterogeneities

of hydraulic parameters are not taken into account. Addressing those points aid to resolve the disagreement between the two approaches.

4. Further investigations of the scaling relations of fluid-induced earthquake magnitudes can be performed. In particular, post-injection microseismicity is in focus because at several injection locations the strongest earthquakes were induced after injection stop (Majer et al., 2007). Another concern applies to the observed non-stationarity of Gutenberg-Richter  $b$ -value in Basel. To evaluate and interpret this phenomenon more detailed and advanced studies are required.

# Bibliography

- Albright, J. N. and Pearson, C. F. (1982). Acoustic emissions as a tool for hydraulic fracture location: experience at the Fenton Hill Hot Dry Rock site. *Soc Petro Eng*, August:523–530.
- Arco Exploration and Production Technology (1997). Cotton Valley production stimulation hydrofracture Phase II. Technical report, UPR Consortium.
- Backers, T., Stanchits, S., and Dresen, G. (2005). Tensile fracture propagation and acoustic emission activity in sandstone: The effect of loading rate. *Int J Rock Mech Min Sci*, 42:1094–1101.
- Baisch, S., Bohnhoff, M., Ceranna, L., Tu, Y., and Harjes, H. P. (2002). Probing the crust to 9-km depth: Fluid-injection experiments and induced seismicity at the KTB superdeep drilling hole, Germany. *Bul Seism Soc of America*, 92(6):2369–2380.
- Baisch, S., Vörös, R., Weidler, R., and Wyborn, D. (2009). Investigation of fault mechanisms during geothermal reservoir stimulation experiments in the Cooper Basin, Australia. *Bul. Seism. Soc. of America*, 99:doi:10.1785/0120080055.
- Baisch, S., Weidler, R., Vörös, R., Wyborn, D., and DeGraaf, L. (2006). Induced seismicity during the stimulation of a geothermal HFR reservoir in the Cooper Basin (Australia). *Bul. Seism. Soc. of America*, 96:doi:10.1785/0120050255.
- Barenblatt, G. I. (1996). *Scaling, self-similarity, and intermediate asymptotics*. Cambridge University Press, New York, NY.
- Biot, M. A. (1962). Mechanics of deformation and acoustic propagation in porous media. *J Appl Phys*, 33:1482–1498.
- Block, L. V., Cheng, C. H., Fehler, M. C., and Phillips, W. S. (1994). Seismic imaging using microearthquakes induced by hydraulic fracturing. *Geophysics*, 59(1):102–112.

- Carpenter, B. M., Marone, C., and Saffer, D. M. (2009). Frictional behavior of materials in the 3D SAFOD volume. *Geophys Res Letters*, 36:doi:10.1029/2008GL036660.
- Carslaw, H. S. and Jaeger, J. C. (1973). *Conduction of Heat in Solids*. Oxford University Press, London.
- Carter, R. D. (1957). *Drilling and Production Practice*, chapter Optimum Fluid Characteristics for Fracture Extension, Appendix 1: Derivation of the General Equation for Estimating the Extent of the Fractured Area. American Petroleum Institute, New York.
- Cooke, M. L. (1997). Fracture localization along faults with spatially varying friction. *J Geophys Res*, 102(B10):22425–22434.
- Deichmann, N. and Giardini, D. (2009). Earthquakes induced by the stimulation of an Enhanced Geothermal System below Basel (Switzerland). *Seism Res Letters*, 80(5):doi:10.1785/gssrl.80.5.784.
- Delepine, N., Cuenot, N., Rothert, E., Parotidis, M., Rentsch, S., and Shapiro, S. A. (2004). Characterization of fluid transport properties of the Hot Dry Rock reservoir Soultz-2000 using induced microseismicity. *J. Geophys. Eng.*, 1:doi:10.1088/1742–2132/1/1/010.
- Detournay, E. and Cheng, A. H.-D. (1993). *Comprehensive Rock Engineering: Principles, Practice and Projects*, volume II: Analysis and Design Method, chapter 5: Fundamentals of Poroelasticity, pages 113–171. Pergamon Press.
- Dyer, B. C. (2001). Soultz GPK2 stimulation June/July 2000: Seismic monitoring report. Technical report, Semore Seismic, Cornwall, UK.
- Dyer, B. C., Schanz, U., Spillmann, T., Ladner, F., and Häring, M. O. (2008). Microseismic imaging of a geothermal reservoir stimulation. *TLE*, 27(7):856–869.
- Economides, M. J. and Nolte, K. G., editors (2003). *Reservoir Stimulation*. Wiley, Chichester.
- Eisbacher, G. H. (1996). *Einführung in die Tektonik*. Spektrum Akademischer Verlag, Stuttgart.
- Fehler, M., House, L., and Kaieda, H. (1987). Determining planes along which earthquakes occur: Method and application to earthquakes accompanying hydraulic fractures. *J Geophys Res*, 92:9407–9414.

- Fischer, T., Hainzl, S., Eisner, L., Shapiro, S. A., and Calvez, J. L. (2008). Microseismic signatures of hydraulic fracture growth in sediment formations: Observations and modeling. *J Geophys Res*, 113:doi:10.1029/2007JB005070.
- Fisher, M. K., Wright, C. A., Davidson, B. M., Goodwin, A. K., Fielder, E. O., Buckler, W. S., and Steinsberger, N. P. (2005). Integrating fracture-mapping technologies to improve stimulations in the Barnett Shale. *SPE Prod Fac*, 20(2):doi:10.2118/77441-PA.
- Gallagher, R. H. (1975). *Finite Element Analysis: Fundamentals*. Prentice-Hall, Englewood Cliffs, NJ.
- Geertsma, J. and de Klerk, F. (1969). A rapid method of predicting width and extent of hydraulic induced fractures. *J Petrol Tech*, 21:1571–1581.
- Gutenberg, B. and Richter, C. F. (1954). *Seismicity of Earth and associated Phenomenon*. Princeton University Press, Princeton.
- Häring, M. O., Schanz, U., Ladner, F., and Dyer, B. C. (2008). Characterisation of the Basel 1 enhanced geothermal system. *Geothermics*, page doi:10.1016/j.geothermics.2008.06.002.
- Harrington, L. and Hannah, R. R. (1975). Fracturing design using perfect support fluids for selected fracture proppant concentrations in vertical fractures. In *SPE Annual Meeting*, Dallas.
- Hori, Y., Kitano, K., Kaieda, H., and Kiho, K. (1999). Present status of the Ogachi HDR project, Japan, and future plans. *Geothermics*, 28(4-5):doi:10.1016/S0375-6505(99)00034-6.
- House, L. (1987). Locating microearthquakes induced by hydraulic fracturing in crystalline rocks. *Geophys Res Letters*, 14:919–921.
- Hubbert, M. and Willis, D. (1957). Mechanics of hydraulic fracturing. *J Petrol Tech*, 9(6):153–168.
- Kaiser, J. (1950). *A study of acoustic phenomena in tensile test*. PhD thesis, Technical University Munich.
- Kay, S. (1993). *Fundamentals of Statistical Signal Processing*, volume I: Estimation Theory. Prentice Hall.
- Keck, R. G. and Withers, R. J. (1994). A field demonstration of hydraulic fracturing for solid waste injection with real-time passive seismic monitoring. In *Proc 1994 Soc Petro Eng Annu Tech Conf*, page Paper 28495, New Orleans.

- Khristianovich, S. A. and Zheltov, Y. P. (1955). Formation of vertical fractures by means of highly viscous liquid. In *Fourth World Petrol Congress*, volume 2, pages 579–586, Rome.
- Kurita, K. and Fuji, N. (1979). Stress memory of crystalline rocks in acoustic emission. *Geophys Res Letters*, 6:9–12.
- Langenbruch, C. and Shapiro, S. A. (2009). Induced seismicity after termination of rock stimulations: Possibilities for reservoir characterization. In *79th SEG Conference Expanded Abstracts*, pages Paper-RC5.1, Houston.
- Langenbruch, C. and Shapiro, S. A. (2010). Decay rate of fluid-induced seismicity after termination of reservoir stimulations. *Geophysics*, 75.
- Lockner, D. A. (1998). A generalized law for brittle deformation of Westerly granite. *J Geophys Res*, 103(B3):5107–5123.
- Majer, E. L., Baria, R., Stark, M., Oates, S., Bommer, J., Smith, B., and Asanuma, H. (2007). Induced seismicity associated with Enhanced Geothermal Systems. *Geothermics*, 36:doi:10.1016/j.geothermicss.2007.03.003.
- Maxwell, S., Waltman, C., Warpinski, N. R., Mayerhofer, M., and Boroumand, N. (2009). Integrating fracture-mapping technologies to improve stimulations in the Barnett Shale. *SPE Res Eval & Eng*, 12(1):doi:10.2118/102801-PA.
- Mukuhira, Y., Asanuma, H., Niitsuma, H., Häring, M., and Deichmann, N. (2009). Investigation of relationship of pore pressure to large microseismic events with large collected at Basel, Switzerland in 2006 33, 331-335. *Trans GRC*, 33:331–335.
- Nordgren, R. P. (1972). Propagation of a vertical hydraulic fracture. *SPE Journal*, 12(8):306–314.
- Parotidis, M. and Shapiro, S. A. (2004). A statistical model for the seismicity rate of fluid-injection-induced earthquakes. *Geophys Res Letters*, 31:doi:10.1029/2003GL020421.
- Parotidis, M., Shapiro, S. A., and Rotherth, E. (2004). Back front of seismicity induced after termination of borehole fluid injection. *Geophys Res Letters*, 31:doi:10.1029/2003GL018987.
- Pearson, C. (1981). The relationship between microseismicity and high pore pressures during hydraulic stimulation experiments in low permeability granitic rocks. *J Geophys Res*, 86:7855–7864.

- Perkins, T. K. and Kern, L. R. (1961). Width of hydraulic fractures. *J Petro Tech*, 13(9):937–949.
- Phillips, W. S., House, L. S., and Fehler, M. C. (1997). Detailed joint structure in a geothermal reservoir from studies of induced microearthquake clusters. *J Geophys Res*, 102:11745–11763.
- Pinnacle Technologies (1999). Cotton Valley fracture imaging project Phase III - final report. Technical report, JIP Consortium.
- Rindschwentner, J. (2001). Estimating the global permeability tensor using hydraulically induced seismicity. Master's thesis, Freie Universität Berlin.
- Rothert, E. (2004). *Fluid induced microseismicity: Data modeling and inversion for hydraulic properties of rocks*. PhD thesis, Freie Universität Berlin.
- Rothert, E. and Shapiro, S. A. (2007). Statistics of fracture strength and fluid-induced microseismicity. *J Geophys Res*, 112:doi:10.1029/2005JB003959.
- Rowe, C. A., Aster, R. C., Phillips, W. S., Jones, R. H., Borchers, B., and Fehler, M. C. (2002). Using automated, high-precision repicking to improve delineation of microseismic structures at the Soultz geothermal reservoir. *Pure Appl Geophysics*, 159.
- Rudnicki, J. W. (1986). Fluid mass sources and point forces in linear elastic diffusive solids. *Mechanics of Materials*, 5:383–393.
- Rutledge, J. T. and Phillips, W. S. (2003). Hydraulic stimulation of natural fractures as revealed by induced microearthquakes, Carthage Cotton Valley gas field, east Texas. *Geophysics*, 68:441–452.
- Rutledge, J. T., Phillips, W. S., and Mayerhofer, M. J. (2004). Faulting induced by forced fluid injection and fluid flow forced by faulting: An interpretation of hydraulic-fracture microseismicity, Carthage Cotton Valley gas field, Texas. *Bul. Seism. Soc. of America*, 94:1817–1830.
- Scholz, C. H. (2002). *Mechanics of Earthquake and Faulting*. Cambridge University Press, New York.
- Shapiro, S. A., Audigane, P., and Royer, J.-J. (1999). Large-scale in situ permeability tensor of rocks from induced microseismicity. *Geophys J Int*, 137:207–213.

- Shapiro, S. A. and Dinske, C. (2009a). Fluid-induced seismicity: Pressure diffusion and hydraulic fracturing. *Geophysical Prospecting*, 57(2):doi:10.1111/j.1365-2478.2008.00770.x.
- Shapiro, S. A. and Dinske, C. (2009b). Scaling of seismicity induced by nonlinear fluid-rock interaction. *J Geophys Res*, 114(B09307):doi:10.1029/2008JB006145.
- Shapiro, S. A., Dinske, C., and Kummerow, J. (2007). Probability of a given-magnitude earthquake induced by a fluid injection. *Geophys Res Letters*, 34:doi:10.1029/2007GL031615.
- Shapiro, S. A., Dinske, C., and Rothert, E. (2006a). Hydraulic-fracturing controlled dynamics of microseismic clouds. *Geophys Res Letters*, 33:doi:10.1029/2006GL026365.
- Shapiro, S. A., Huenges, E., and Borm, G. (1997). Estimating the permeability from fluid-injection induced seismic emission at the KTB site. *Geophys J Int*, 131:F15–F18. see also Corrigendum, *Geophys J Int*, 134, 913.
- Shapiro, S. A., Kummerow, J., Dinske, C., Asch, G., Rothert, E., Erzinger, J., Kümpel, H.-J., and Kind, R. (2006b). Fluid induced seismicity guided by a continental fault: Injection experiment of 2004/2005 at the German Deep Drilling site (KTB). *Geophys Res Letters*, 33:doi:10.1029/2005GL024659.
- Shapiro, S. A., Patzig, R., Rothert, E., and Rindschwentner, J. (2003). Triggering of seismicity by pore-pressure perturbations: permeability-related signatures of the phenomenon. *Pure Appl Geophys*, 160:1051–1061.
- Shapiro, S. A., Rentsch, S., and Rothert, E. (2005). Characterization of hydraulic properties of rocks using probability of fluid-induced microearthquakes. *Geophysics*, 70:F27–F33.
- Shapiro, S. A., Rothert, E., Rath, V., and Rindschwentner, J. (2002). Characterization of fluid transport properties of reservoirs using induced microseismicity. *Geophysics*, 67:212–220.
- Sileny, J., Eisner, L., Hill, D. P., and Cornet, F. H. (2008). Non-double-couple mechanisms of microearthquakes induced by hydraulic fracturing. In *70th EAGE Conference and Exhibition*, page PO21, Rome.
- Tanimoto, K., Nakamura, J., and Fudo, R. (1978). Application of acoustic emission in in-situ test. In *Proc, 10th Int Conf on soil mechanics and foundation engineering*, volume 2, pages 573–576, Rotterdam. Balkema.

- Tensi, H. M. (2004). The Kaiser effect and its scientific background. In *Proc of 26th Europ Conf on acoustic emission testing*, pages 31–42, Berlin.
- Terzaghi, K. (1923). Die Berechnung der Durchlässigkeitsziffer des Tones aus dem Verlauf der hydrodynamischen Spannungserscheinungen. *Sitzungsberichte Akad. Wiss. Wien*, 132:125–138.
- Urbancic, T. and Rutledge, J. T. (2000). Using microseismicity to map Cotton Valley hydraulic fractures. In *SEG Expanded Abstracts 19*, page doi:10.1190/1.1815676.
- Valley, B. and Evans, K. F. (2010). Stress heterogeneity in the granite of the Soultz EGS reservoir inferred from analysis of wellbore failure. In *World Geothermal Congress*, Bali, Indonesia.
- Walker, R. N. (1997). Cotton Valley hydraulic fracture imaging project. In *Proc 1997 Soc Petro Eng Annu Tech Conf*, page Paper 38577, San Antonio.
- Warpinski, N. R., Engler, B. P., Young, C. J., Peterson, R., Branagan, P. T., and Fix, J. E. (1995). Microseismic mapping of hydraulic fractures using multi-level wireline receivers. In *Proc 1995 Soc Petro Eng Annu Tech Conf*, page Paper 30507, Dallas.
- Wescott, W. A. (1984). Diagenesis of a tight gas formation: Jurassic Cotton Valley sandstone, East Texas Basin. *AAPG Bulletin*, 68:doi:10.1306/AD4618C2-16F7-11D7-8645000102C1865D.
- Zang, A., Wagner, F. C., Stanchits, S., Janssen, C., and G.Dresen (2000). Fracture process zone in granite. *J Geophys Res*, 105(B10):23651–23661.
- Zoback, M. D. and Harjes, H. P. (1997). Injection-induced earthquakes and crustal stress at 9 km depth at the KTB deep drilling site, Germany. *J Geophys Res*, 102(B8):18477–18491.



# **Appendix A**

## **Supplement to Chapter 4**

Summarized in this chapter of the appendix is the interpretation of seismicity induced by hydraulic fracturing Stage B in Carthage Cotton Valley tight-gas reservoir. The treatment was performed using a cross-linked gel injected through perforated intervals of borehole CGU 21-10. The induced seismicity was monitored by geophones placed in wells CGU 21-09 and CGU 22-09. In the figure section included are:

- map and depth view of source locations of induced seismicity
- engineering data
- $r - t$  diagram of induced seismicity
- plots of the results

The estimated parameters regarding fracture and reservoir properties after application of the presented interpretational approach are summarized in Table 4.2.

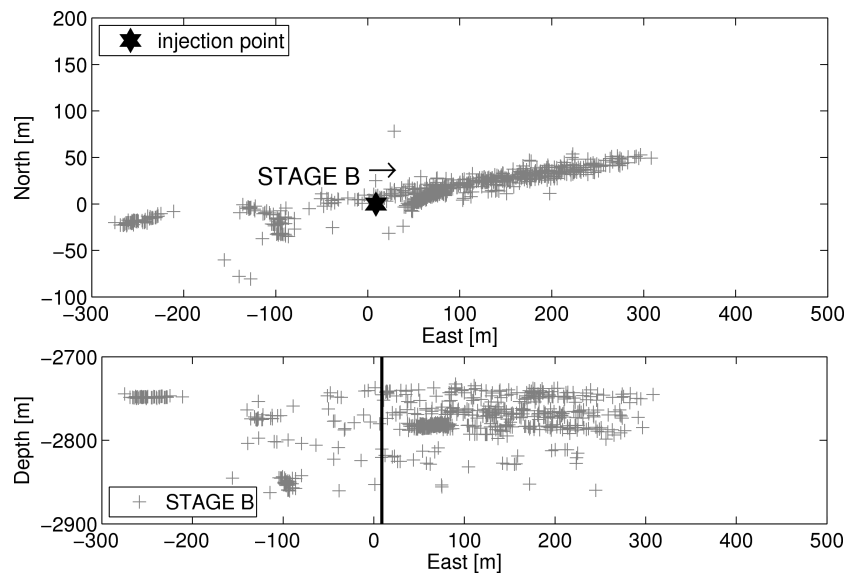


Figure A.1: Map view and depth view of source locations of microearthquakes induced in Stage B gel treatment.

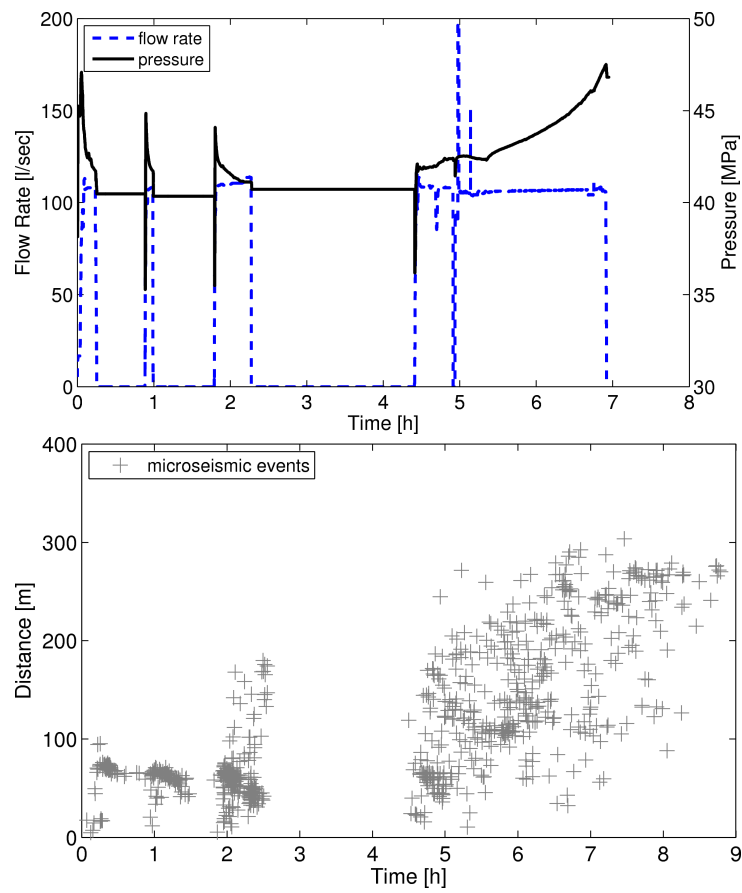


Figure A.2: (Top) Hydraulic fracturing treatment data and (bottom)  $r-t$  diagram of induced microearthquakes of Stage B gel treatment.

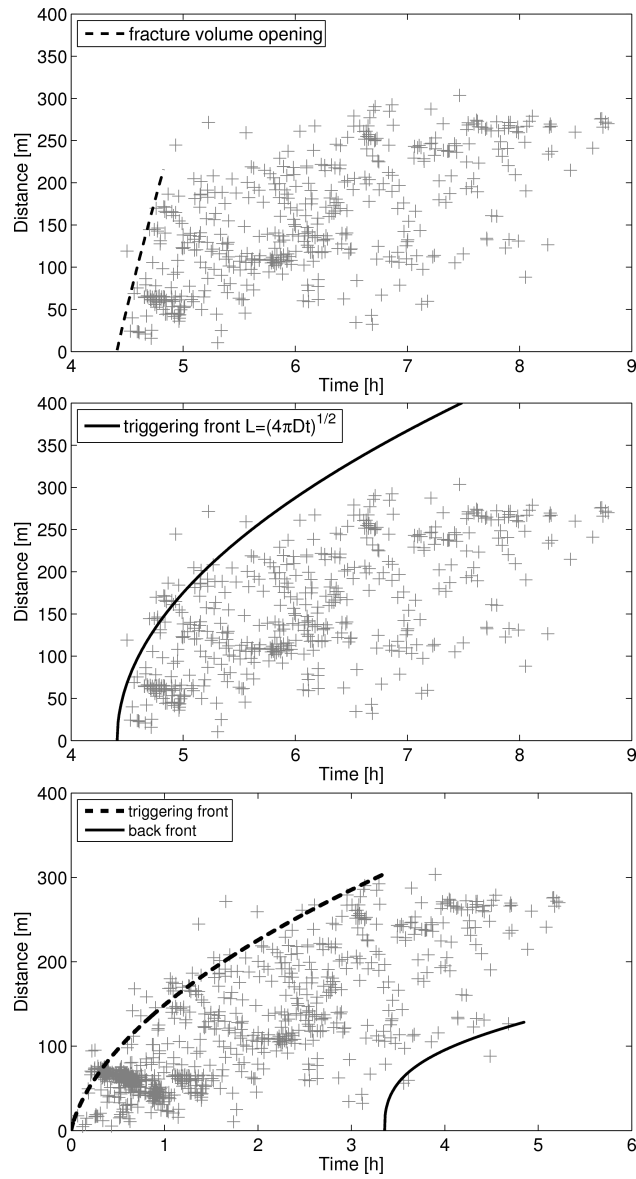


Figure A.3: (Top)  $r - t$  diagram of microearthquakes induced in main treatment period of Stage B gel treatment, dashed line indicates fracture volume opening, (middle)  $r - t$  diagram as before but with triggering front curve according to Equation 2.4 to describe the diffusion-like propagation of seismicity, (bottom) modified  $r - t$  diagram with removed shut-in phases. Triggering and back front curves according to Equations (4.2) and (4.5) will limit the microseismic event cloud.

Supplement to Chapter 4.6.2, Breakdown of Kaiser effect:  
analysis of Stage B and Stage C seismicity

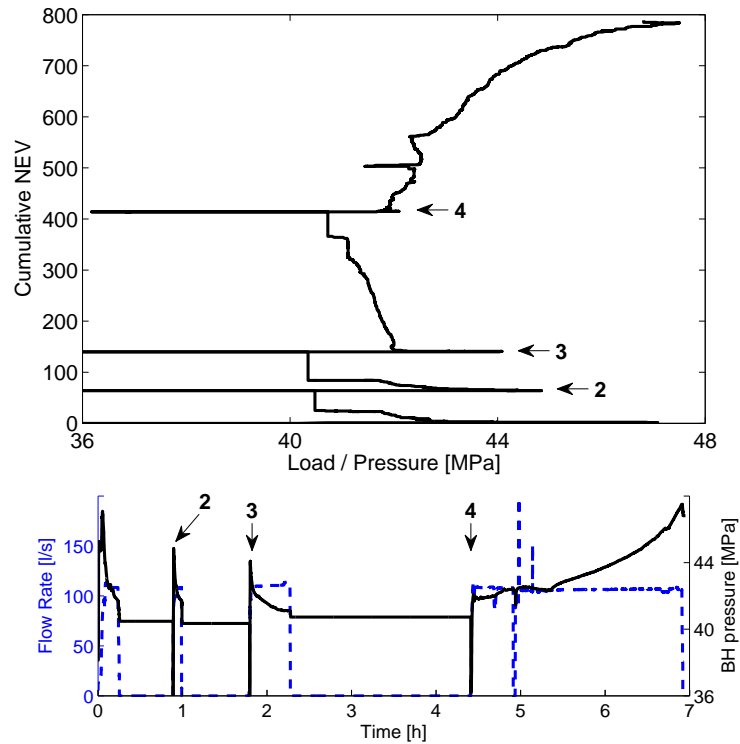


Figure A.4: (Top) Cumulative number of microearthquakes (NEV) induced in Stage B gel treatment as function of bottom hole pressure, (Bottom) Hydraulic treatment data (dashed line: flow rate, solid line: bottom hole pressure) of Stage B gel treatment. Numbers 2, 3 and 4 show the same time moments in both figures. They mark starting points of an injection cycle.

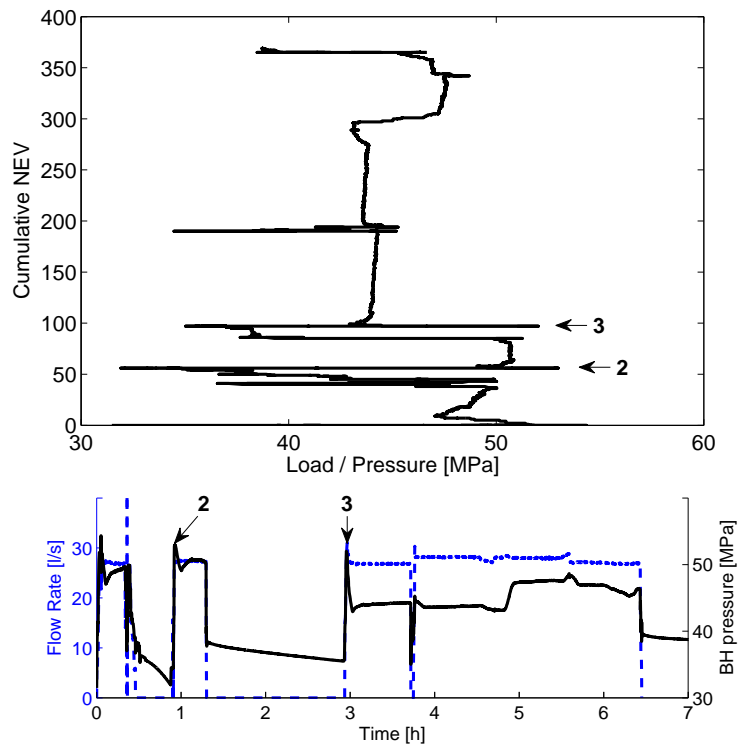


Figure A.5: (Top) Cumulative number of microearthquakes (NEV) induced in Stage C water treatment as function of bottom hole pressure, (Bottom) Hydraulic treatment data (dashed line: flow rate, solid line: bottom hole pressure) of Stage C water treatment. Numbers 2 and 3 show the same time moments in both figures. They mark starting points of an injection cycle.

## Danksagung

An erster Stelle möchte ich Prof. Dr. Serge Shapiro herzlich danken für die wissenschaftliche Betreuung der Doktorarbeit. Die zahlreichen Ideen und Anregungen sowie die aufschlussreichen Gespräche haben wesentlich zum Gelingen dieser Arbeit beigetragen.

Prof. Dr. Rainer Kind danke ich recht herzlich für die Übernahme des Koreferats. Prof. Dr. Georg Kaufmann, Prof. Dr. Mark Handy und Dr. Jörn Kummerow gilt mein Dank für die Teilnahme in der Disputationskommission.

Ein herzliches Danke geht an Cornelius Langenbruch und Nicolas Hummel für das sorgfältige Korrekturlesen des Manuskripts.

Ich danke Markus Häring (Geothermal Explorers Ltd.) für die Bereitstellung der Basel Daten sowie Jim Rutledge (Los Alamos National Laboratory), welcher die Cotton Valley Daten freundlicherweise zur Verfügung gestellt hat. Mein Dank gilt auch Dr. Sebastian Hainzl (GFZ Potsdam) für seine Hilfe in der *Likelihood*-Modellierung. Desweiteren danke ich den Sponsoren des PHASE (Physics and Application of Seismic Emission) Konsortium.

Ein besonderes Dankeschön all den Menschen die mich in den zurückliegenden Jahren - beruflich wie privat - begleitet und diese zu einer angenehmen und wunderbaren Zeit gemacht haben.

Ich danke von ganzem Herzen meinen Eltern Marlies und Harald sowie meiner Schwester Janine für die liebevolle Unterstützung und Aufmunterung während meines Studiums und meiner Promotion.

## **LEBENS LAUF**

Der Lebenslauf ist in der Online-Version aus Gründen des Datenschutzes nicht enthalten.